POLITECNICO
MILANO 1863

SCUOLA DI INGEGNERIA INDUSTRIALE
E DELL'INFORMAZIONE

Ultrafast Yb:CALGO amplified laser for broadband mid-infrared generation

Tesi di Laurea Magistrale in
Physics Engineering - Ingegneria Fisica

Author: **Loris Freddi**

Student ID: 990110
Advisor: Prof. Nicola Coluccelli
Co-advisors: Dr. Gianluca Galzerano, Dr. Francesco Canella
Academic Year: 2022-23

Contents

List of Figures

List of Tables

Acknowledgements

I would like to thank Dr. Gianluca Galzerano for his precious advices and his effort in making this work possible. A special thanks to Dr. Francesco Canella who patiently helped me and supported me from the beginning of the experiment despite the difficulties encountered.
Lastly, I would like to thank my family and Chiara who supported me during these years of engineering studies and allowed me to arrive where I am today.

Abstract

In this thesis work we demonstrate a simple approach to generate amplified few-optical-cycles pulses starting from a mode-locked Yb:CALGO femtosecond laser emitting at 1 µm for broadband mid-infrared generation. The initial pulses characterized by a duration of 70 fs and an average power of 45 mW are amplified by an Yb-based fiber amplifier and optically compressed by a pair of diffraction gratings. The output pulses characterized by a duration of 80 fs and an average power of 5 W are then coupled within a photonic crystal fiber producing 100 nm spectral broadening. If these are optically compressed and focused in an orientation-patterned gallium phosphide (OP-GaP) crystal, we can generate by means of intrapulse difference frequency generation a radiation spanning the mid-infrared range.

Abstract in lingua italiana

In questo lavoro di tesi dimostriamo un semplice approccio per la generazione di impulsi amplificati a pochi cicli ottici utili per produrre una radiazione a larga banda nel medio infrarosso partendo da un mode-locked Yb:CALGO laser che emette ad 1 µm. Gli impulsi iniziali, caratterizzati da una durata di 70 fs e una potenza media di 45 mW, sono amplificati da un amplificatore in fibra drogata Itterbio e compressi otticamente per mezzo di una coppia di reticoli di diffrazione. Gli impulsi in uscita, caratterizzati da una durata di 80 fs e una potenza media di 5 W, sono poi accoppiati in una fibra a cristallo fotonico producendo un allargamento spettrale pari a 100 nm. Se questi sono poi compressi otticamente e focalizzati in un cristallo di fosfuro di gallio a disegno orientato, possiamo produrre per mezzo di una differenza di frequenza tra le componenti spettrali degli impulsi una radiazione che si estende nella regione spettrale del medio infrarosso.

Introduction

The term "broadband mid-infrared light" refers to a region of the electromagnetic spectrum spanning 2-20 µm (500-5000 cm^{-1}) crucial for a large number of applications. The practical interest of this interval comes from the presence of the fundamental vibrational modes of most of the molecules that makes mid-infrared a versatile tool for spectroscopy in the molecular fingerprint (500-1800 cm^{-1}). The non-invasive and label-free optical measurements provided are useful in diagnosis of diseases via biomarkers in human breath [1], contamination control in manufacturing processes [2], detection of poisonous gasses or explosives [3], environmental monitoring [4], and more [5]. Apart from spectroscopic applications, broadband mid-infrared radiation represents an ideal prerequisite for hyperspectral imaging [6], and for time-domain coherent control of vibrational dynamic [7][8].
In last two decades, the large number of perspectives in terms of applications produces an intense research activity on mid-infrared sources. Despite the great effort, covering this spectral region with conventional laser technologies remains a challenge. Over the years, many light sources demonstrated to be able to emit in this spectral range: quantum cascade lasers [9], optical parametric oscillators [10], supercontinuum sources [11], optical parametric amplifiers [12], and sources based on difference frequency generation (DFG) [13]. However, they faced a lot of technical problems in terms of brightness, spectrum flatness, repetition rate, robustness, and spectral bandwidth [14]. Among them the most attractive are the sources based on DFG for various reasons. First of all, the use of a frequency-conversion nonlinear process allows to adopt as principal source a mode-locked laser emitting in the near-infrared which is a well-established technology employed in many fields. Then, difference-frequency generation is simple and robust and it can produce high average power radiation covering the full fingerprint region. Mode-locked oscillators combined with DFG allow very precise applications such as dual-comb spectroscopy [15], time-stretch spectroscopy [16], and field-resolved spectroscopy [17].
This thesis work deals with the design and the characterization of a system able to produce amplified few-optical-cycles pulses starting from a mode-locked Yb:CALGO femtosecond laser emitting at 1 µm for broadband mid-infrared generation. The initial pulses are characterized by a duration of 70 fs and an average power of 45 mW. In terms of spectral properties, their spectrum is centred around 1050 nm and it shows a full width at half maximum of 15 nm. By combining an Ytterbium-base fiber amplifier and an optical compressor made of a pair of diffraction gratings in double-pass configuration, we produce pulses with a duration of 80 fs and average power of 5 W. For the generation of broadband mid-infrared radiation, we would exploit the intrapulse difference-frequency generation (IDFG) which is a particular case of DFG where the

nonlinear interaction that produces new frequencies happens among the components within the bandwidth of the starting pulse. As consequence, to produce a broadband radiation the spectrum must be broadened, and this is done by exploiting the supercontinuum generation in a photonic crystal fiber. If the output pulses are then compressed by means of a hollow core fiber or a pair of prisms, in relation to the results obtained we expect to produce pulses characterized by a duration of 12 fs and average power higher than 2.5 W. By focusing them into an orientation-patterned gallium phosphide (OP-GaP) we expect to generate a radiation of few milliwatt spanning the mid-infrared range. This is not the only possible application since amplified few-optical-cycles pulses can be used also for the generation of the terahertz radiation and of the 4^{th}-harmonic by simply changing the crystal. This aspect underlines the versatility of our system. All the passages up to the supercontinuum generation are characterized in terms of spectrum, average power, pulse duration, and relative intensity noise.
The thesis is structure as following:

1. The first chapter deals with general concepts useful for understanding all the processes that characterize the system. It opens with a brief description of the mode-locking techniques followed by an introduction on ytterbium-based solid-state and fiber laser to understand the general principles behind the master oscillator. The chapter proceed describing the types of specialty optical fibers adopted in our setup and the dispersion added by themselves while the pulses propagate. It closes with an analysis of the self-phase modulation which is third order nonlinear process exploited in the supercontinuum generation.

2. The second chapter focused on the setup adopted. It starts with brief description of the mode-locked Yb:CALGO femtosecond laser followed by a characterization of it in terms of spectrum, pulse duration, average power, and relative intensity noise. Then, the scheme and the mathematical models behind the fiber amplifier are presented. It closes with a section describing how the optical compressor used in the experiment work.

3. The third chapter presents the characterization of the pulses after the fiber amplifier and the optical compressor in terms of spectrum, pulse duration, average power, and relative intensity noise. This section is followed by a mathematical description of the supercontinuum generation. It closes with the results of the spectral broadening and the characterization of the pulse at the output of the photonic crystal fiber.

4. The fourth chapter starts focusing on the three-wave interaction processes which constitute the base of the applications involving few-optical-cycles pulses. The following section compares two different crystals used for the mid-infrared generation and it contains an estimation of the results that we would have obtained with our pulses. The chapter closes with a brief description of other two possible applications which are terahertz and 4^{th}-harmonic generation.

5. The fifth chapter closes the thesis by summarizing the result obtained and by suggesting possible improvement in future experiments.

1 | Introductory concepts

This chapter presents theoretical contents related to the activities done in this thesis work. It opens with a briefly introduction on mode-locking principles and techniques followed by a comparison between solid-state Ytterbium-based oscillators and equivalent fiber lasers. Then, all the types of fibers used in this thesis work are presented. It closes with the analysis of the dispersive and nonlinear effects affecting the propagation of ultrashort pulses in a media.

1.1 Lasers emitting at 1 µm

The importance of ultrafast lasers emitting in near infrared region is due to their application in many scientific and industrial fields, such as sensors, telecommunication, medicine, and high-resolved spectroscopy [18]. One category of lasers emitting in the region around 1 µm is constituted by optical oscillators based on Ytterbium-doped crystals and glasses. However, this is not the unique possibility since there exist also Yb-doped fiber lasers emitting in that spectral region. The following subchapters go into the details of both these types of oscillators.

1.1.1 Mode-locking theoretical principles and techniques

The term ultrafast lasers indicates oscillators able to emit optical pulses with a temporal duration in the domain of the femtoseconds (1 fs = 10^{-15} s). The generation of such short pulses in time-domain can be achieved only by means of mode-locking (ML) techniques. ML is defined as a multimodal regime of operation where laser modes have a precise relation among their phases. This operative condition is achieved by introducing a certain modulation that can be externally driven (Active ML) or generated by nonlinear elements introduced inside the cavity (passive ML) [19]. The details of the techniques used will be treated later in the text.
Consider a very simple linear cavity made by two plane mirrors separated by a distance L. The oscillating electric field E(t,z) must satisfy the following boundary conditions:

$$\begin{cases} \mathrm{E}(\mathrm{t}, \mathrm{z} = 0) = 0 \\ \mathrm{E}(\mathrm{t}, \mathrm{z} = \mathrm{L}) = 0 \end{cases} \tag{1.1}$$

By imposing these, we get a discrete set of frequencies f_n allowed to oscillate called longitudinal modes. The latter are regularly separated by a quantity δf called free

spectral range:

$$\delta f = f_n - f_{n-1} = \frac{1}{\mathrm{T_R}} \tag{1.2}$$

Here $\mathrm{T_R}$ is the round-trip time defined as the time needed to a pulse to make a complete trip within the cavity:

$$\mathrm{T_R} = \frac{2\mathrm{L}}{\mathrm{v_g}} \tag{1.3}$$

where v_g is the group velocity. This holds in case of optical pulses since, in presence of waves, v_g is substituted by the phase velocity $v_{ph} = c/n$. The frequency of the m-th mode can be written as:

$$f_m = m f_r + \frac{\Delta\phi_{CEP}}{2\pi} f_r \tag{1.4}$$

In Eq. (1.4), f_r is the pulse repetition defined as the inverse of $\mathrm{T_R}$ while $\Delta\phi_{CEP}$ represent the pulse-to-pulse carrier-envelope phase (CEP) slipping. Both f_r and $\Delta\phi_{CEP}$ tend to change over the time due to external noises and so they required to be stabilized.
Consider N oscillating modes all with the same amplitude $\mathrm{E_0}$. If we focus for simplicity on a point near one of the two plane mirrors, the electric field can be written as the superposition of these N modes:

$$\mathrm{E(t)} = \sum_{\mathrm{n=-N/2}}^{\mathrm{N/2}} \mathrm{E_0 \sin[2\pi(f_0 + n\,\delta f)\,t + \varphi_n(t)]} \tag{1.5}$$

where φ_n are the amplitude and the phase of the n-th mode while f_0 is central frequency of the laser spectrum. Figure 1.1 shows the time behaviour of the total electric field squared in case of 31 oscillating modes with same amplitude $\mathrm{E_0}$ and with random phases provided by Svelto in Ref. [20].

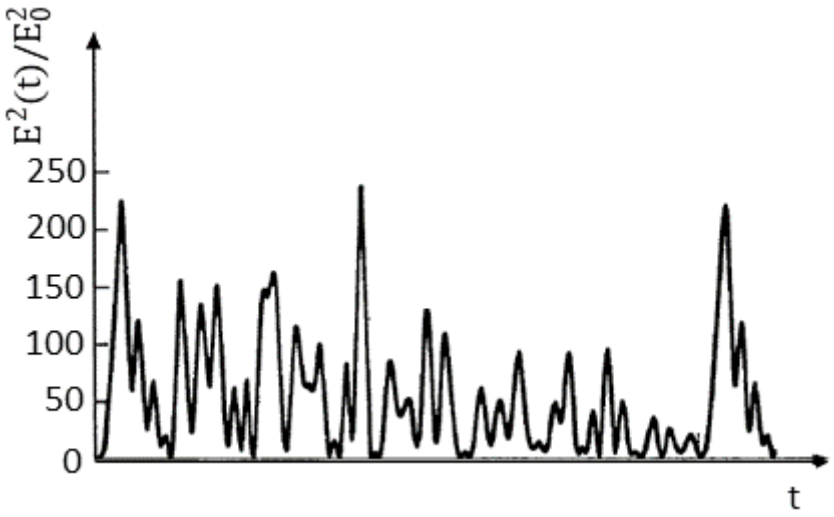

Figure 1.1: Time behaviour of the total electric field squared in case of 31 oscillating modes with same amplitude E_0 and with random random phases provided by Svelto in Ref. [20].

Now, we can impose a phase relation as required by mode-locking regime. The simplest case is represented by a linear relation $\varphi_n = \mathrm{n}\alpha$ such that:

$$\Delta\varphi = \varphi_n - \varphi_{n-1} = \alpha \tag{1.6}$$

The overall field in ML regime is given by:

$$\mathrm{E(t)} = \sum_{\mathrm{n=-N/2}}^{\mathrm{N/2}} \mathrm{E_0} \sin\left[2\pi\left(f_0 + \frac{\mathrm{N}-1}{2}\delta f\right)\mathrm{t}\right] \frac{\sin(\mathrm{N}\,\delta f \varphi\,\mathrm{t})}{\sin(\delta f \varphi\,\mathrm{t})} \tag{1.7}$$

If we look at the expression of the power got by averaging fast components:

$$\mathrm{P(t)} = \frac{1}{2}|\mathrm{E_0}|^2 \left[\frac{\sin(\mathrm{N}\,\delta f \varphi\,\mathrm{t})}{\sin(\delta f \varphi\,\mathrm{t})}\right]^2 = \mathrm{P_0}\left[\frac{\sin(\mathrm{N}\,\delta f \varphi\,\mathrm{t})}{\sin(\delta f \varphi\,\mathrm{t})}\right]^2 \tag{1.8}$$

it is possible to retrieve the following three key features of ML regime:

- P(t) has the shape of a pulse train with repetition rate $\delta f = f_r = \frac{1}{\mathrm{T_R}}$
- The peak power $\mathrm{P_{peak}}$ defined as the maximum of the average power is proportional to N^2, $\mathrm{P_{peak}} = \mathrm{N}^2\,\mathrm{P_0}$
- The pulse duration is inversely proportional to the number of modes locked and so the FWHM Δt_{FWHM} is approximately equal to inverse of the laser spectrum $\Delta f = \mathrm{N}\delta f$

Now, we start analysing the most interesting techniques used to achieve mode-locking regime. As already mentioned, there are two approaches, the active ML and the passive ML. The former techniques are well-established and exploit an externally driven modulator that needs to be precisely synchronize with the oscillator cavity. Below is a list of some of the most widespread and relevant active methods.

- *Synchronous pumping* [21]. In this technique, mode-locking is achieved by using a pulsed laser as pump. In this way laser gain increases only when pulses pass through the active medium.
- *Synchronous loss modulation* [19]. In this technique an amplitude modulation of a continuous-wave laser is used to achieve the mode-locking regime. This can be done by means of either an acusto-optic modulator or an electro-optic modulator.
- *Synchronous phase modulation* [22]. The key principle is similar to the previous technique with the difference that here the quantity modulated is the phase. This can be achieved with an electro-optic modulator.
- *Harmonic mode-locking* [23]. In this technique the modulator used to achieve mode-locking is driven by one of the harmonics of the laser cavity frequency.

Since the synchronization between oscillator cavity and externally driven modulator is not an easy task, sometimes it is preferable to use passive techniques. Apart from overcoming this problem, the latter ensures also a better performance in terms of pulse duration achievable. In passive ML techniques, pulses are generated by means of nonlinear elements. The most widespread and relevant methods are:

- *Mode-locking based on saturable absorbers* [24]. A saturable absorber is an optical element with a transmission that increases with the intensity of light. When a laser is switched on, it is in continuous-wave regime in which there is no correlation among the phases of the modes. As consequence, the output intensity will show some random fluctuations that present time-to-time intense spikes caused by the random interference of modes. When light pass through the saturable absorber the small fluctuations are killed due to a low transmission while the intense spikes, representing the pulses, are transmitted. We distinguish among fast or slow absorber depending on their recovery time.
- *Kerr-lens mode-locking (or self-focusing mode-locking)* [24] [25] [26]. This technique exploits a third order nonlinear effect called self-focusing where, depending on the intensity, light is focused in different manners. Higher is the intensity, stronger is the focusing effect. So, by introducing in the cavity an iris it is possible to select high-intensity pulses.
- *Nonlinear polarization rotation* [24] [27]. This technique is similar to kerr-lens mode-locking. Indeed, the intensity-dependent polarization rotation can be exploited to select high-intensity pulses since they rotate more than low-intensity ones. The selection can be done by introducing in the cavity either birefringent plates or polarizing beamsplitters.

1.1.2 Solid-State Yb-based lasers

The mode-locking techniques just listed can be used to generate ultrashort pulses in solid-state lasers. In the latter rare-earth or transition metal ions are introduced as impurities in host material, generally crystals or glasses. Ytterbium (Yb) is a rare earth whose electronic structure is $4f^{16}5s^25p^65d^06s^2$. When an atom is introduced in a host media, it loses two electrons from 6s and one from 4f. The remaining 15 electrons, then, reorganize themselves in the different states of 4f shell giving rise to large number of energy levels [20]. In particular, the characteristic transitions of the Ytterbium ion Yb^{3+} interests the $^2F_{5/2}\rightarrow{}^2F_{7/2}$ levels [28]. To be precise, the presence of external electric field causes a split of them into many sub-levels manifolds (Stark effect [29]) shown in Fig. 1.2(a). The Figure 1.2(b) displays the characteristic absorption and emission cross sections of the Ytterbium ion. The absorption and the emission are peaked around 976 nm, but they show also secondary peaks centred, respectively, around 920 nm and 1030 nm. One of the most used scheme, shown in Fig. 1.2(a), consists in pumping Ytterbium ions at 976 nm and exploiting the emission at 1030 nm. The choice of hosting material must be done carefully since it influences and determines a lot of properties of Ytterbium ion such as the radiative lifetime [30]. Generally, Yb-doped crystals are characterized by broad and smooth emission and absorption spectra [31] making them suitable for short-pulse generation via mode-locking. Today a large number of robust, efficient and cost-effective solid-state Yb-based crystal lasers are available, some examples are Yb:YAG, Yb:KYF, Yb:YLF, and Yb:$CaGdAlO_4$ also called Yb:CALGO.

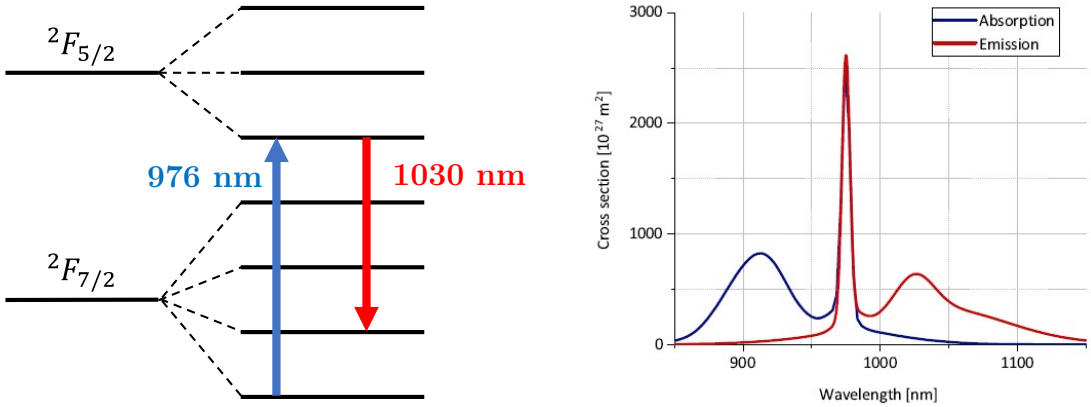

(a) (b)

Figure 1.2: (a) Sub-levels interested by absorption at 976 nm and emission at 1030 nm and (b) absorption and emission spectra of Yb ion.

1.1.3 Yb-based fiber lasers

Fiber lasers exist from the beginning of the history of lasers but only recently become very famous thanks to the development of diode laser able to provide an effective pump in terms of quality beam and brightness [20] [32]. Differently from solid-state oscillators, the active medium is the core of the fiber which is generally doped with rare earth ions. Two interesting configurations are the single-mode fiber laser and double-clad fiber laser. In the latter the pump is guided by the inner cladding around the core, as shown in Figure 1.3, while in the former it is guided by the core itself [20]. Double-clad fibers overcomes the problems of alignment that limits the pump power coupled in conventional single mode fibers [33]. Another advantage of double-clad fiber is the high damage threshold [33].

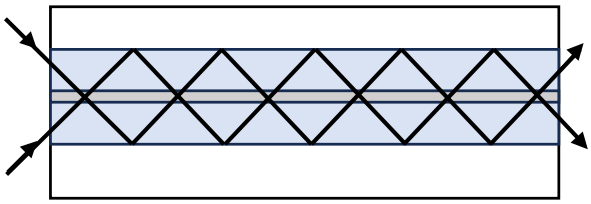

Figure 1.3: Scheme of cladding pump.

The low pump absorption of some doped fibers causes the present of a very long active media characterized by a small effective mode area. As consequence, fiber lasers suffer from strong nonlinearities that limit duration and output power of ultrashort pulses. Indeed, the advantage of high amplification bandwidth is nullified by these effects and by chromatic dispersion. Nonetheless, sub 100 fs pulses can be achieved by means of passive mode locking technique. One possibility is represented by nonlinear

polarization rotation which is very effective but also very unstable due to polarization changes caused by an uncontrolled birefringence and temperature.
The early fiber lasers were based on very inefficient Erbium and Neodymium doped fibers. A great step was made when Ytterbium-doped fiber started to be used, allowing to develop oscillators with an optical efficient larger than 90%. This kind of fiber is characterized by a very broad gain bandwidth and is an extremely attractive media for generation and amplification of ultrashort pulses [34]. Moreover, Ytterbium has a better solubility in glass than Erbium and Neodymium [32]. However, the high normal dispersion of the silica around 1030 nm is quite annoying. This problem affects all the oscillators based on fiber but, in particular, Yb-doped fiber laser due to the peak of the emission spectrum around that wavelength. As consequence, these kinds of lasers need to introduce in the cavity systems able to compensate it in order to achieve very short pulses. One possibility, also the most diffused, is to use a couple of gratings or prisms set on a moving stage allowing a fine adjustment of the distance.

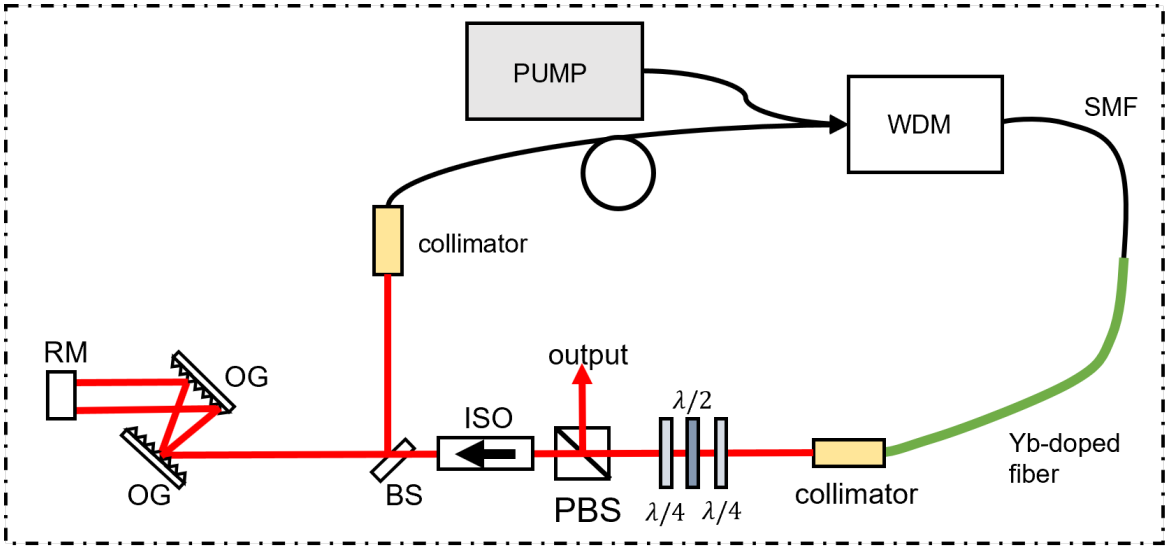

Figure 1.4: Example of Yb-based fiber laser proposed by [35]. BS: beamsplitter; ISO: optical isolator; OG: optical grating; PBS: polarizing beamsplitter; RM: roof mirror; SMF: single-mode optical fiber.

An example of Yb-based fiber system proposed by [35] is shown in Fig. 1.4. The pump diode emits at 976 nm, in correspondence of the absorption peak of Ytterbium, with an average power of 300 mW. A wavelength division multiplexing (WDM), used to couple light into a ring cavity, is followed by 30-cm long Yb-doped fiber. Then three wave plates are used to adjust the polarization which is quite delicate as said in the introduction. The output coupler is a polarizing beamsplitter which reflects part of the light and transmit the remaining part. The latter enters in an optical isolator allowing a unidirectional operation and then in a system of gratings pair used to compensate dispersion accomulated in the cavity.

1.2 Specialty optical fibers

The term "specialty optical fibers" indicates classes of waveguides having at least one special property with respect to the standard fibers. Some examples are those that are not constituted entirely by glasses showing some air holes (Photonic Crystal Fibers) or those made of rare earth doped glass (Active fibers). There are many categories, but this thesis will focus, in the following subsections, only on the types of fibers used in the setup.

1.2.1 Active optical fibers

Active fibers have been partially mentioned in Subsection 1.1.3. Differently from passive ones, these fibers have a core made of rare earth doped glass. Specialty optical waveguides are used in many applications. Other than in lasers and amplifiers, they are used in medical, industrial, and scientific fields [36]. The key concept is the following: the pumping light is absorbed by the rare earth ions that reach a metastable level [37] and the subsequent de-excitation cause an emission of light at higher wavelength. Apart from the common parameters used to describe waveguides such as numerical aperture, mode area, and bend losses, here the doping concentration, the effective absorption and emission, and energy transfer must be kept under control. Indeed, doping concentration is strictly related to absorption efficiency and to the phenomena of quenching [38]. If the concentration increases, also the absorption increases. However, after a certain value the probability of having cluster of ions increases and therefore the quenching. The energy transfer is important especially in case of codoped active fibers where instead of using a single type of rare earth for doping, a couple of ions is employed [39]. This method helps to tune the emission wavelength and it increases the efficiency of absorption. In case of Er:Yb fibers, the pump is absorbed by the Ytterbium which than use the energy acquired to excite the Erbium [39]. The following steps are identical to the case of single rare earth doped fiber.

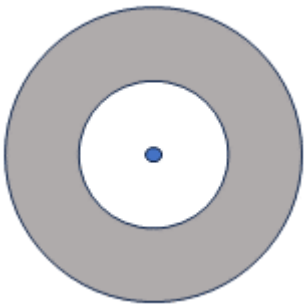

Figure 1.5: Double-clad optical fiber cross section. The blue circle is the core; the white circle is the inner cladding; the grey circle is the outer cladding.

Active fibers can be single-mode or multimode and sometimes also polarization-maintaining

(Subsection 1.2.2) or characterized by large mode area (Subsection 1.2.3). There is also a special variant called double-clad, showed in Figure 1.5, which has, apart from the inner cladding, also an outer cladding allowing to reach excellent beam quality and very high output powers [40].

1.2.2 Polarization-maintaining optical fibers

Generally optical fibers with circular core [41] are not affected by the phenomena of birefringence for which depending on the polarization of light, the refractive index is different. As consequence, the polarization of the light remains unchanged. However, the great sensibility of this kind of fibers to temperature, mechanical stress, bending, and manufacturing defects causes the rise of a small amount of birefringence. The latter generates a phenomenon called polarization-mode dispersion that will be treated in detail in Subsection 1.3.2. As consequence, a random cross talking CT among the two polarization modes in fiber and so an uncontrollable change of the polarization can be observed [42]:

$$\mathrm{CT} = 10 \cdot \log \frac{\mathrm{P_y}}{\mathrm{P_x}} \tag{1.9}$$

The idea of polarization-maintaining fibers is not to cancel out this effect but to introduce on purpose an uniform birefringence that allows a controllable and non-casual exchange of power between the two polarization modes.

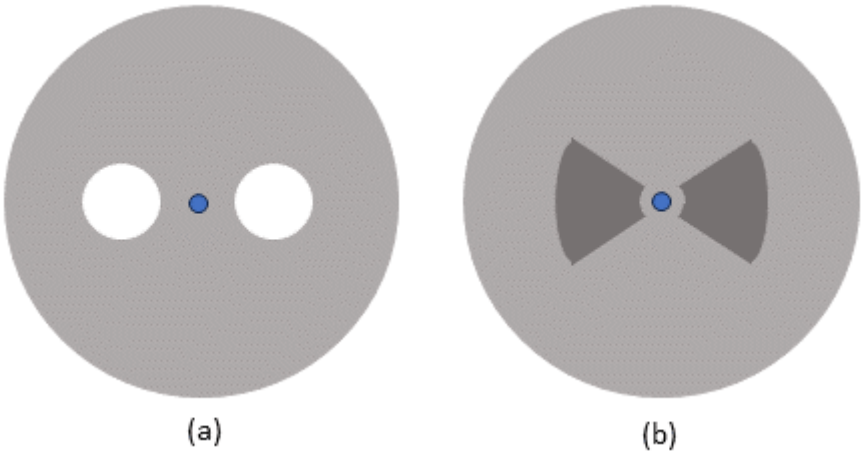

Figure 1.6: (a) PANDA optical fiber and (b) Bow-tie optical fiber; the blue circles represent the core while the white and dark grey parts represent regions with a different birefringence

The strong birefringence can be achieved by introducing in the fiber preform, in opposite position with respect to the core, two cylindrical rods made of borum-doped glasses [43]. Due to different thermal expansion coefficients, a built-in mechanical stress arises

when fiber is cooled down [43]. The cross section shown in Fig. 1.6(a) has the shape of a panda and for this reason these fibers are called PANDA fibers. Another possibility is to introduce rods with more complicated shape as shown in Fig. 1.6(b). These waveguides are called bow-tie fibers. The polarization-maintaining condition can be achieved also in photonic crystal fibers (Subsection 1.2.4) where the air holes instead of being symmetric with respect to the core, follow an asymmetrical disposition.
Polarization-maintaining optical fibers are widely used for polarization control in fiber optic sensors, precision optical instruments, and optical communication systems [44]. However, the particular structure makes the splicing between two fibers very difficult and causes large propagation losses compared to the standard fibers [43].

1.2.3 Large mode area optical fibers

Some applications require a large effective mode area whose definition is not straightforward due to the different shapes of the fiber modes. The mathematical definition is the integral of the electric field profile E(r) over the full area where the intensity of mode is not negligible [45]:

$$A_{eff} = \frac{(\int |E(r)|^2 \, dA)^2}{\int |E(r)|^4 \, dA} \tag{1.10}$$

That can be also expressed in terms of intensity profile I(r) [46]:

$$A_{eff} = \frac{(\int I(r) \, dA)^2}{\int I(r)^2 \, dA} \tag{1.11}$$

The dependence of the electric field from only the radial coordinate comes from the assumption that field distribution is constant over the time and during the propagation along the fiber.
The advantages of having a large mode area are reduced nonlinearities and higher damage threshold. Indeed, the relation between the phase shift introduced by the Kerr effect and the effective mode area is inversely proportional [43]:

$$\varphi = \frac{2\pi}{\lambda} n_2 \frac{P}{A_{eff}} L \tag{1.12}$$

where n_2 is the nonlinear coefficient, P the optical power and L the length of the medium. So having a large A_{eff} means small phase shift. Despite a large mode area, it is possible to realize fibers guiding a single or a small number of modes. However, the propagation is less robust since for reaching this result the refractive index contrast between core and cladding must be decreased making the waveguide more sensible to inhomogeneities in composition and to any disturbance [43]. Indeed, the balance between diffraction and waveguiding that sustains the propagation of a single mode is worsen due to a weaker diffraction.
Other difficulties regard the production of large mode area active fibers with rare-earth doped core. As said, these fibers suffer from quenching that can be reduced by introducing additional dopants in the glass. However, this causes an increment in the

numerical aperture and so of the core cladding refractive index contrast reducing the waveguiding capability and the quality of the output beam [43].
Other effects that characterize this family of fibers is the thermal lensing [47]. This phenomenon affects high power fiber lasers and amplifiers where the heating of the medium may not be uniform or there may be some mechanical stress that produce a gradient of the refractive index. This effect is called like that because causes a focusing effect and as consequence it determines a reduction of the effective mode area nullifying the advantages of these waveguides.
So large mode area fibers can be used in many applications where nonlinearities are unwanted or where high powers are used but must be carefully designed to avoid all the problems listed.

1.2.4 Photonic crystal optical fibers

Photonic Crystals are particular media characterized by periodic modulation of the dielectric constant, and as consequence of the refractive index, obtained by alternating it with different materials. In photonic crystal fibers (PCF), light is guided by a periodic wavelength-scale lattice of microscopic holes in the cladding [48]. The structure of this kind of waveguides offers many degrees of freedom and, as consequence, many peculiar applications and properties.

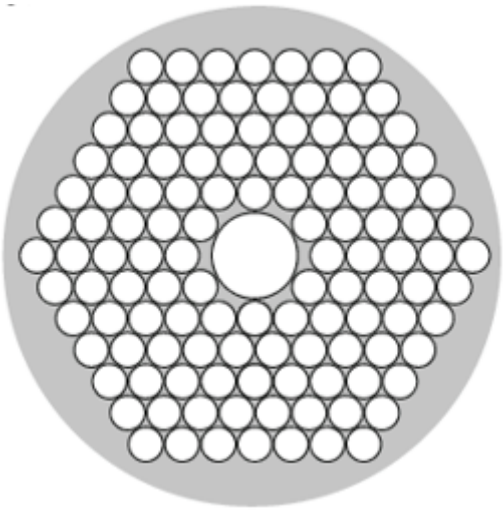

Figure 1.7: Hollow core optical fiber cross section.

We distinguish mainly between two types of photonic crystal fibers depending on the pattern of the air holes and if the core is filled with silica or is empty. In case of core filled with air, these fibers, shown in Figure 1.7, are called hollow core and they belong to the category of photonic bandgap fibers. These kind of waveguide exploit 2D photonic crystals which show a periodicity of the refractive index along two dimensions. Therefore, the structure will show a 2D photonic bandgaps which are frequency ranges

where light propagation is not allowed. Indeed, by properly design the structure it is possible getting photonic bandgap in correspondence of the wavelength of interest [43]. In this way, the amplitude of light decays exponentially in the cladding and so it remains confined in the core.
The other type is characterized by a triangular pattern of the air holes around a fused silica rod working as core shown in Fig. 1.8. In this last type of PCFs, the guiding principle is similar to the total internal reflection like the normal fibers. Indeed, the presence of air holes in cladding determines an effective refractive index lower than the one of the core.

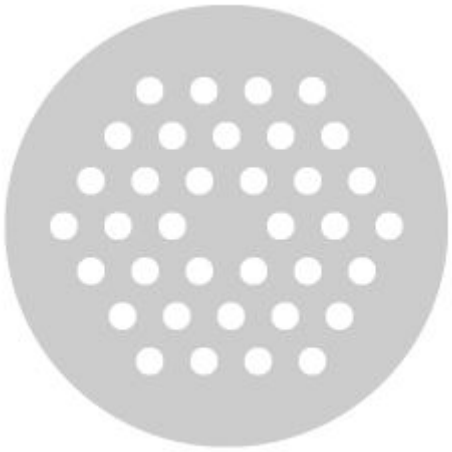

Figure 1.8: Photonic crystal optical fiber with central silica rod cross section.

The fabrication of these waveguides is very complicated. This can be done with a method very similar to the one used for normal fibers which is based on a preform that, in case of PCFs, is got by stacking many pure silica tubes. The protection of the bundle is achieved by jacketing it with a big tube. Then, the fiber is introduced in the conventional drawing tower where it is heated to reduce the tension of the waveguide. Depending on the temperature and the drawing speed selected, it is possible to achieve structures with different dimensions and space between air holes. To get a structure like that, the tension must be high enough which means high speed and a temperature not higher than 2000°C [49]. In Figure 1.9 it is possible to see the formation of the fiber structure during the drawing phase. Another possibility is represented by extrusion in which molten glass is forced through a die containing a defined pattern of holes [48]. This technique allows to draw the fibers directly from the bulk and it is mainly used in case of soft glasses and polymers [43].
In photonic crystal fibers, depending on the parameters of the structure it is possible to achieve very important properties. One of them regards the dispersion. Indeed, it is possible to shift the zero group velocity dispersion (GVD) point achieving an anomalous dispersion where the GVD of pure silica and that of conventional single-mode fibers is normal. They are useful also for the generation of supercontinuum which is a strong nonlinear broadening of the spectrum that will be treated in the third chapter.

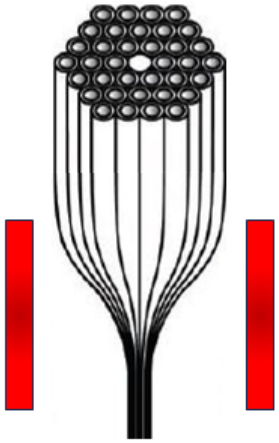

Figure 1.9: Prefrom used for the production of PCFs; the red rectangles represent the heating elements.

1.3 Dispersive effects in fibers

1.3.1 Chromatic Dispersion

The chromatic dispersion is a phenomenon related to the dependence of the media response from optical frequency. When a pulse propagates within a waveguide made by a given material, its components experience a different refractive index causing a propagation velocity different for all of them. The relation between refractive index and optical frequency is provided by the Sellmeier's equation:

$$n^2(\omega) = 1 + \sum_{n=1}^{m} \frac{B_j\, \omega_j^2}{\omega_j^2 - \omega^2} \tag{1.13}$$

where ω_j are the resonance frequencies at which the media absorbs the electromagnetic radiation and B_j is the strength of the j-th resonance [50]. As consequence, the propagation speed of the different components expressed by $c/n(\omega)$ is different and so they will arrive at the end of the waveguide in different moment causing a temporal broadening of the pulse. Mathematically speaking, an early measure of chromatic dispersion was expressed by the Abbe number V_d:

$$V_d = \frac{n_D - 1}{n_F - n_C} \tag{1.14}$$

where n_D, n_F, n_C are the refractive index of the Fraunhofer lines which are 486.1 nm (F line), 589.2 nm (D line) and 656.3 nm (C line). High V number means low dispersion and viceversa.
The modern way of quantifying chromatic dispersion is based on the Taylor expansion

of the wavenumber k:

$$k = k_0 + \frac{\partial k}{\partial \omega}(\omega - \omega_0) + \frac{1}{2}\frac{\partial^2 k}{\partial \omega^2}(\omega - \omega_0)^2 + \frac{1}{6}\frac{\partial^3 k}{\partial \omega^3}(\omega - \omega_0)^3 + \dots \tag{1.15}$$

The term k_0 is a common phase term whose expression is $2\pi/\lambda_0$ with λ_0 central wavelength. The first order term contains the group velocity defined as:

$$v_g = \frac{\partial k}{\partial \omega} \tag{1.16}$$

which express the propagation speed in a medium of the pulse envelope. The term $\frac{\partial^2 k}{\partial \omega^2}$, also indicated as β_2, is called group velocity dispersion (GVD), generally expressed in s^2/m. The derivative of GVD with respect to ω is called third order dispersion (TOD) per unit length $k''' = \frac{\partial^3 k}{\partial \omega^3}$. This parameter is mainly used together with other higher orders term near the zero-dispersion point of a given material where β_2 is nearly zero. Indeed, at that point seem to be no dispersion but by considering higher order terms like TOD, the effect is not null.
There are two different regimes of dispersion, the normal or positive dispersion and the anomalous or negative dispersion. The former is characterized by a positive GVD and, as consequence, the group velocity decreases by increasing the optical frequency. In case of a pulse, the high-frequency components (blue-shifted) travel slower than low-frequency (red-shifted) components [50]. In case instead of an anomalous dispersion, the effects are the opposite: β_2 is negative, the group velocity increases with the optical frequency and the blue-shifted components travel faster than red-shifted ones. This regime is interesting because it can be exploited to balance nonlinear effects in waveguides generating a solitary pulse that propagates along the fiber. Differently from others, this kind of pulse maintains the same spectral and temporal shape during the propagation. To be precise, there exist also high-order solitary pulses that shows a periodic behaviour. Indeed, their shape changes during propagation but after a certain distance, the pulse gets again the initial one.
In case of guided modes apart from the contribution given by the material dispersion, there is another contribution to chromatic dispersion due to the dielectric waveguiding. However, this factor is relatively small except near the zero-dispersion wavelength where it becomes comparable with the material contribution [50].
In telecommunication field, dispersion is quantified by means of the dispersion parameter D expressed in ps/(km nm) and linked to β_2 by the following relation:

$$\mathrm{D} = -\frac{2\pi \mathrm{c}}{\lambda^2}\beta_2 \tag{1.17}$$

An effect related to chromatic dispersion is the so-called temporal walk-off. This phenomenon affects the nonlinear frequency conversion processes such as sum or difference frequency generation, optical rectification that need the temporal superposition of optical pulse to be efficient. Indeed, if pulses have a different frequency, they propagate with different speed and, as consequence, after a certain distance they are no more overlap.

1.3.2 Polarization-mode dispersion

In single-mode fiber, as said by the name, light propagate with a unique mode. To be precise, there are two degenerate modes corresponding to the two orthogonal polarizations, along x and y directions. This holds in an ideal case when the waveguide is characterized by a perfect cylindrical symmetry. However, in a real fiber some variations of the core shape or stress-induced anisotropy break the perfect symmetry causing a mixing of the polarizations. As consequence, the propagation constants of the no more degenerate modes are different causing a so-called modal birefringence. The strength of this effect is measured by [50]:

$$\mathrm{B} = \frac{|\beta_\mathrm{x} - \beta_\mathrm{y}|}{k_0} \tag{1.18}$$

with $k_0 = 2\pi/\lambda_0$ and β_x, β_y propagation constants of the two polarizations. The modes exchange their power in a periodic fashion as they propagate with a period [50]:

$$\mathrm{L_b} = \frac{\lambda}{\mathrm{B}} \tag{1.19}$$

$\mathrm{L_b}$ is called beat length that is the distance after which the phase difference accumulated between the two polarization modes is equal to 2π [42]. This kind of effect is quite difficult to study since B changes due to the fluctuations of the anisotropic stress and in the shape of the core. Modal birefringence mainly affects ultrashort pulses causing a temporal broadening. This can be estimated by measuring the delay ΔT between the two polarizations:

$$\Delta\mathrm{T} = \mathrm{L}|\beta_\mathrm{x} - \beta_\mathrm{y}| \tag{1.20}$$

where L is the length of the fiber. However, as said, the values of the two betas are not constant. As consequence, it is better considering the root mean square value of ΔT defined as:

$$\sigma_\mathrm{T}^2 = <\Delta\mathrm{T}^2> = 2(\Delta^{'}\mathrm{l_c})^2[\exp(-\frac{\mathrm{L}}{\mathrm{l_c}}) + \frac{\mathrm{L}}{\mathrm{l_c}} - 1] \tag{1.21}$$

Here, $\Delta\mathrm{T}^{'}$ is the intrinsic modal dispersion and $\mathrm{l_c}$ is the correlation length which is the distance over which the two polarizations remained correlated [51]. In case of L>0.1 km and $\mathrm{l_c}$«L, this expression can be simplified [50]:

$$\sigma_\mathrm{T} = \mathrm{D_p}\sqrt{\mathrm{L}} \tag{1.22}$$

where $\mathrm{D_p}$ is the polarization-mode dispersion parameter that has generally values between 0.1-1 ps/$\sqrt{\mathrm{km}}$ [50]. The dependence from $\sqrt{\mathrm{L}}$ make this kind of the effect relatively small with respect to chromatic dispersion.

1.4 Third order nonlinear effects

1.4.1 Nonlinear Schrödinger equation

The starting point is represented by the Maxwell equations:

$$\begin{cases} \nabla \cdot \boldsymbol{D} = \rho \\ \nabla \times \boldsymbol{E} = \dfrac{\partial \boldsymbol{B}}{\partial t} \\ \nabla \cdot \boldsymbol{B} = 0 \\ \nabla \times \boldsymbol{H} = \boldsymbol{J} + \dfrac{\partial \boldsymbol{D}}{\partial t} \end{cases} \tag{1.23}$$

$\boldsymbol{D}$ is called electric displacement and it is defined as:

$$\boldsymbol{D} = \varepsilon_0 \boldsymbol{E} + \boldsymbol{P} \tag{1.24}$$

Here, ε_0 is the vacuum permittivity, $\boldsymbol{E}$ is the electric field, and $\boldsymbol{P}$ is the polarization vector. Instead, $\boldsymbol{B}$ is called magnetic induction and it is expressed by:

$$\boldsymbol{B} = \mu_0(\boldsymbol{H} + \boldsymbol{M}) \tag{1.25}$$

where μ_0 is the vacuum permeability, $\boldsymbol{H}$ is the magnetic field, and $\boldsymbol{M}$ is the magnetization vector. The remaining quantities ρ and $\boldsymbol{J}$ are, respectively, the net free charge density and the conduction current density.
The polarization vector is constituted by a contribution $\boldsymbol{P}^{(l)}$ which is linearly dependent from the electric field $\boldsymbol{E}$ and under the assumption of isotropic media it is expressed by:

$$\boldsymbol{P}^{(l)}(\boldsymbol{r}, t) = \varepsilon_0 \int_{\mathbb{R}^3} d\boldsymbol{r}' \int_{-\infty}^{+\infty} \chi(\boldsymbol{r}, \boldsymbol{r}', t, t') \boldsymbol{E}(\boldsymbol{r}', t')\, dt' \tag{1.26}$$

and by a nonlinear term that under the further assumption of instantaneous nonlinear response it is written as:

$$\boldsymbol{P}^{(nl)} = \sum_{i>2}^{\infty} \varepsilon_0 \chi^{(i)} \boldsymbol{E}^i \tag{1.27}$$

with i representing the order. To be precise, the assumption of isotropic media is unphysical especially for i=2 since $\chi^{(2)}$ is different from zero only in materials lacking symmetry. Nonetheless, in this mathematical proof it will be considered only the third order avoiding any problem.
By combining the Maxwell equations, what we get is:

$$\boldsymbol{\nabla}(\boldsymbol{\nabla} \cdot \boldsymbol{E}) - \nabla^2 \boldsymbol{E} = -\mu_0 \frac{\partial \boldsymbol{J}}{\partial t} (\boldsymbol{\nabla} \times \boldsymbol{M}) - \mu_0 \frac{\partial \boldsymbol{J}}{\partial t} - \frac{1}{c^2} \frac{\partial^2 \boldsymbol{E}}{\partial t^2} - \mu_0 \frac{\partial^2 \boldsymbol{P}}{\partial t^2} \tag{1.28}$$

Under the following approximations:

1. Non-magnetic materials ($\boldsymbol{M} \simeq 0$)
2. Absence of free charges ($\rho \simeq 0$)
3. Homogenous media
4. $\boldsymbol{J} \simeq 0$
5. Plane wave approximation

the Equation (1.28) becomes:

$$\frac{\partial^2 \boldsymbol{E}}{\partial z^2} - \frac{1}{c^2}\frac{\partial^2 \boldsymbol{E}}{\partial t^2} = \mu_0 \frac{\partial^2 \boldsymbol{P^{(l)}}}{\partial t^2} + \mu_0 \frac{\partial^2 \boldsymbol{P^{(nl)}}}{\partial t^2} \tag{1.29}$$

Now, to make the treatment little bit easier we can pass to frequency domain by applying the Fourier transform in both spatial and temporal domain:

$$\mathcal{F}_{t,z}\big\{E(t,z)\big\} = \hat{E}(\omega,k) = \int_{-\infty}^{+\infty} dt \int_{-\infty}^{+\infty} E(z,t)e^{i(kz-\omega t)}\, dz, \tag{1.30}$$

$$\mathcal{F}_{t,z}\big\{P^{(l)}(t,z)\big\} = \hat{P}^{(l)}(\omega,k) = \int_{-\infty}^{+\infty} dt \int_{-\infty}^{+\infty} P^{(l)}(z,t)e^{i(kz-\omega t)}\, dz, \tag{1.31}$$

$$\mathcal{F}_{t,z}\big\{P^{(nl)}(t,z)\big\} = \hat{P}^{(nl)}(\omega,k) = \int_{-\infty}^{+\infty} dt \int_{-\infty}^{+\infty} P^{(nl)}(z,t)e^{i(kz-\omega t)}\, dz, \tag{1.32}$$

obtaining:

$$\left[\frac{\omega^2 \epsilon_r(\omega)}{c^2} - k(\omega)^2\right]\hat{E}(\omega,k) = -\omega^2 \mu_0 \hat{P}^{(nl)}(\omega,k) \tag{1.33}$$

The Equation (1.33) is propagation equation in Fourier domain.
In case of envelope approximation in which we consider the pulse as the product of an envelope and a carrier, the electric field can be written as:

$$E(z,t) = A_R(z,t)cos[\omega_0 t - k_0 z + \varphi(z,t)] = \mathbb{R}\big[A(z,t)e^{i(\omega_0 t - k_0 z)}\big] \tag{1.34}$$

where the appendix R indicates that A_R(z,t) is a real function while A(z,t) is a complex function since it englobes the phase term $e^{i\varphi(z,t)}$. Also the nonlinear polarization term can be written in a similar form but since $P^{(nl)}$ is not an electromagnetic wave, the wavevector here is different from k_0 of the electric field and is called k_p. The frequency instead is the same since $P^{(nl)}$ is a source term and must oscillate at same frequency of the wave, the expression is:

$$P^{(nl)}(z,t) = B_R(z,t)cos[\omega_0 t - k_p z + \varphi(z,t)] = \mathbb{R}\big[B(z,t)e^{i(\omega_0 t - k_p z)}\big] \tag{1.35}$$

Before proceeding, we need to make further two assumptions on (1.33). The first goes under the name of "slowly-varying envelope approximation" for which $\omega \simeq \omega_0$. It is called light that because "slowly-varying" means something that does not change

rapidly and so the value of the frequency is in the neighbourhood of ω_0. The second assumption is neglecting the backward propagation by writing:

$$\frac{\omega}{c}n(\omega) + k(\omega) \simeq \frac{\omega_0}{c}n(\omega_0) + k_0 = 2k_0 \tag{1.36}$$

The equation (1.33) becomes:

$$\left[\frac{\omega}{c}n(\omega) - k(\omega)\right]\hat{E}(\omega, k) = -\frac{\mu_0 c\omega_0}{2n(\omega_0)}\hat{P}^{(nl)}(\omega, k) \tag{1.37}$$

After making the Fourier transform of (1.34) and (1.35) and substituting them into (1.37), what we get is:

$$\left[\frac{\omega}{c}n(\omega) - k(\omega)\right]\hat{A}(\omega - \omega_0, k - k_0) = -\frac{\mu_0 c\omega_0}{2n(\omega_0)}\hat{B}(\omega - \omega_0, k - k_0) \tag{1.38}$$

The equation got is in Fourier domain, to return in spatial and temporal domain is necessary applying the anti-transform. Before doing this, $k(\omega)$ in Eq. (1.38) is substituted with its Taylor expansion already seen in Subsection 1.3.1. After the transform, the resulting equation is:

$$\frac{1}{v_g}\frac{\partial A}{\partial t} + \frac{\partial A}{\partial z} + \sum_{n=2}^{+\infty}\frac{\beta_n(-i)^{n-1}}{n!}\frac{\partial^n A}{\partial t^n} = e^{-i\Delta k z}\left[-\frac{\mu_0 c\omega_0}{2n(\omega_0)}\right]B \tag{1.39}$$

with $\Delta k = k_p - k_0$. Since this chapter is considering third order nonlinear effects, we can calculate $P^{(3)}$:

$$P^{(3)} = \frac{\epsilon_0\chi^{(3)}}{8}\left[A^3 e^{i3(\omega_0 t - k_0 z)} + 3A^2 e^{i2(\omega_0 t - k_0 z)}A^* e^{-i(\omega_0 t - k_0 z)} + cc\right] \tag{1.40}$$

Now, consider only the term oscillating at the fundamental frequency and compare the expression obtained with Eq. (1.35):

$$B = \frac{3\epsilon_0\chi^{(3)}}{4}A|A|^2 \tag{1.41}$$

Simplify Equation (1.39) by considering only second order (n=2) and the degenerate case $\Delta k = 0$ and then substitute in it (1.41) getting:

$$\frac{1}{v_g}\frac{\partial A}{\partial t} + \frac{\partial A}{\partial z} - i\frac{\beta_2}{2}\frac{\partial^2 A}{\partial t^2} = -\gamma A|A|^2 \tag{1.42}$$

where $\gamma = \frac{3\omega_0\chi^{(3)}}{8cn(\omega_0)}$. We can change the reference frame passing to a co-moving one by performing the following change of coordinates:

$$\begin{cases} Z = z, & \text{(1.43a)} \\ T = t - \dfrac{z}{v_g} & \text{(1.43b)} \end{cases}$$

obtaining:

$$\frac{\partial A}{\partial Z} - i\frac{\beta_2}{2}\frac{\partial^2 A}{\partial T^2} + \gamma A|A|^2 = 0 \tag{1.44}$$

The Eq. 1.44 is called "nonlinear Schrödinger equation" (NLSE) since its form is the same as for the conventional time-dependent Schrödinger equation in quantum mechanics, but with a nonlinear potential term [19].
To be precise, the Equation (1.44) does not take into account eventual losses that must be considered in case of propagation in a medium. To have a more completed equation, we can introduce a term $\frac{\alpha}{2}A$ in Eq. (1.44) where α is the linear absorption coefficient:

$$\frac{\partial A}{\partial Z} - i\frac{\beta_2}{2}\frac{\partial^2 A}{\partial T^2} + \frac{\alpha}{2}A + \gamma A|A|^2 = 0 \tag{1.45}$$

In phenomenon such as supercontinuum generation, other effects like higher-orders nonlinearities and stimulated Raman scattering should be included in Eq. (1.44) generating the so-called "generalized nonlinear Schrödinger equation" (GNLSE). This equation will be matter of the third chapter.

1.4.2 Dispersionless self-phase modulation

The Kerr effect is a nonlinear optical effect which can occur when light propagates in crystals and glasses. It can be described as a change of the refractive index n caused by electric field E. Indeed, n is the sum of unperturbed refractive index n_0 and a term containing the optical intensity which is proportional the modulus squared of E:

$$\mathrm{n} = \mathrm{n}_0 + n_2\mathrm{I} \tag{1.46}$$

The parameter n_2 is called nonlinear index:

$$n_2 = \frac{3\chi^{(3)}}{4\mathrm{c}\epsilon_0\mathrm{n}_0^2} \tag{1.47}$$

An interesting manifestation of this dependence occurs through the self-phase modulation (SPM) which is a phenomenon leading to spectral broadening of optical pulses [50]. This effect is not the only way to understand optical Kerr effect. Apart from SPM which works in temporal domain, there is another phenomenon operating in the spatial domain called self-focusing effect. Indeed, in an optical pulse the intensity is a function of the radial coordinate r (Fig. 1.10). As consequence, the intensity and so the refractive index of the tails will be different from the ones of the peak and this causes a focusing effect.
The mathematical treatment of SPM starts from the nonlinear Schrödinger equation. To make the case easier, it's possible, at least at the beginning, neglect the propagation losses and the dispersion contribution setting β_2 to zero:

$$\frac{\partial A}{\partial Z} + i\gamma A|A|^2 = 0 \tag{1.48}$$

This assumption has sense, at least initially, if the length of the medium L is much lower than the dispersion length $\mathrm{L_D} = \frac{\mathrm{T_0^2}}{|\beta_2|}$ where $\mathrm{T_0}$ is the pulse duration. Now, assume that the solution to Equation (1.48) is:

$$A(Z,T) = A(0,T)e^{i\varphi(Z,T)} \tag{1.49}$$

and impose the following boundary conditions:

$$\begin{cases} \varphi(0,T) = 0 \\ \varphi(Z,T) = -i\gamma Z|A(0,T)|^2 \end{cases} \tag{1.50}$$

After substituting (1.49) in (1.48) and applying the condition expressed by the System (1.50), the result of (1.48) is:

$$A(Z,T) = A(0,T)e^{-i\gamma 2|A(0,T)|^2} \tag{1.51}$$

Consider again the Equation (1.29) and perform the change of coordinate (1.34), by inserting (1.51), what we get is:

$$E(Z,T) = \mathbb{R}\big[A(0,T)e^{i\phi(Z,T)}\big] \tag{1.52}$$

where:

$$\phi(Z,T) = \omega_0 T + \frac{\omega_0 Z}{v_g} - k_0 Z - \gamma Z|A(0,T)|^2 \tag{1.53}$$

The result shows how the envelope remain unchanged during a nonlinear propagation and the unique effect is the introduction of a phase term $\phi(Z,T)$ that depends, by means of last term of (1.53), from the envelope itself.

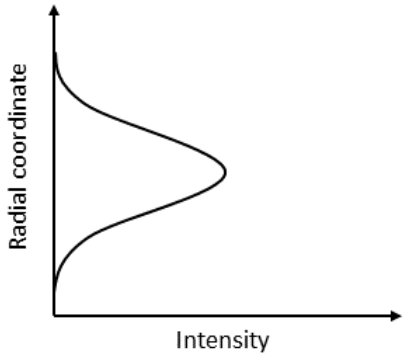

Figure 1.10: Radial coordinate of a gaussian pulse as function of intensity

To better understand the effect of self-phase modulation, we can calculate the instantaneous frequency:

$$\omega(T) = \frac{\partial\phi}{\partial T} = \omega_0 - \gamma Z\frac{\partial|A(0,T)|^2}{\partial T} \tag{1.54}$$

From Eq. (1.54) we see that when Z increases and so pulse propagates, the frequency chirp becomes larger and larger. Figure 1.11 shows the qualitative representation of this effect.

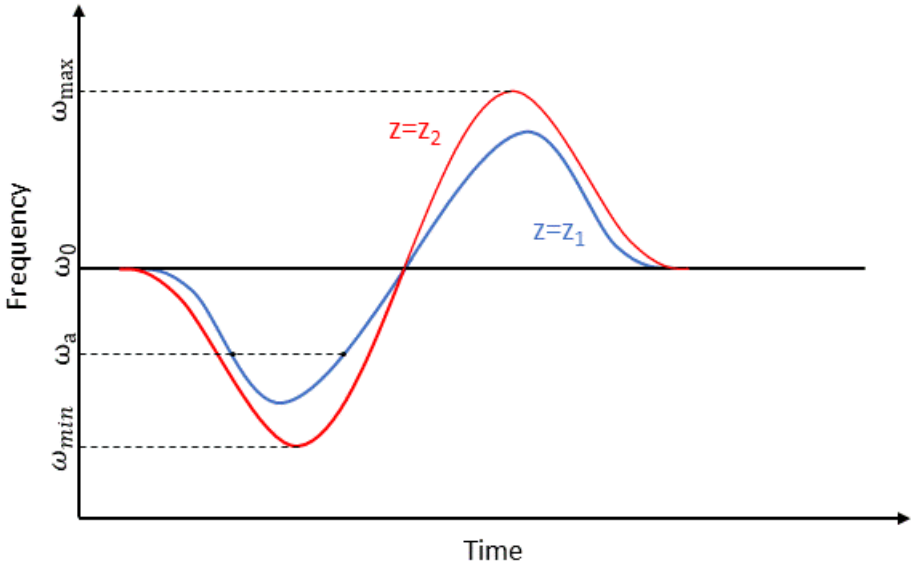

Figure 1.11: Instantaneous frequency as function of time for two different propagation lengths ($z_2 > z_1$).

Assume a large peak phase shift ($\phi_{max} \gg 1$) indicated with ϕ_{max} since in correspondence of the peak of the pulse, the intensity shows a maximum and so also the phase shift is maximum. Under this assumption, the characteristics of SPM are:

1. The optical bandwidth depends on maximum excursion of the instantaneous frequency curve and in case of symmetric pulse is defined by [19]:

$$\Delta\omega = \omega_{max} - \omega_{min} = \frac{\pm f_1 \phi_{max}}{\Delta t} \tag{1.55}$$

with f_1 numerical factor and Δt pulse duration. If the initial bandwidth is expressed by [19]:

$$\Delta\omega_{in} = \frac{f_2}{\Delta t} \tag{1.56}$$

with f_2 another numerical factor, the broadening can be estimated by:

$$\frac{\Delta\omega_{SPM}}{\Delta\omega_{in}} = 2\frac{\Delta\omega_{max}}{\Delta\omega_{in}} = \frac{2f_1}{f_2}\phi_{max} \tag{1.57}$$

In case of a Gaussian pulse, the broadening can be roughly considered to be equal to the maximum phase shift:

$$\frac{\delta\omega_{SPM}}{\Delta\omega_{in}} \approx 1.03\phi_{max} \tag{1.58}$$

2. Related to the power spectrum, it is characterized by a modulation shown in Fig. 1.12. It can be qualitatively described by looking at the interference between components with different delays. Indeed, consider a frequency ω_a (Figure 1.11). At that value there are two components that can give rise to a constructive or a destructive interference generating a spectrum like that.

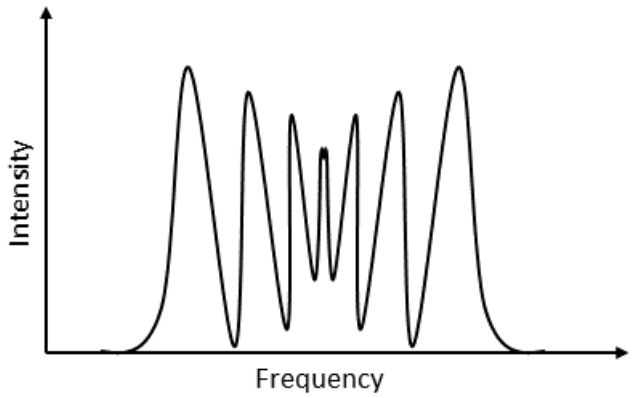

Figure 1.12: Self-phase modulation power spectrum.

The number of peaks and of minima are estimated by:

$$number\,of\,peaks \approx \frac{\delta\phi_{max}}{\pi} + 1 \tag{1.59}$$

$$number\,of\,minima \approx \frac{\delta\phi_{max}}{\pi} \tag{1.60}$$

1.4.3 Group velocity dispersion effects

The effect of chromatic dispersion can be considered by assuming in NLSE $\beta_2 \neq 0$:

$$\frac{\partial A}{\partial Z} - i\frac{\beta_2}{2}\frac{\partial^2 A}{\partial T^2} + i\gamma A|A|^2 = 0 \tag{1.61}$$

In this case $L \gg L_D$ and $L \gg L_N L = \frac{1}{\gamma P_{peak}}$ where P_{peak} is the peak power of the pulse. These conditions tell us that both the nonlinearities and the dispersion have an important role. Once again, the losses in (1.61) are neglected. Nonetheless, this kind of equation needs numerical methods to be solved. One of them is the split-step Fourier method where the medium considered is divided into slices of thickness Δz. The accuracy of solution is inversely proportional to the width of them. In each slice, the dispersion and the SPM are separated. Indeed, the method considers before the effects of GVD and then the self-phase modulation as if it is completely concentrated on the edge of the slice (Figure 1.13). An example of solution is:

$$A(z_{k+1}, T) = \mathcal{F}^{-1}\left\{\hat{A}(z_k, \omega)e^{-i\frac{\beta_2\omega^2\Delta z}{2}}\right\} \cdot e^{-i\gamma\Delta z|A(z_k,T)|^2} \tag{1.62}$$

where z_k and z_{k+1} are the edges of two generic, consequent slices.

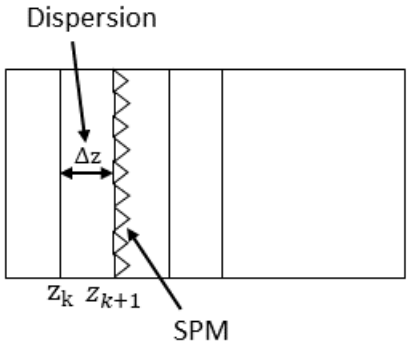

Figure 1.13: Pictorial representation of split-step Fourier method; the medium is divided into slices of thickness Δz characterized by certain amount of dispersion while SPM is fully concentrated on the edge of each slice.

The qualitative description of the effects can be made by means of Figure 1.14 that shows the behaviour in temporal and in frequency domain of a sech pulse when it propagates in a media under the effects of SPM and GVD. While the spectrum broadens due to nonlinear phenomenon, the dispersion becomes more and more important causing a temporal broadening. As consequence, the intensity of pulse reduces and the effects of SPM are less strong. At very long distances, dispersion effects are dominant. Related to the temporal broadening, in Figure 1.14 is shown how the presence of nonlinear effects generates a flat top. The other phenomenon interests the power spectrum which presents a reduced modulation since now the contributions of the components that interfere are unbalanced.

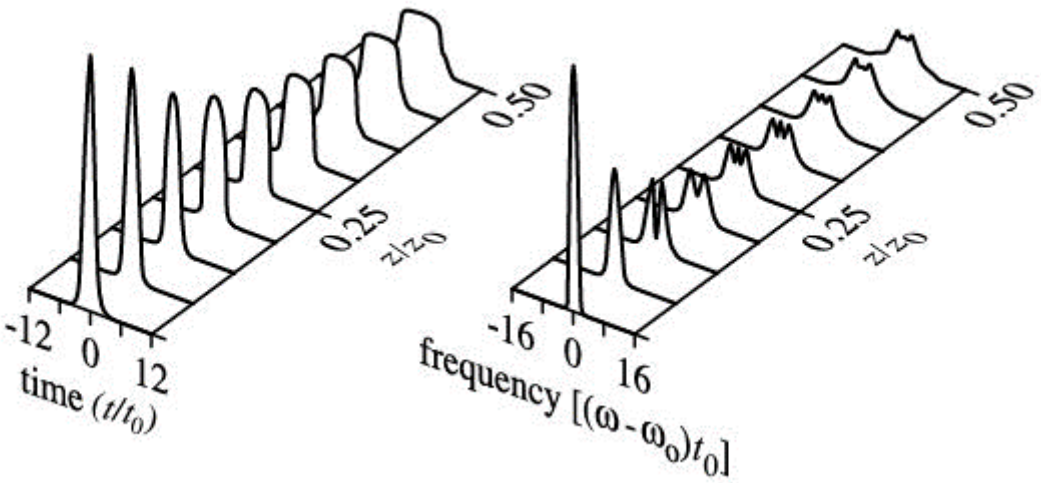

Figure 1.14: Evolution of temporal intensity profiles and power spectra for $sech(\frac{t}{t_0})$ input pulse under SPM with normal dispersion [19].

2 | Experimental setup

2.1 Design and alternative versions

The experimental setup is projected to provide few-optical-cycles pulses with high average power needed to generate a mid-infrared radiation and for other applications treated in the last chapter. The system shown in Fig. 2.1 starts from $sech^2$-shaped pulses emitted by Yb:CALGO. These are then coupled into a fiber amplifier by means of two Ø1" protected gold mirrors. The latter show an average reflectance R_{ave}>96% in IR range. The light coupled is about 75% and it has a horizontal polarization which remains unchanged until the exit of the amplifier since it is made of polarization-maintaining fibers. The output polarization is vertical because the final tip is rotated by 90 degrees. This choice has the advantage of limiting the losses in the following compression stage. After the fiber amplifier, there is a lens with a focal length of 25 mm to collimate the light. A dichroic mirror is used to separate the residual pump from the amplified signal which is now characterized by pulses with a duration larger than 2 ps and an average power higher than 5 W. These pulses pass then through the compression stage constituted by a pair of optical gratings whose reciprocal distance has been determined by means of simulations and by optimizing the intensity autocorrelation. Two different configurations for the compression have been tested: one by placing it before coupling the signal in the fiber amplifier and the other after. In Chapter 3, the decision of taking it after the amplification stage will be justified.
The compression allows to get pulses with duration of 80 fs and an average power of 5 W. Then a series of 3 Ø0.5" Yb-fs mirrors bring the pulses at input of the photonic crystal fiber used for the spectral broadening. These mirrors reflect more than 99.5% in the range of interest and if placed at 45 degrees, they ensure a minimum effect on the pulse dispersion. Between two of these, an optical isolator is placed in order to avoid back reflections of light which are quite annoying. Indeed, when light is coupled in fiber optics, the silica-air interface can generate some reflections which add extra noise to measurements. However, the introduction of this element into the setup causes a 20% loss in terms of power which is now slightly higher than 4 W. Once pulses arrive at the PCF, they are coupled by means of an aspheric lens with a very small focal length of 3.9 mm that allows to couple more than 60% of the power. The output pulses can be then optically compressed by a pair of prisms or by a hollow core fiber and focused into an orientation-patterned gallium phosphide to generate broadband mid-infrared radiation.

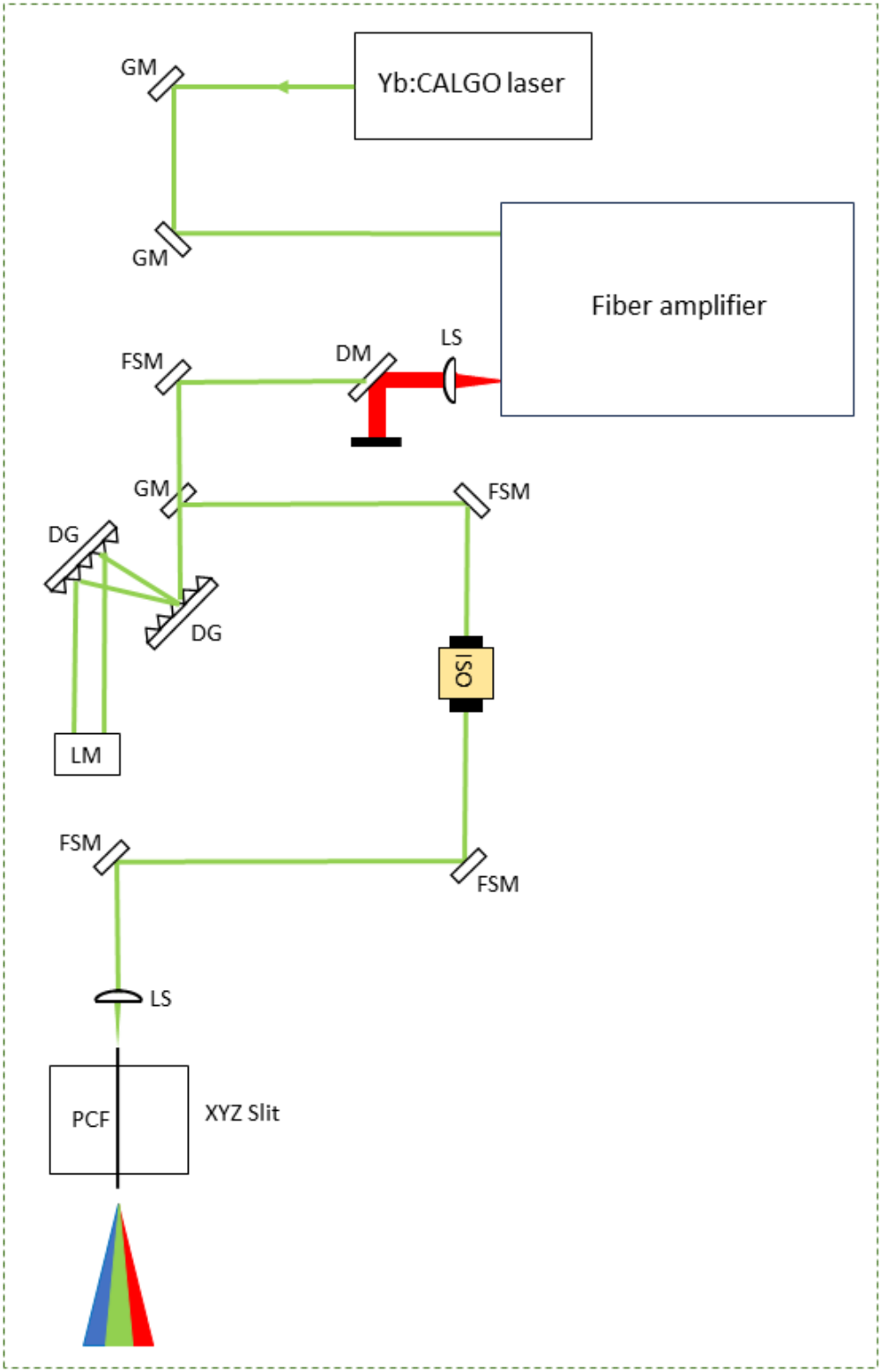

Figure 2.1: Experimental setup. DG: diffraction gratings; DM: dichroic mirror; FSM: Yb-fs mirror; GM: gold mirror; ISO: optical isolator; LM: low-GDD mirror; LS: lens; PCF: photonic crystal fiber.

2.2 Solid-state Yb:CALGO

This section is centred on the first block of the setup. It opens describing the operation of the oscillator followed by the characterization of it in terms of average power, spectrum, pulse duration, and relative intensity noise (RIN).

2.2.1 Setup description

As introduced in Section 2.1, the laser used is an Yb:CALGO femtosecond laser. Apart from a high thermal conductivity and large emission cross section, this crystal is characterized by an ultraflat gain [31] and these features make it suitable to produce ultrashort pulses. The setup of the laser is shown in Fig. 2.2.

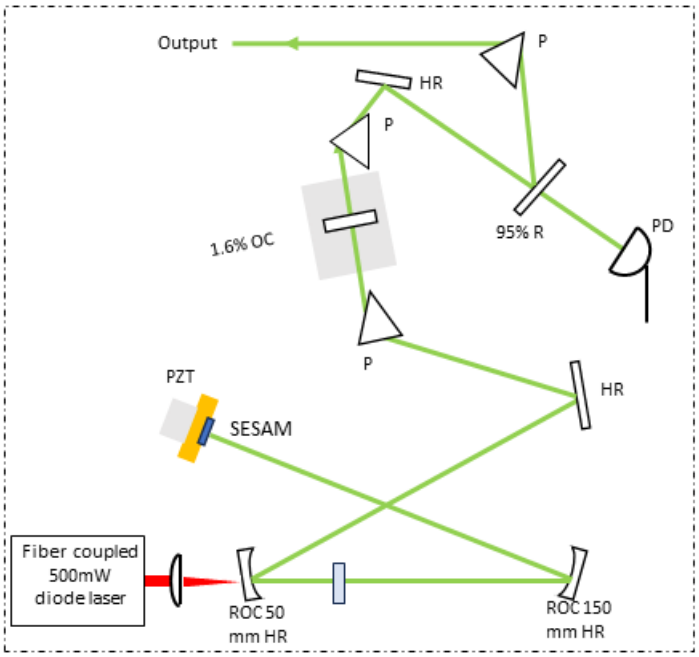

Figure 2.2: Yb:CALGO setup. HR: high-reflectivity dielectric mirror; ISO: optical isolator; OC: output coupler; P. fused silica prism; PD: fast photodetector; PZT: piezoelectric transducer.

The oscillator is pumped with a Bragg-gratings-stabilized diode laser which emits with an average power of 500 mW centred around 976 nm. The linear x-folded cavity contains an a-cut 2 mm thick crystal characterized by a 5% doping and pumped along π-polarization [52]. The mode-locking operation is achieved by exploiting a semiconductor saturable absorber mirror (SESAM) with a modulation depth of 3% and non-saturable loss less than 1%, mounted on a piezoelectric transducer. The output coupler has a transmission of 1.6% and is fixed on a linear stage used for a fine tuning of the

pulse repetition and of carrier envelope offset. The prisms in the setup are used for the GVD management. This laser can produce hyperbolic secant pulses with a duration of 70 fs and an average output power of 45 mW. The repetition rate is fixed at 160 MHz corresponding to a cavity length of about 94 cm.

2.2.2 Average power and optical spectrum

To characterize the Yb:CALGO laser, we determined its optical spectrum and average power. Since the aim of the thesis is to produce mid-infrared radiation, the oscillator was already built and so characterized in previous experiments [52]. Nonetheless, we preferred collecting again some measurements of average power, optical spectrum, and pulse duration (Subsection 2.2.3) which are relevant to our experiment. For all measurements, the repetition rate of the laser was kept approximately 160 MHz.
The first quantity measured was the average power. This value is an important indicator for the design of the amplifier. Indeed, to produce mid-infrared radiation, high power pulses are needed and so depending on the starting value, the length of the active fiber and the pump current used in the amplifier would change. Average power is also useful for the calculation of pulse energy E_p and peak power P_p. The former is simply the average power divided by the pulse repetition rate. Instead, the calculation of the peak power is not straightforward since it depends on pulse shape. In our case, for $sech^2$-shaped pulses it is equal to [53]:

$$P_p \approx 0.88 \frac{E_p}{\tau_p} \tag{2.1}$$

where τ_p is the pulse duration.
The power measurements were performed by means of an optical power meter with a sensor placed immediately after the case of the laser. This instrument can reach a sensitivity of 1 µW but for our purpose 100 µW is enough. In Table 2.1, the results are presented. We decided to measure the output average power at three different values of pump current in order to have a larger flexibility for the design of the fiber amplifier. In the end, among these three values of current, we decided to use 0.65 A. The reason of this choice is to avoid any q-switched pulse. The latter is characterized by a long duration and a high average power and as consequence it could compromise the operation of the system destroying some components. Low current is aimed to remain in a stable region of operation of the laser avoiding this phenomenon.

I_{pump} **(A)**	P_{out} **(mW)**
0.55	35.7
0.65	42.5
0.75	53.5

Table 2.1: I_{pump} vs P_{out}.

Optical spectrum provides information about the central wavelength and the bandwidth of pulses. It was measured by means of AQ6317C optical spectrum analyser. The light can be coupled either directly in the instrument or in an optical fiber mounted on three-dimensional slit. In our case, we have adopted the second configuration placing the system near the exit of the laser case. The measurements were performed with a resolution of 0.5 nm at the values of current used for the previous analysis. In Figure 2.3 the three normalized spectra and their comparison are shown. The central wavelength is about 1050 nm and the full width at half maximum (FWHM) goes from 14.3 nm for 0.55 A to 15.8 nm for 0.75 A. From the comparison in Figure 2.3(d), we notice that for different pump currents the shape of spectrum does not change. As we can observe, on the top of all the three spectrum a strange modulation is present. This phenomenon is called Ethanol effect.

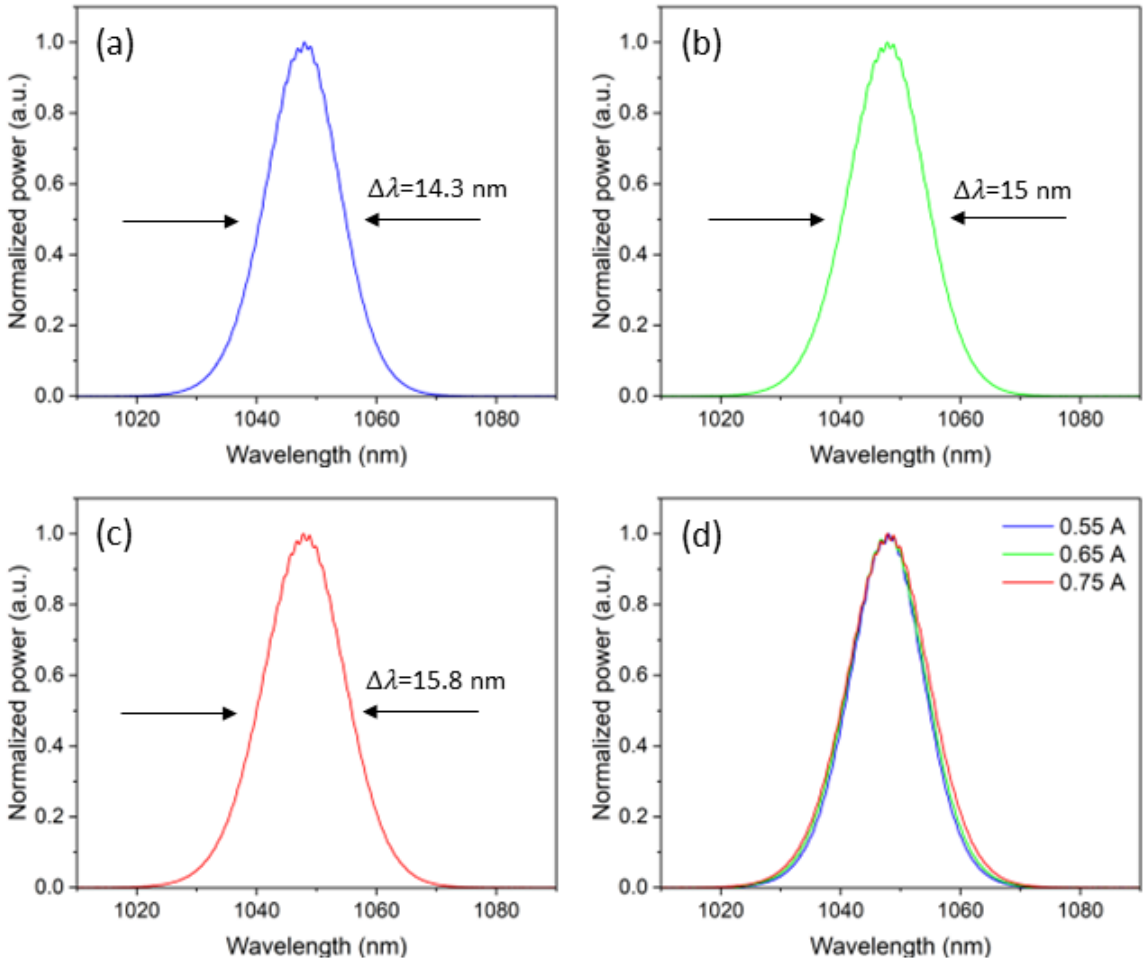

Figure 2.3: Normalized optical spectrum for a pump current of (a) 0.55 A (b) 0.65 A (c) 0.75 A; (d) comparison among all the three spectra.

2.2.3 Intensity autocorrelation

There exist several techniques used for temporal characterization of pulses. The duration can be measured directly in time domain by means of a fast photodiode or a streak camera. However, the former is exploited only in case of pulses with duration up to picoseconds. Indeed, at its best, it is able to reach a resolution of 10 ps. Instead, the streak camera can characterize pulses with duration in the order of tens of femtoseconds making it suitable to our purpose. Nonetheless, the high cost of this tool forced us to use an alternative technique based on concepts coming from Michelson interferometer. The latter is not able alone to fully reconstruct an ultrashort pulse unless we assume that the spectral phase of the pulse $\phi(\omega)$ is constant and the pulse is transform-limited [19]. For this reason, in order to characterize a femtosecond ultrashort pulse, we need to introduce a crystal with $\chi^2 \neq 0$ and exploit the second harmonic generation (SHG) which is a second order nonlinear effect that generates light at twice the input optical frequency. The configuration used, called non-collinear second harmonic autocorrelator, is shown in Fig. 2.4.

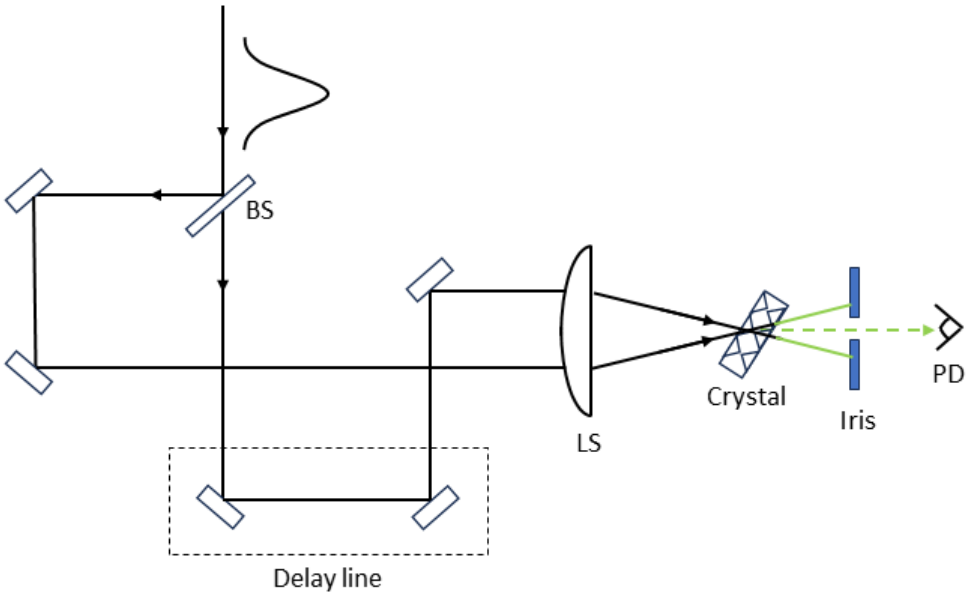

Figure 2.4: Non-collinear second harmonic autocorrelator. BS: beamsplitter; LS: lens; PD: photodetector.

The operation principle is quite simple but also effective. A 50% beam splitter produces a copy of the input pulse which is then delayed by a quantity τ. After following different paths, the two pulses are focused by means of a lens on a crystal where they interfere. Here, the second harmonic of the interaction is generated and it is then detected by a photodiode. This happens only if the crystal satisfies the phase matching condition:

$$\boldsymbol{K_1} + \boldsymbol{K_2} = \boldsymbol{K_{SH}} \tag{2.2}$$

where $\boldsymbol{K_1}$, $\boldsymbol{K_2}$, and $\boldsymbol{K_{SH}}$ are the wavevectors of the two pulses and of the second harmonic. In reality, the interaction of each pulse with crystal produces other two second

harmonics which are then blocked by an iris. Indeed, this technique is background-free in the sense that if there is no interaction between the single pulses, no signal is recorded.
Mathematically speaking, the signal $U(\tau)$ detected is an integral since, as mentioned, the photodiode is not fast enough to detect ultrashort pulses:

$$U(\tau) \propto \int_{-\infty}^{+\infty} |E_{SH}(t,\tau)|^2 dt \propto \int_{-\infty}^{+\infty} |A_{SH}(t,\tau)|^2 dt \tag{2.3}$$

where A_{SH} is the envelope of the second harmonic pulse that is constituted by:

$$A_{SH}(t,\tau) \propto A(t) \cdot A(t-\tau) \tag{2.4}$$

with $A(t-\tau)$ envelope of the delayed pulse. But, in Eq. 2.3 there is the modulus squared of $A_{SH}(t,\tau)$ which is:

$$|A_{SH}(t,\tau)|^2 \propto I(t) \cdot I(t-\tau) \tag{2.5}$$

that produces the following expression:

$$U(\tau) \propto \int_{-\infty}^{+\infty} I(t) \cdot I(t-\tau) dt = C_I(\tau) \tag{2.6}$$

called intensity autocorrelation $C_I(\tau)$. This function has the following three properties:

- It reaches the maximum when τ=0 since in that moment the two pulses are completely overlapped.
- It is an even function, $C_I(\tau)$=$C_I(-\tau)$.
- By performing the Fourier transform of it, what we get is:

$$\mathcal{F}\{C_I(\tau)\} = |\hat{I}(\omega)|^2 \tag{2.7}$$

These properties underline the limits of this technique. Indeed, the second feature does not permit the characterization of an asymmetric pulse. Instead, in the third one the phase term $e^{i\hat{\varphi}(\omega)}$ is missing and so the spectral phase cannot be reconstructed with this method. However, in our experiment we consider symmetric pulses and as consequence, the Fourier transform is real and that phase term can be skipped. Finally, the pulse duration can be retrieved by simply measuring the FWHM of the intensity autocorrelation and dividing it by a constant that in case of $sech^2$-shaped pulses is 1.54.
The measurements were performed by directly launching the output beam of the oscillator in a commercial autocorrelator based on the working principle described above. The traces collected, shown in Fig. 2.5, are three and they correspond to the values of pump current seen in previous subchapter. As we can see here again, the intensity autocorrelations do not change too much by varying the output power. The curves were fitted with $sech^2$ function producing the following values of FWHM: 113.2 fs (for

a current of 0.55 A), 105.9 fs (for a current of 0.65 A), and 103.4 fs (for a current of 0.75 A).

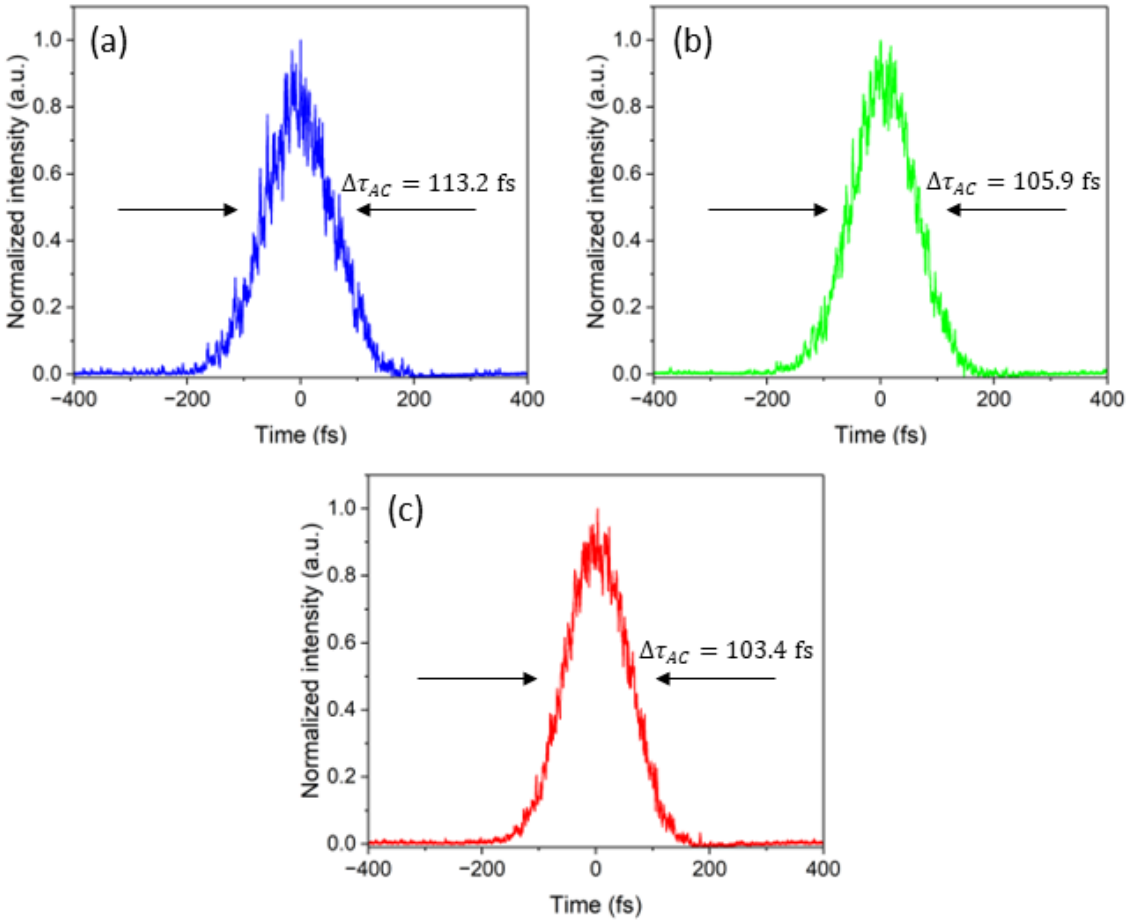

Figure 2.5: Intensity autocorrelation for a pump current of (a) 0.55 A (b) 0.65 A (c) 0.75 A.

The corresponding pulse durations are shown in Table 2.2. As we can notice, these values are around 70 fs and so they are coherent with the measurements performed in previous experiments.

I_{pump}(A)	$\Delta\tau_{AC}$(fs)	Δt_p(fs)
0.55	113.2	73.5
0.65	105.9	68.8
0.75	103.4	67.1

Table 2.2: Autocorrelation FWHM $\Delta\tau_{AC}$ and pulse duration Δt_p as function of pump current I_{pump}. Since we are dealing with sech^2-pulses, Δt_p is got dividing $\Delta\tau_{AC}$ by 1.54.

2.2.4 Relative intensity noise

Lasers are generally affected by external perturbations which influence their operation and for this reason it is fundamental to stabilize them. Apart from fluctuations of the cavity length which brings to a change of the pulse repetition rate, there are as well some perturbations causing amplitude fluctuations named intensity noise. In case of solid-state lasers, these perturbations come from different sources: pump fluctuations, cavity misalignment or degradation of components [20]. This intensity noise is usually quantified in terms of relative intensity noise (RIN) defined as the ratio between the mean-square power fluctuation and the average optical power of pulse train squared:

$$\mathrm{RIN} = \frac{\langle \delta \mathrm{P(t)}^2 \rangle}{\langle \mathrm{P(t)}^2 \rangle} \tag{2.8}$$

The frequency analysis of RIN can be performed by means of the power spectral density (PSD) :

$$\mathrm{S_{RIN}}(f) = \mathcal{F}\{\mathrm{R}(\tau)\} = \int_{-\infty}^{+\infty} \mathrm{R}(\tau) \mathrm{e}^{\mathrm{i}2\pi\omega\tau} \mathrm{d}\tau \tag{2.9}$$

which is the Fourier transform of a function $\mathrm{R}(\tau)$ defined as the autocorrelation of the output power fluctuations divided by the square of the average output power:

$$\mathrm{R}(\tau) = \frac{\langle \delta \mathrm{P(t)} \delta \mathrm{P(t+\tau)} \rangle}{\langle \mathrm{P} \rangle^2} \tag{2.10}$$

The relation between Eq (2.8) and Eq (2.9) is expressed by:

$$\mathrm{RIN} = \int_{\frac{1}{\mathrm{T}}}^{\frac{f_\mathrm{r}}{2}} \mathrm{S_{RIN}}(f) \mathrm{d}f \tag{2.11}$$

where T is the measurement time while f_r is the repetition rate.
Intensity noise is generally measured with a fast photodiode in which a photocurrent is generated and converted into a voltage by means, for example, of a resistor. The fluctuating voltage is then fed into an electronic spectrum analyser getting the PSD which is expressed in V^2/Hz or in alternative as logarithmic quantity in dBm/Hz. If this value is then divided by the DC voltage level squared, we get RIN PSD expressed in Hz^{-1}. It is common to multiply the logarithm in base 10 by 10 in order to express it in dBc/Hz.
Figure 2.6 displays the RIN of the Yb:CALGO laser. The measurements of both the oscillator and the noise floor were performed at the output of the amplifier with everything switched off. The reason for this choice is the will to compare all the traces, included the RIN of amplified signal that will be displayed in Chapter 3, at the same fixed place. Our measurements were performed from 10 HZ to 80 MHz (Nyquist frequency). Around 10^2 Hz, we notice a series of peaks caused by the electronic noise associated to the pump diode. At higher frequencies these peaks are filtered by the Ytterbium upper-level lifetime equal to 440 µs [52] which corresponds to a cut-off

frequency $\sim$ 2.3 kHz. At 30 kHz we notice a further peak caused by a small modulation that characterize the mode-locking regime of Yb:CALGO. After this, the RIN of laser reaches the noise-floor at the level of -130 db/Hz.

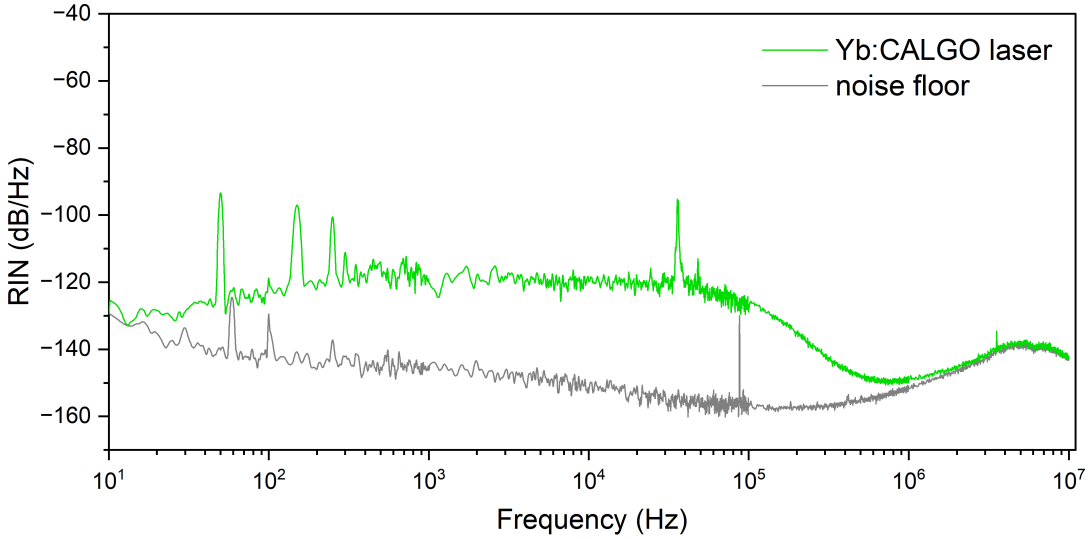

Figure 2.6: Relative intensity noise of the Yb:CALGO ultrafast oscillator.

2.3 Yb-based fiber amplifier

2.3.1 Technical description

The first element of the fiber amplifier, shown in Fig. 2.7, is a collimator mounted on a special slit moving along x and y directions allowing a fine coupling of light into fiber. The latter is a 75-cm long Liekki Passive-10/125DC-PM that is, as specified by the model, a polarization-maintaining waveguide with a core diameter of 10 µm and a cladding diameter of 125 µm. The fiber goes from the collimator to one of the two inputs of the wavelength domain multiplexing (WDM) which is a technology that allows the simultaneous transmission of several optical channels at different wavelengths into a single optical fiber [54]. In our case, WDM is a (1+1)x1 PM combiner where (1+1)x1 means that there is one input dedicated to the signal and one to the pump with a single output. PM underlines that during the transmission the polarization of light remains unchanged. The maximum power supported by it is 100 W. Like the first input, the output is connected to a 75-cm long Liekki Passive-10/125DC-PM. Instead, the second input, dedicated to the pump, is linked to a fiber with a core diameter of 105 µm and a cladding diameter of 125 µm.

The pumping system is constituted by a power supply of TDK Lambda and by a pump diode (model: K976DA5RN-70.00WN0N-10522B10ENA0). Since the spectrum of the signal is peaked at 1050 nm, the transition of Ytterbium ions exploited here is the one with absorption at 976 nm and emission at around 1030 nm. This reason and the need of high power bring us to adopt a pump diode emitting at 976 nm with a maximum power of 70 W even if this is more than enough for our purposes. However, working with such high powers causes problems of overheating. To avoid any damage, the temperature of diode must be kept under 35 Celsius degrees. In our case we adopted a passive cooler presenting on the top a copper foil covered by a thermal compound helping the flow of heat. The temperature is monitored by means of a 10 kΩ thermistor put on the base of the diode connected to a digital multimeter. A better cooling could be achieved by means of a Peltier cell put below the base of diode but we did not adopt it since our cooling system demonstrated to be easier and efficient.
The output passive fiber is then spliced with a 3-meter long Liekki Yb1200-10/125DC-PM which is the active equivalent of the WDM's output fiber. The fact that the dimensions of core and cladding are the same avoids any problem of compatibility between these two types of fiber. The active waveguide is wrapped around a steel spool that has the function of cooling it when the pump power is high. Two key aspects worth to mention are that these fibers are double-clad in order to support high powers and that the amplifier is characterized by a forward pumping configuration. In this kind of setup the pump coupled in the inner cladding and the signal coupled in the core are launched from the same fiber end [33]. The opposite case is represented by the backward pumping where pump and signal are launched from opposite ends.

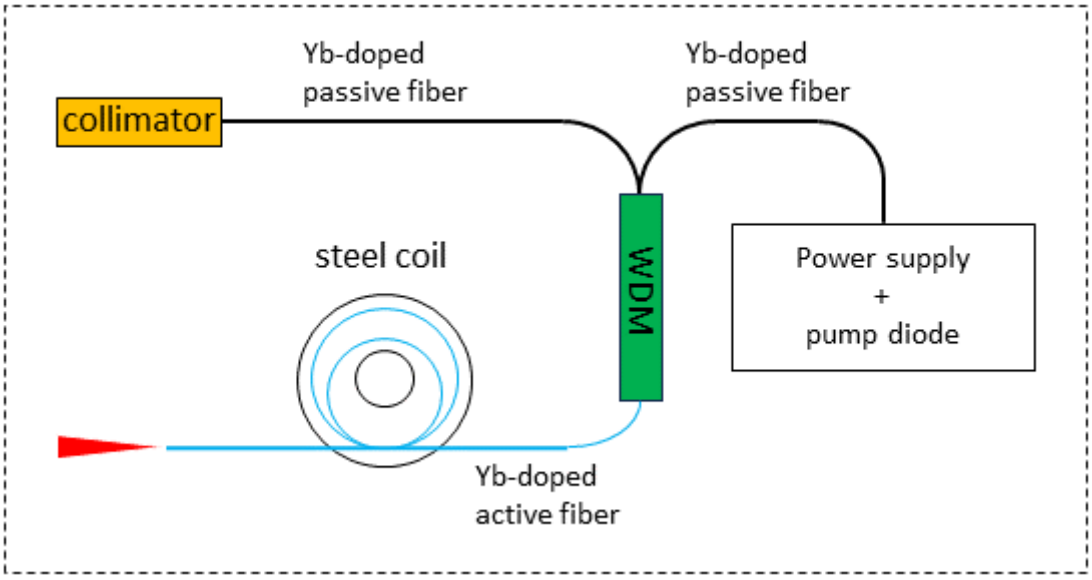

Figure 2.7: Fiber amplifier scheme.

The correct length of the active waveguide, which is quite delicate, has been determined by means of a simulation on MATLAB implementing the mathematical models that will be matter of following subsection. Another key aspect is that the output tip of

this 3-meter long fiber is not flat but it has a certain angle in order to avoid back reflections that would cause damage to components. The output beam is constituted by the amplified signal and the residual pump that, as already mentioned, are then separated by means of a dichroic mirror.

2.3.2 Mathematical modelling

The mathematical model presented employs a rate equation formulation [33] including a large part of effects that characterize the amplification process such as scattering losses and amplified spontaneous emission (ASE). ASE is the amplification of the luminescence spontaneously emitted in laser gain medium which is, in case of fiber amplifiers, an unwanted effect since it limits the gain [29]. Other effects like clustering and quenching are neglected by considering quite low dopants concentration [55]. Before writing down the rate equations, let's define the following parameters: the signal wavelength λ_s, the pump power P_p and λ_p wavelength, and the dopant concentration N that at first order approximation can be consider as independent from time and position z along the fiber. The time-dependent rate equations for a double-clad fiber are:

$$\begin{aligned}\frac{\partial N_2(z,t)}{\partial t} =&\left(\frac{\lambda_p \Gamma_p \sigma_a(\lambda_p}{)} hcA\right) P_p(z,t) N_1(z,t) - \frac{N_2(z,t)}{\tau} + \\ &- \left(\frac{\Gamma_s}{hcA}\right) N_2(z,t) \int \sigma_e(\lambda)[P^+(z,t,\lambda) + P^-(z,t,\lambda)]\lambda d\lambda + \\ &+ \left(\frac{\Gamma_s}{hcA}\right) N_1(z,t) \int \sigma_a(\lambda)[P^+(z,t,\lambda) + P^-(z,t,\lambda)]\lambda d\lambda\end{aligned} \tag{2.12}$$

$$\frac{\partial N_1(z,t)}{\partial t} = -\frac{\partial N_2(z,t)}{\partial t} \tag{2.13}$$

where N_1 and N_2 are, respectively, the population of the ground state and of the excited state, τ is the spontaneous decay time, σ_e and σ_a are the emission and the absorption cross sections. Γ_s and Γ_p represent the signal and the pump filling factor. For a double-clad fiber $\Gamma_p \cong A/S$ [33] where A is the area of core cross section and S is the area of first cladding. P^+ and P^- are the power densities per unit wavelength in positive (+) and negative (-) directions whose evolution along the fiber is described by:

$$\begin{aligned}\pm\frac{dP^\pm(z,t,\lambda)}{dz} =&\Gamma_s[\sigma_e(\lambda)N_2(z,t) - \sigma_a(\lambda)N_1(z,t)]P^\pm(z,t,\lambda) + \\ &+ \Gamma_s \sigma_e(\lambda) N_2(z,t) P_0(\lambda) - \alpha(\lambda) P^\pm(z,t,\lambda)\end{aligned} \tag{2.14}$$

$$\pm\frac{dP_p^\pm(z,t)}{dz} = -\Gamma_p \sigma_a(\lambda_p) N_1(z,t) P_p^\pm(z,t) - \alpha(\lambda_p) P_p^\pm(z,t) \tag{2.15}$$

where $\alpha(\lambda)$ represents the losses at λ, $\frac{dP_p^\pm(z,t)}{dz} \equiv \frac{\partial P_p^\pm(z,t)}{\partial z} \pm \frac{n}{c}\frac{\partial P^\pm}{\partial t}$, and $P_0 \equiv 2\frac{hc^2}{\lambda^3}$ As previously mentioned, the length of active fiber must be carefully defined. Indeed, at the end of the fiber the pump is low and it is no more able to compensate the scattering

losses that cause a reduction of the signal [33]. That's why the fiber must not be too long. On the other hand, in case of a too short waveguide, the potential of the amplifier is not fully exploited.

2.4 Optical compression

The chromatic dispersion accumulated by a pulse propagating in a given medium can be compensated by means of an optical compressor. The most common setup is the one proposed by Treacy [56] shown in Figure 2.8. It is constituted by two couples of diffraction gratings or by a single pair followed by a roof mirror. The basic idea of an optical compressor is to provide an opposite effect compared to the one caused by the propagation in the medium. In fact, the group delay dispersion (GDD) introduced by the gratings, which is the product of GVD by the length of the medium, must have the opposite sign with respect to the one of the medium. In our treatment, we stop at second order, but to get a better compression especially near the zero-GVD point, it is also necessary to consider the higher order terms.

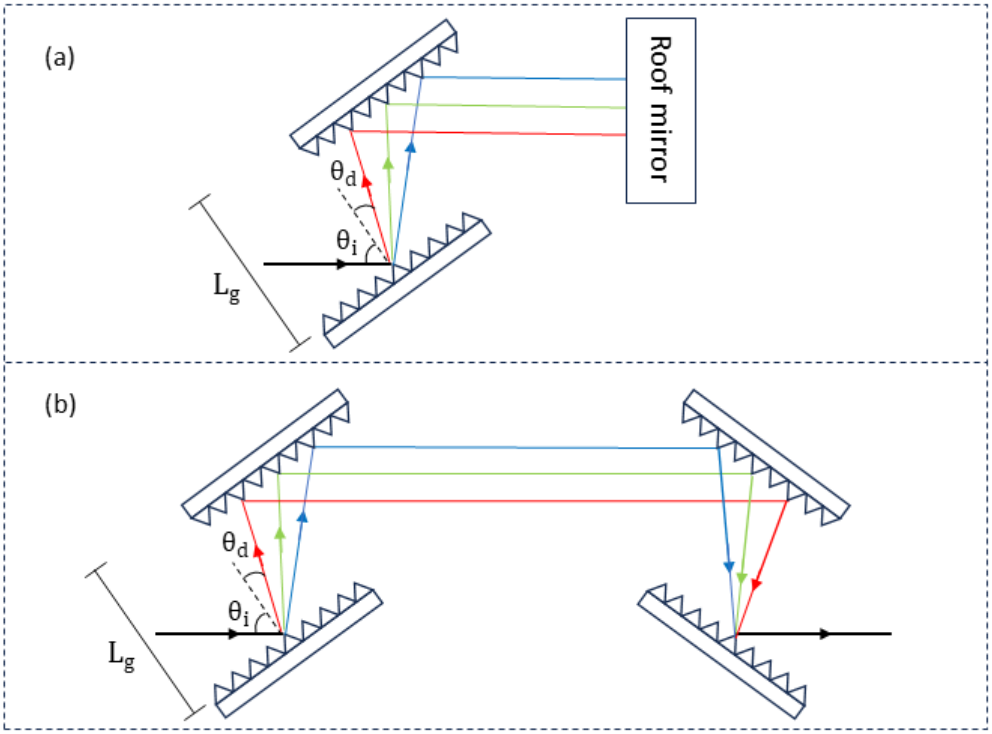

Figure 2.8: Optical compressor made of (a) single pair of diffraction gratings followed by a roof mirror and (b) two pairs of diffraction gratings.

To be effective, the pair of diffraction gratings must be carefully design and the starting

point is represented by the well-known grating equation [57]:

$$sin\,\theta_d = sin\,\theta_i + \frac{\mathrm{m}\,\lambda}{\mathrm{d}} \tag{2.16}$$

where θ_d is the diffracted angle, θ_i is the incident angle, d is the distance between adjacent grooves, and m is the diffraction order that usually is equal to -1 [19]. Assuming that the distance between parallel gratings is $\mathrm{L_g}$, the optical path l of a generic spectral component is expressed by:

$$l = \frac{\mathrm{L_g}}{cos\,\theta_d} + \frac{\mathrm{L_g}}{cos\,\theta_d} cos(\theta_d + \theta_i) \tag{2.17}$$

Define now the group delay $\tau_\mathrm{g} = l/c$ of the component considered and the group delay dispersion $\mathrm{D_{2c}}$ expressed by:

$$\mathrm{D_{2c}} = \frac{\partial \tau_\mathrm{g}}{\partial \omega} = \frac{\partial}{\partial \omega}\left[\frac{\mathrm{L_g}}{\mathrm{c}\cdot cos\,\theta_d} + \frac{\mathrm{L_g}\cdot cos\,\theta_i}{\mathrm{c}} - \frac{\mathrm{L_g}}{\mathrm{c}}\cdot sin\,\theta_i \cdot tan\,\theta_d\right] \tag{2.18}$$

In the expression of the group delay we consider as propagation speed c and not c/n because we assume to be in vacuum (n=1). In Eq. (2.18) the derivative with respect to ω of second term is zero since θ_i, $\mathrm{L_g}$ and c are equal for all the spectral components. After calculation, what we get is:

$$\mathrm{D_{2c}} = \frac{\partial \tau_\mathrm{g}}{\partial \omega} = \frac{\mathrm{L_g\,m}\,\lambda}{\mathrm{c\,d}\,cos\,\theta_d^2}\frac{\partial \theta_d}{\partial \omega} \tag{2.19}$$

where:

$$\frac{\partial \theta_d}{\partial \omega} = \left[1 - \left(sin\theta_d + \frac{\mathrm{m}\,\lambda}{\mathrm{d}}\right)^2\right]^{-\frac{1}{2}} \cdot \frac{\mathrm{m}}{\mathrm{d}} \cdot \frac{\partial}{\partial \omega} \cdot \left[\frac{2\,\pi\,\mathrm{c}}{\omega}\right] = -\frac{2\,\pi\,\mathrm{m\,c}}{\mathrm{d}\,\omega^2 cos\,\theta_d} \tag{2.20}$$

Now, substitute the 2.20 in 2.19 obtaining:

$$\mathrm{D_{2c}} = \frac{\mathrm{L_g\,m^2}\,\lambda^3}{2\,\pi\,\mathrm{d}^2\,cos\,\theta_d^3} \tag{2.21}$$

By comparing this equation with the value of GDD accumulated in the propagation of the medium, it is possible to retrieve the geometrical parameters of the system. Pay attention that this expression is used in case of a single pair. For a double pair of gratings, Eq. (2.21) must be multiply by a factor 2.
In our setup for the compression after the amplifier, we use a system based on a single pair of grating of Wasatch Photonics with incident angle of 24 degree and a density of 800 grooves/mm. They are followed by a low-GDD ultrafst mirror that works as roof mirror and ensures a minimum effect on pulse dispersion.
The compression can be performed also by means of a pair of prisms. Also in this case, the most common configurations are two: one with single pair followed by a mirror (Fig. 2.9(a)) and the other with two pairs of prisms proposed by Fork [58] (Fig. 2.9(b)). Differently from diffraction gratings, prisms are characterized by very low losses and for

this reason they are used in laser cavities for dispersion compensation. Indeed, when they are placed at a particular angle called Brewster's angle, reflections are significantly reduced and the following relation holds [19]:

$$tan\,\phi_1 = tan\,\phi_2 = \mathrm{n} \tag{2.22}$$

where n is the prisms refractive index, ϕ_1 and ϕ_2 are, respectively, the incident and the emerging angles. On the other hand, prisms add a very low dispersion and this translates in a big spacing among them since a large quantity of dispersion is accumulated in the material-free space. Mathematically speaking, the treatment is quite complicated. For this reason, we simply report the result proposed by Weiner [19]:

$$\mathrm{D_{2c}} = \frac{\lambda^3}{2\pi \mathrm{c}^3}\left\{4\mathrm{L}\,cos\,\theta\left(\frac{\mathrm{dn}}{\mathrm{d}\lambda}\right)^2 - 2\mathrm{L}\,sin\,\theta\left[\frac{\mathrm{d}^2\mathrm{n}}{\mathrm{d}\lambda^2} + \left(2\mathrm{n} - \frac{1}{\mathrm{n}^3}\right)\left(\frac{\mathrm{dn}}{\mathrm{d}\lambda}\right)^2\right]\right\} \tag{2.23}$$

Here, θ is the angle formed by a generic ray with respect to the line, of length L, connecting the apices of adjacent prisms. One aspect to mention is that Eq. (2.23) holds for a single pair, in case of four prisms configuration it is necessary to multiply it by factor 2. In our setup the compensation of the dispersion accumulated in PCF is done by means of a pair of prims.

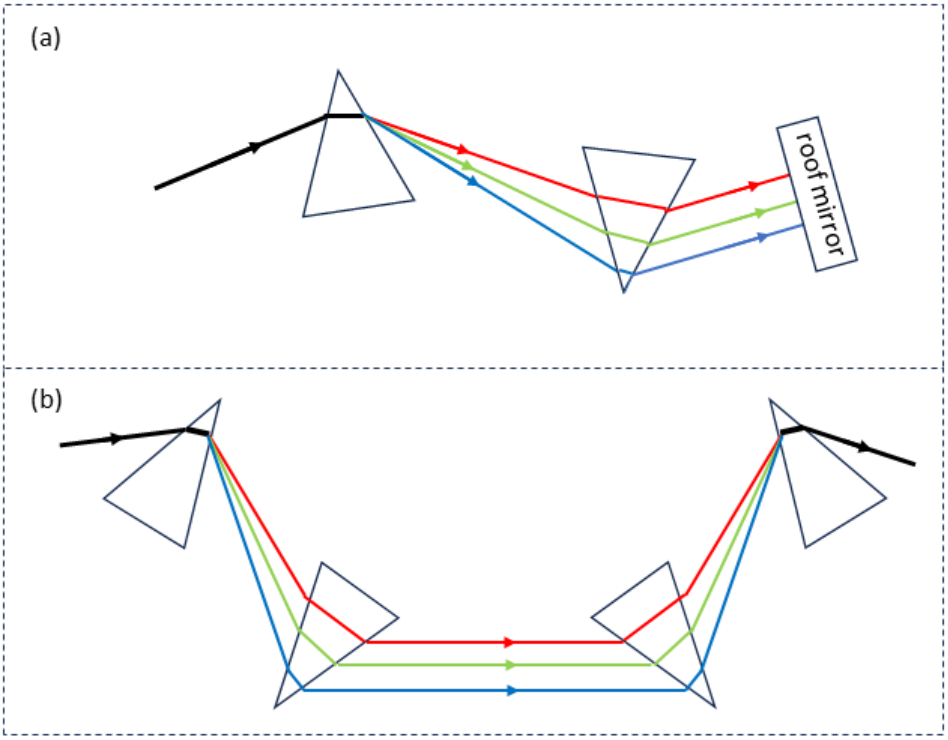

Figure 2.9: Optical compressor made of (a) single pair of prisms followed by a roof mirror and (b) two pairs of prisms.

In an alternative configuration, prisms can be substituted by few centimetres of an hollow core fiber making the setup more compact. Indeed, one of the possible features

of HC fiber already mentioned in Chapter 1 is the opposite sign of the GDD in spectral regions where the normal fibers show a positive value. The blue curve in Figure 2.10 displays the behaviour of the dispersion of a HC-1060 fiber as function of the wavelength. As we can notice, the value for λ=1050 nm is positive differently from what would get for a normal fiber.

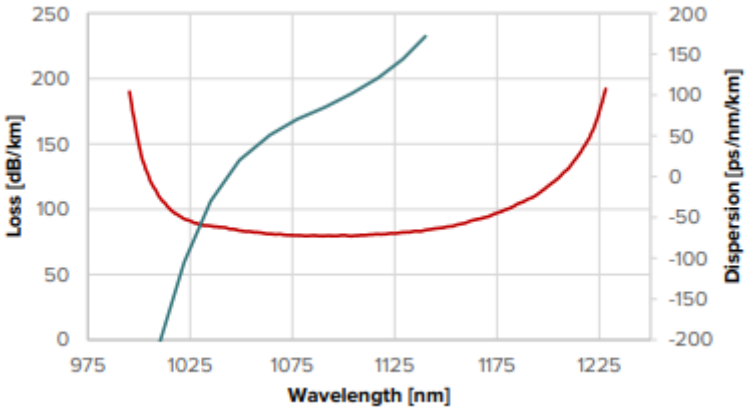

Figure 2.10: Typical dispersion (blue curve) and attenuation (red curve) from HC-1060 fiber datasheet.

The length needed for compensate dispersion can be easily estimated by comparing the phase accumulated during the propagation in a generic fiber φ_{f} with the one that would be accumulate in a HC fiber φ_{HC}:

$$\varphi_{\mathrm{f}} = -\frac{1}{2}\,\mathrm{GVD}_{\mathrm{f}}\,\mathrm{z}_{\mathrm{f}}\,\omega^2 \tag{2.24}$$

$$\varphi_{\mathrm{HC}} = -\frac{1}{2}\,\mathrm{GVD}_{\mathrm{HC}}\,\mathrm{z}_{\mathrm{HC}}\,\omega^2 \tag{2.25}$$

where z_{f} and z_{HC} are the length of the fibers. $\mathrm{GVD}_{\mathrm{f}}$ and $\mathrm{GVD}_{\mathrm{HC}}$ can be easily retrieved from the datasheets.

3 | Experimental results

3.1 Fiber amplifier characterization

3.1.1 Pump characterization

Before splicing all the fibers constituting the amplifier, we performed a characterization of the pump diode. The first quantity measured was the average output power as function of the pump current. The datasheet declares a maximum value of 70 W but, as already said, for our purposes 15 W are enough. As consequence, power measurements were performed up to that point. To do this, we used a power meter with a sensitivity of 10 mW and a range of 10 W that forced us to employ an attenuation filter for higher powers. The results are displayed in Figure 3.1.

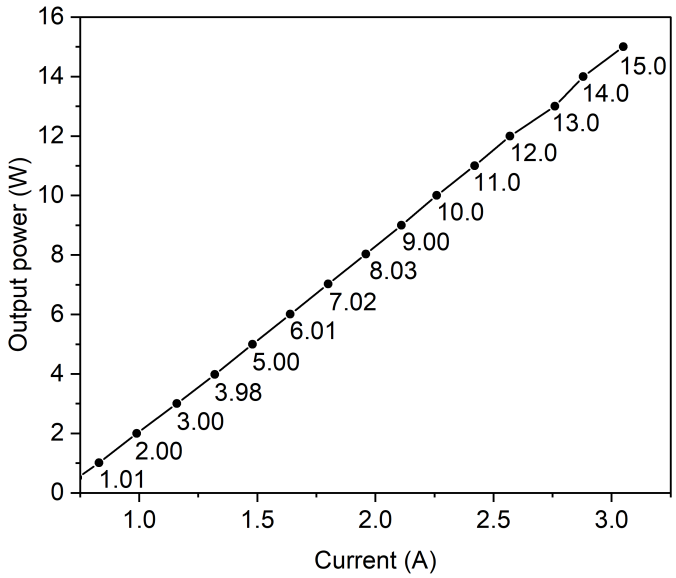

Figure 3.1: Current vs output average power of pump diode.

However, the real pump power is not the one shown in the figure since when the output fiber is spliced with the WDM, some losses are introduced. In order to quantify them we repeated the measurements after the WDM obtaining a value between 5% and 10% which can be considered satisfactory.

For what about the threshold current that is the level at which fiber amplifier starts to work and reaches a steady state condition, it was fixed at 0.85 A. The reason for this choice stays in the power measurements of the output pulses displayed in Subsection 3.1.2, where we noticed no amplification below that value. Furthermore, if we look at the fluorescence spectra shown in Fig. 3.2, the shape for lower levels of current is not smooth and clean like the one at 0.85 A. These measurements were performed after splicing the WDM with the 3-meter long Yb-doped fiber. One important aspect characterizing all the three spectra is the central wavelength that is not fixed, as we may expect, at 1030 nm. This shift is caused by the low precision characterizing the diode. However, this oscillator was the only solution available in laboratory and as consequence we must accept a small reduction in the efficiency of the system.
The same shift can be noticed in the output optical spectrum of the diode shown in Fig. 3.3 which, apart from that, has also a bad shape. These characteristics confirm what we just said. Nonetheless, the results obtained that will be shown later in the text can be considered satisfactory. Obviously, with a more expensive and precise diode we would have get a better performance.

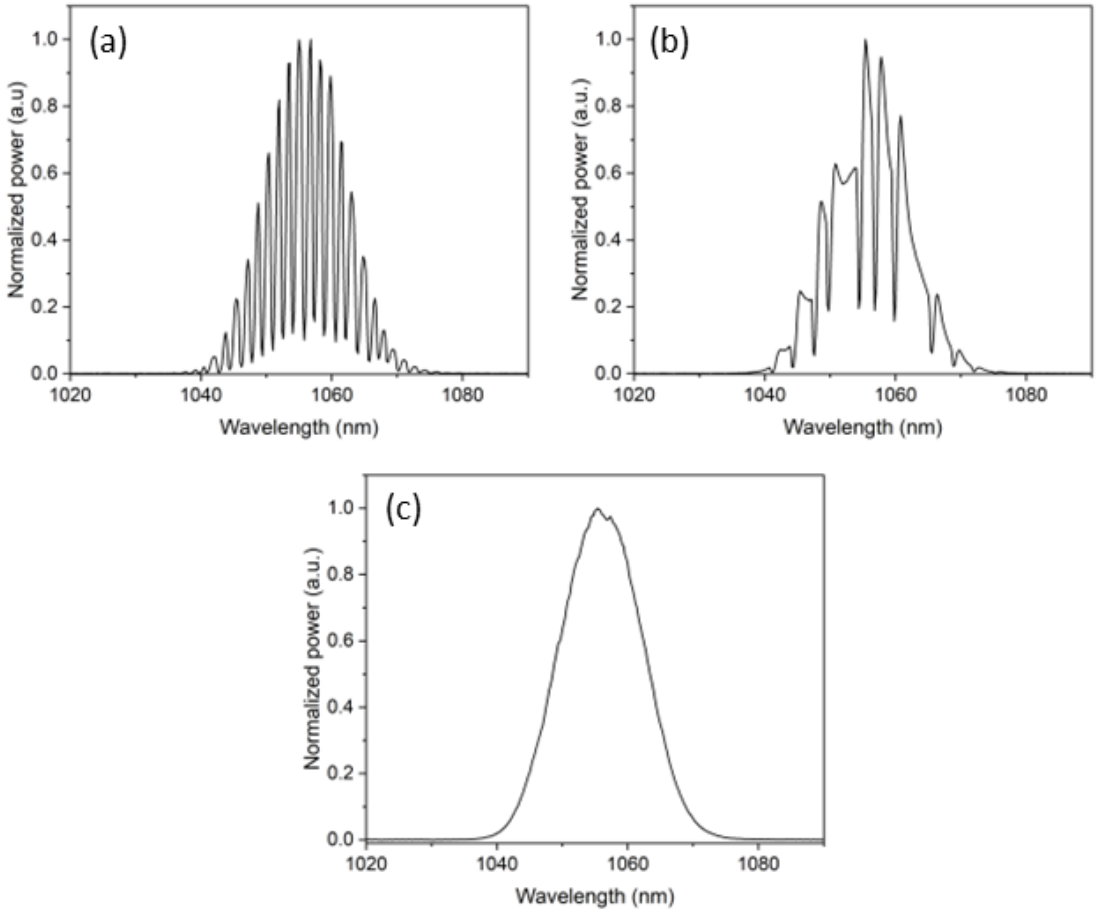

Figure 3.2: Fluorescence normalized optical spectra measured at a pump current of (a) 0.80 A, (b) 0.83 A and, (c) 0.85 A. The bad shapes of the spectra (a) and (b) are due to pump currents below the threshold.

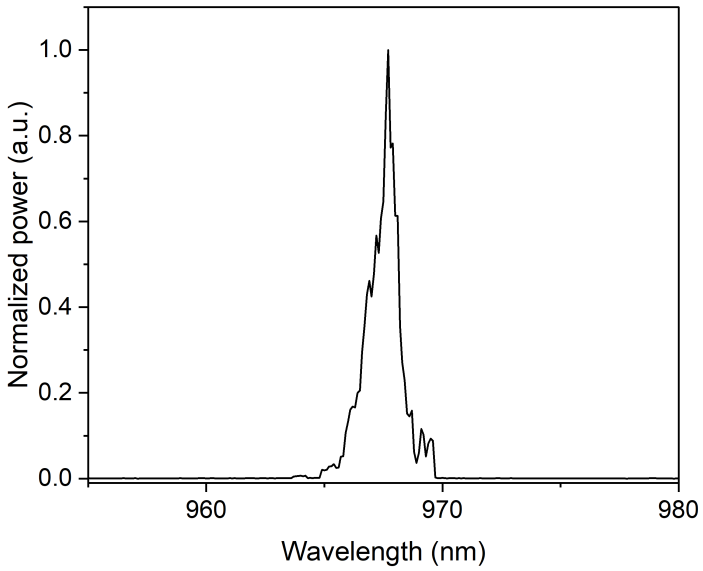

Figure 3.3: Normalized optical spectrum measured at the output of pump diode.

3.1.2 Output pulses characterization

After characterizing the pump, we proceeded by measuring the average power, the optical spectrum, and the intensity autocorrelation of the output pulses. Differently from previous measurements that were performed once at time, here the data were collected in parallel to speed up the process and to avoid any change in conditions. The setup adopted is shown in Figure 3.4.

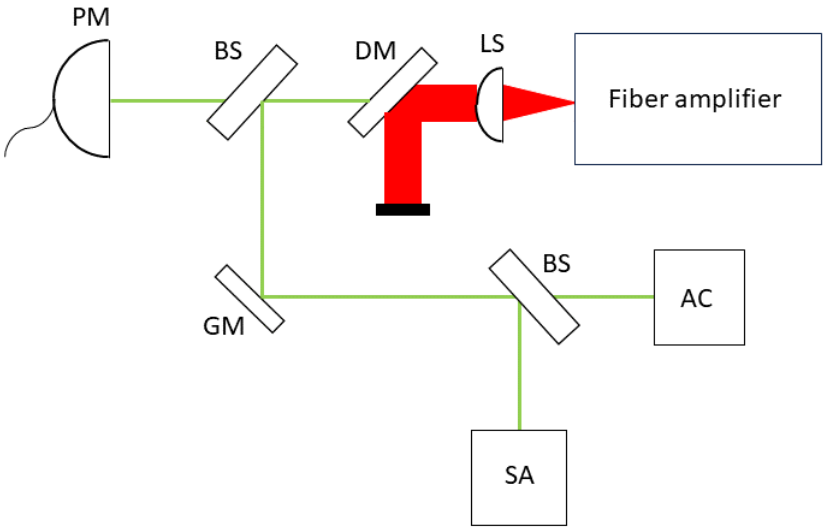

Figure 3.4: Measurements setup. AC: autocorrelator; BS: beamsplitter; DM: dichroic mirror; GM: gold mirror; LS: lens; PM: power meter; SA: spectrum analyzer.

We start analysing the average power. The measurements shown in Fig. 3.5 were performed with a power meter characterized by a sensitivity of 1 mW and by keeping fixed the pump current of Yb:CALGO to 0.65 A.

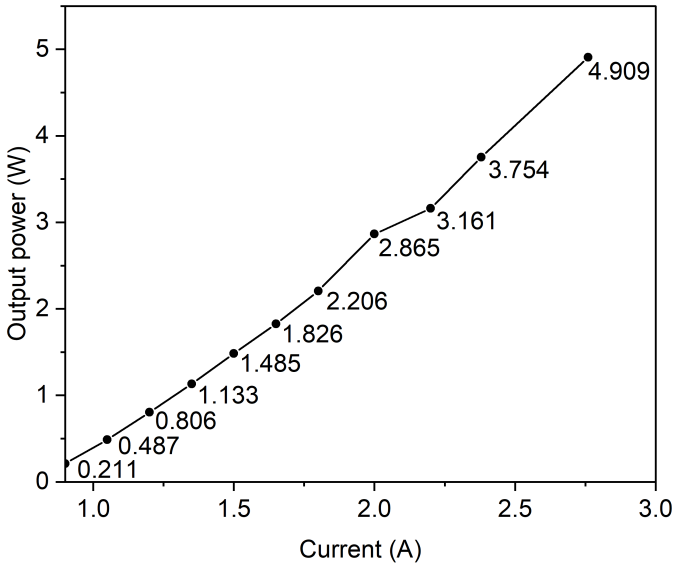

Figure 3.5: Pump current vs average power at the output of fiber amplifier.

By exploiting a pump power of 13 W we were able to get an average output power of 5W. Except for thermal and structural limitations of amplifier components, we would have achieved even higher values since as previously mentioned the pump diode can reach a maximum power of 70 W. However, we stopped there to avoid damaging the amplifier. Indeed, the parts in which the fibers are spliced are quite delicate and at high power the impurities within the waveguide could generate the so-called hot spots reducing the output values.

P_{out} **(W)**	$\Delta\tau_{AC}$ **(fs)**	Δt_p **(fs)**
0.160	3439	2233
1.000	3720	2416
2.000	3605	2341
3.000	3824	2483

Table 3.1: FWHM of intensity autocorrelation and corresponding pulse duration as a function of the average power at the output of the fiber amplifier.

The measurements of optical spectra shown in Fig. 3.6 were performed for four

different values of pump current (0.85 A, 1.35 A, 2.00 A, 2.76 A) with a sensitivity of 1 nm. As we can notice, all the four spectra are centred around 1050 nm as the ones of the input pulses. What changes between one measurement and the other is the full width at half maximum that increases by increasing the pump current. This spectral broadening seems to be caused by SPM confirmed also by the modulation on top of the curves characteristic of this effect.
The intensity autocorrelations were taken at the same level of power of the optical spectra. The measurements were performed at the highest resolution of the autocorrelator equal to 10 fs. As we can notice, the curves displayed in Fig. 3.7 are characterized by a very large FWHM compared to the one saw in Fig. 2.3. This is a consequence of the chromatic dispersion introduced during the propagation in the fiber amplifier. Another aspect that can be observed is that the trace in Fig. 3.7(a) is more noisy than the other three because near the threshold level, as already said, the fiber amplifier does not work well. The corresponding pulse durations are displayed in Table 3.1. As we can notice, all the values are higher than 2 ps and they do not change too much by increasing the pump current.

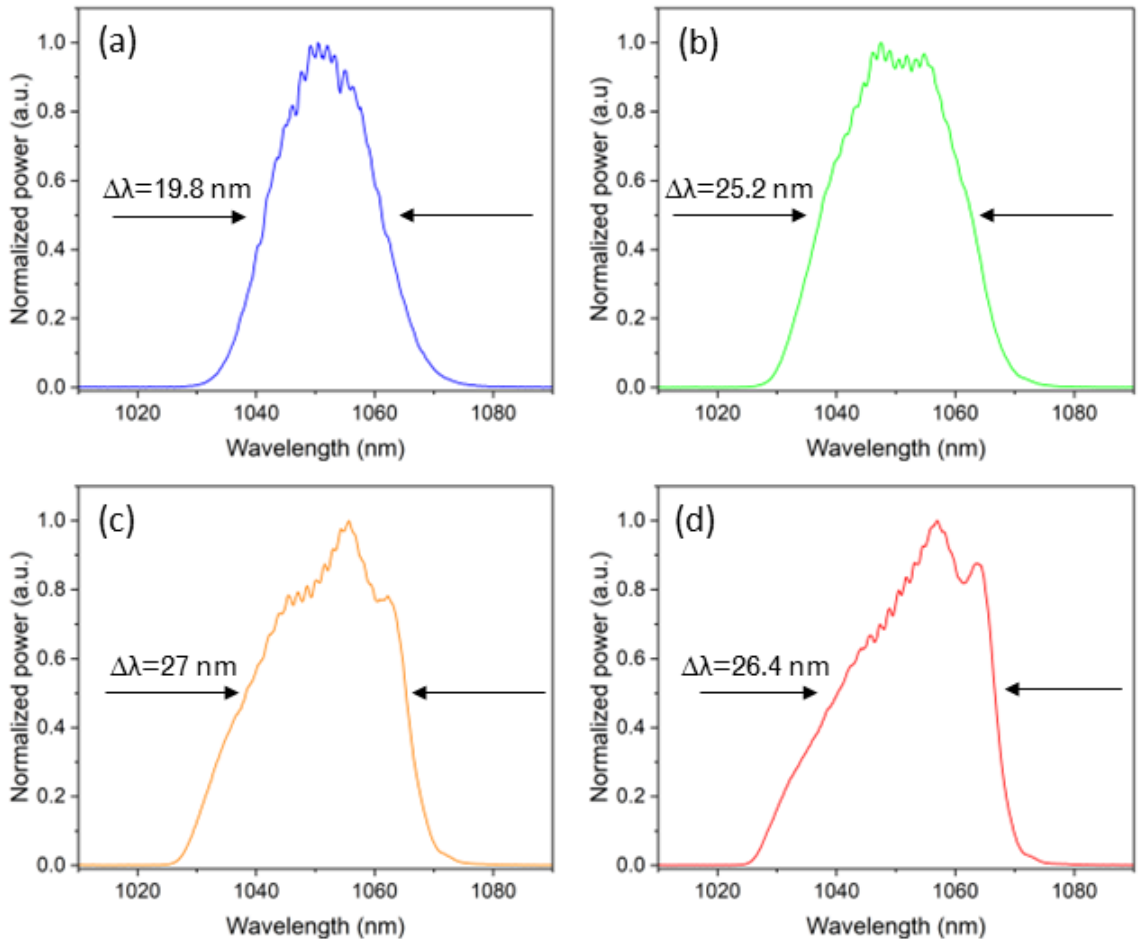

Figure 3.6: Normalized optical spectra measured at a pump current of (a) 0.85 A, (b) 1.30 A, (c) 2.00 A, and (d) 2.76 A.

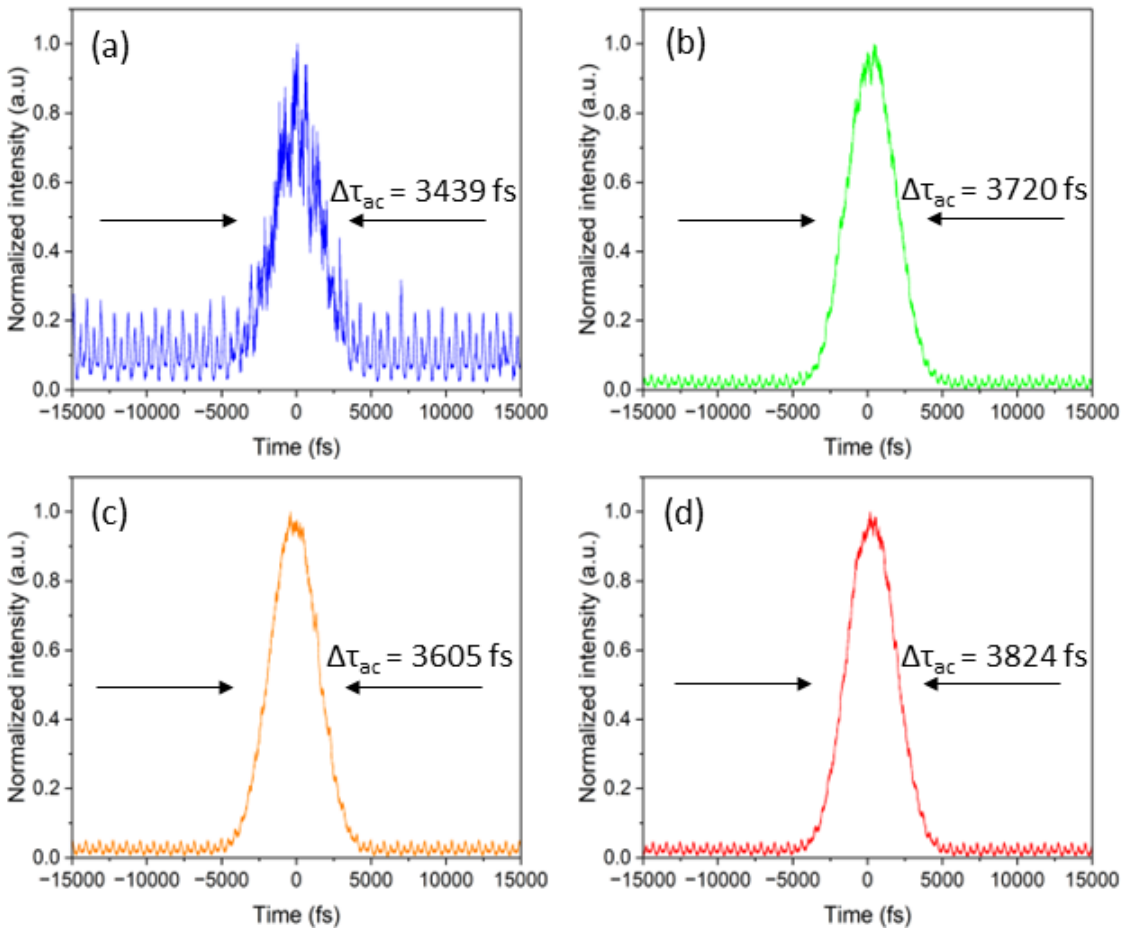

Figure 3.7: Normalized intensity autocorrelations measured at a pump current of (a) 0.85 A, (b) 1.30 A, (c) 2.00 A, and (d) 2.76 A.

3.1.3 Relative intensity noise after amplification

Figure 3.8 compares the RIN of the Yb:CALGO (already analysed in Subsection 2.2.4) with the ones of the amplified signals (AS). The latter were taken at three different levels of output power: one near the threshold of the amplifier (0.5 W), one at half the maximum output power reachable (2.5 W) and the last at the maximum power (5 W). As we can see, at low frequency the intensity noise of the amplified signal is higher than the one of the Yb:CALGO alone. Indeed, around 10^2 Hz there are all the electronic disturbances coming from the electric network whose frequency is 50 Hz. Since the fiber amplifier is made of electronic components such as the power supplier and the pump diode, it adds an extra noise in that region. This is confirmed by the RIN of the pump which is at the same level of the amplified signals. In Figure 3.8, the filtering effect performed by the Ytterbium upper level is more visible with respect to Figure 2.6. Indeed, at higher frequencies the RINs of amplified signals decrease reaching the level of Yb:CALGO while the intensity noise of the pump remains stable. At 30 kHz, we see the peak already analysed in Subsection 2.2.4 related to the mode-locking regime of the laser. One important aspect is the fact that by increasing the

pump current of the amplifier and so the output power, the RINs are not so much affected. Indeed, in Figure 3.8 the three amplified signals have almost the same level of intensity noise. At higher frequencies (>10^6 Hz) all the RINs, apart from the one of the pump, fall on the noise floor at -140dB/Hz.

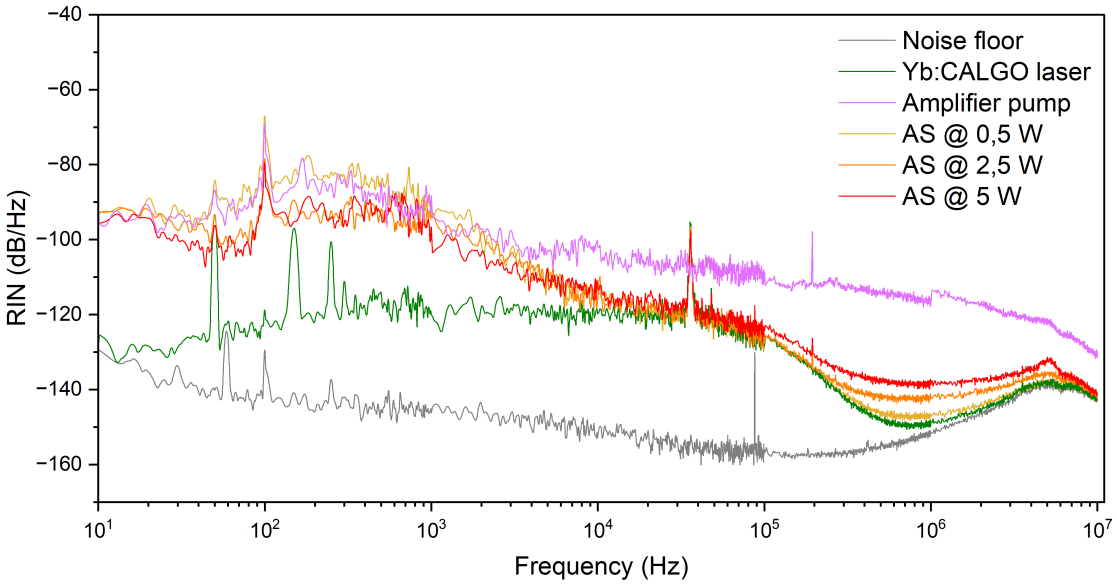

Figure 3.8: Relative intensity noise of Yb:CALGO and amplified signals (AS).

3.2 Pulse characterization after optical compression

This section will analyse two possible configurations we tested during the experiment. We start with the one we chose in which the compression stage is placed after the fiber amplifier. One characteristic to mention common to both the setups is that this stage introduces some losses whose value is between 20% and 25%. So all the values of average output power shown in Figure 3.5, at the same current, will be slightly lower after the compression. However, since our goal was to get already compressed pulses with and average power of 5 W, we increased a little bit the pump current arriving to 3.05 A. As consequence, the real value of average power reached after the amplifier, taken into account the losses, was 6 W. This last statement must be carefully managed since the data comes from an estimation and the maximum value measured after the amplifier is 5 W as shown in Figure 3.5.
The normalized optical spectra shown in Fig. 3.9 were measured at the same current values of the ones in Figure 3.6 with the same resolution. By comparing these spectra with the ones after the amplifier, we notice that compression does not affect too much them. Indeed, the spectra measured at 0.85 A and 1.35 A have practically the same shape of the equivalent traces in Fig 3.6. Instead, the other two curves are characterized by an asymmetric spectral broadening like ones after the amplifier, but with a

slightly different shape. For what about the FWHM, the values are almost the same with a maximum variation of 3 nm.

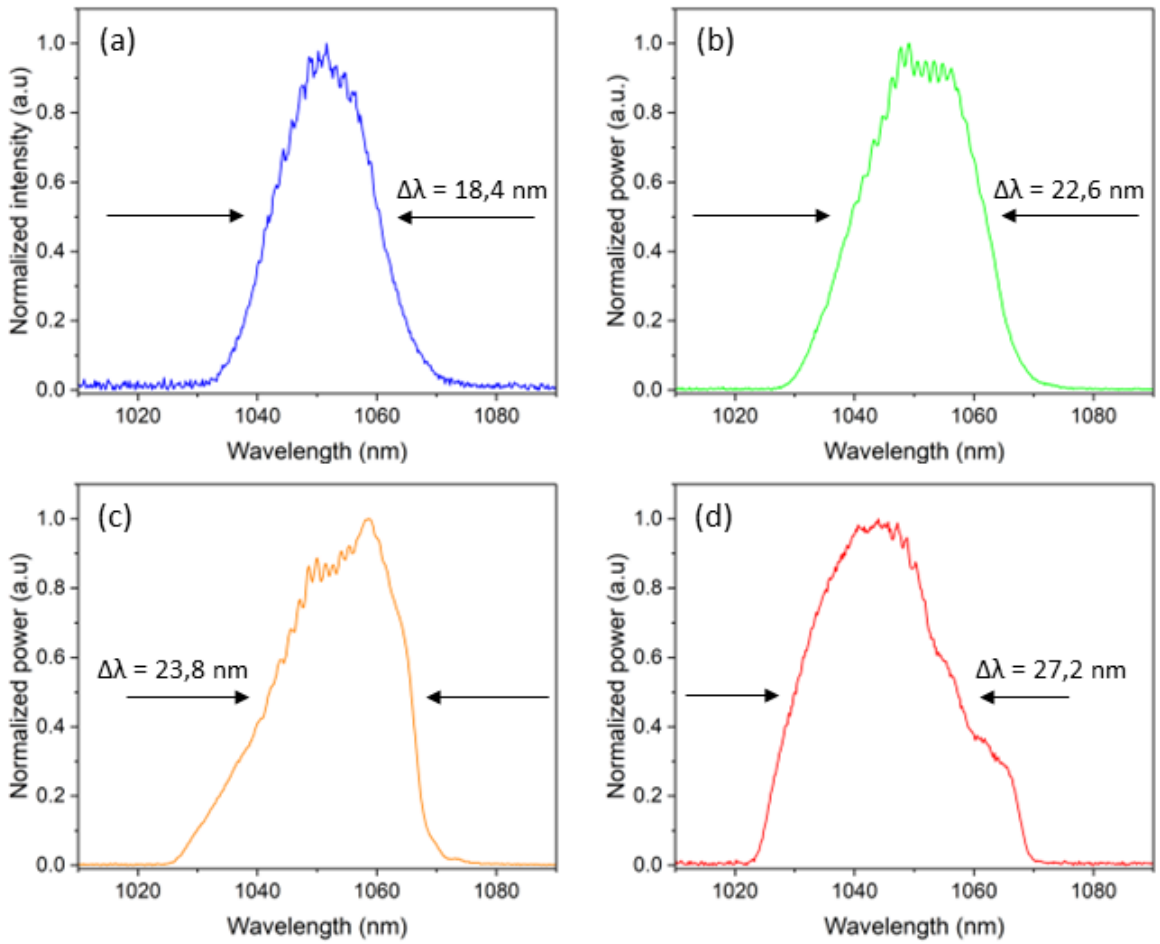

Figure 3.9: Normalized optical spectrum measured after optical compression at a pump current of (a) 0.85 A, (b) 1.30 A, (c) 2.00 A, and (d) 2.76 A.

We study now the pulse duration which is the characteristic mainly influenced by the optical compression. The distance between the two diffraction gratings is the quantity that must carefully determine in order to fully compensate the dispersion. The starting point was roughly determined by a mathematical simulation implementing a method similar to the one mentioned for HC fiber in Section 2.4. Indeed, for the calculation of the phase introduced by the active fiber, we used the Eq. (2.24). while for the gratings we applied the Eq. (2.21) to calculate the GDD and then the classical equation of the phase. The distance obtained is 18 mm. The fine tuning of this value was made by looking at the trace displays on the digital oscilloscope connected to the autocorrelator. The best distance is the one that produces the tightest intensity autocorrelation. In our case, for an average power of 5 W after the compression stage we obtained a distance of 15.41 mm. With this value, the normalized intensity autocorrelations shown in Fig. 3.10(b) is characterized by a FWHM of 130 fs corresponding to a pulse duration

of 81 fs. In Figure 3.10(a) is instead displayed the corresponding normalized optical spectrum. As we can see, around 1050 nm there are some spikes which indicate the presence of a lasing effect. Another characteristic that can be noticed is the highly asymmetric spectral broadening which extend mainly toward low frequency components. This could be a consequence of the intrapulse Raman scattering which is an effect characterizing the propagation of ultrashort pulses in fibers and whose details are described in Subsection 3.3.1. The effects of this phenomenon were already present in the spectra shown in Figure 3.9 but they were not so visible like in this spectrum.

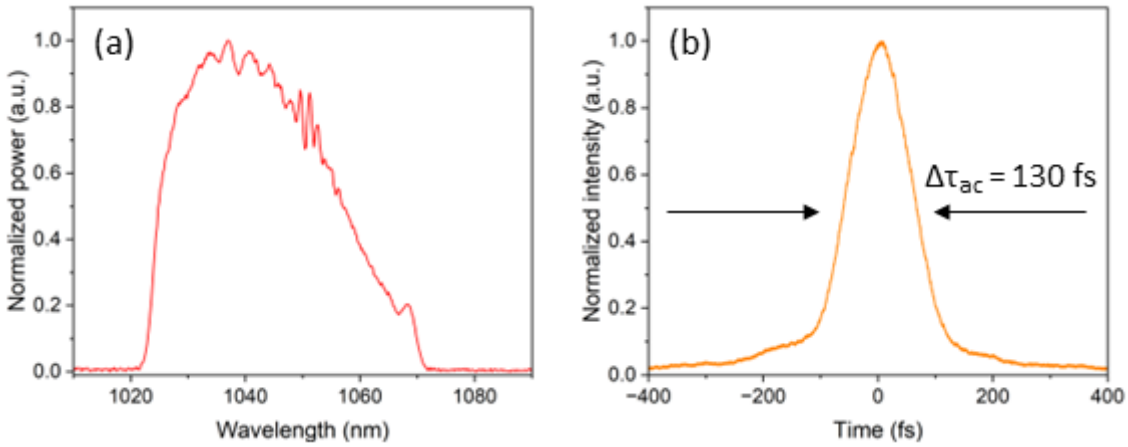

Figure 3.10: (a) Normalized optical spectrum for an average output power of 5W and (b) Normalized intensity autocorrelation for an average output power of 5W.

As said at the beginning of this subsection, this was not the unique possibility to compensate the dispersion. Indeed, before adopting the configuration described above, we placed the compression stage before the input of the fiber amplifier. In terms of average powers, this setup was in line with the other scheme. For what about the optical spectrum, the one measured here shown in Fig. 3.11(a) is quite asymmetric and characterized by a strange shape that does not allow us to quantify the FWHM. As consequence, even if we notice a spectral broadening, we cannot compare quantitively this curve with the ones in Figure 3.9. This spectrum was taken at a pump current of 1 A with the same resolution of the other measurements (1 nm).
However, what brought us to discard this setup is the measurement of intensity autocorrelation shown in Fig 3.11(b). Indeed, despite we used different distance between the diffraction grating, we were not able to reduce the pulse duration below 700 fs. The best intensity autocorrelation taken has a duration of 1.1 ps which is a value ten times larger than the one saw in Fig. 3.9. The reason why it was no possible to compress the pulses is not clear. Probably, it is connected to some distortions introduced by the compression stage in the optical spectrum causing an anomalous propagation of the components. However, this cannot be said with certainty since to verify we need the spectra after the compression.

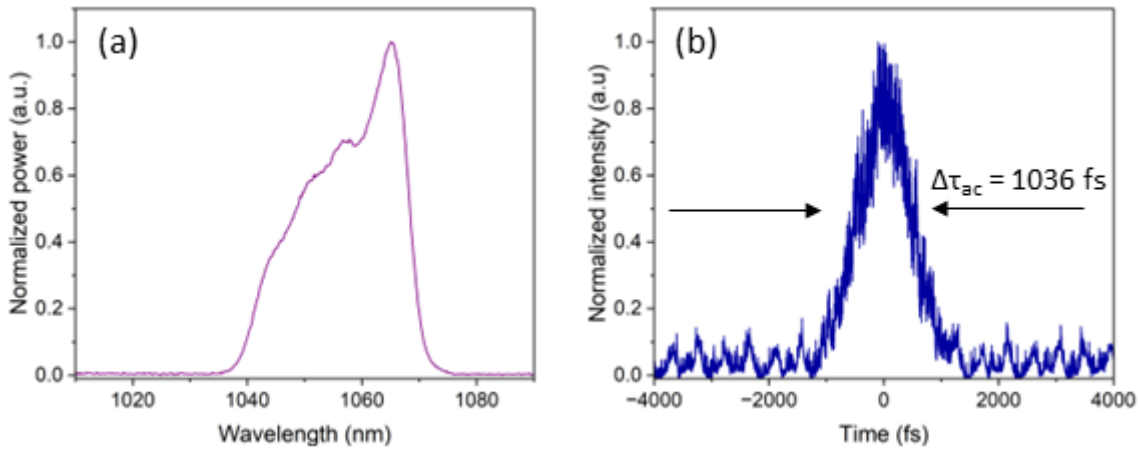

Figure 3.11: (a) Normalized optical spectrum and (b) normalized intensity autocorrelation. Both the measurements were performed after the optical compression stage placed before fiber amplifier.

3.3 Spectral broadening

3.3.1 Supercontinuum generation

Supercontinuum generation (SCG) or white light generation is a phenomenon causing a wide spectral broadening that exceed what is normally observed in case of self-phase modulation. This effect is generated by very intense pulses propagating in liquid, solid and gasses. Supercontinuum generation can be exploited for many applications in ultrafast science and technology such as spectrally resolved ultrafast spectroscopy and realization of octave-spanning spectra to stabilize femtosecond frequency combs [19]. Since we used PCF in our experiment to generate SC, in this chapter we will mainly focus on the physics of SC in fibers and on the comparison with bulk materials. In the latter the self-focusing effect plays a key role since, as already said, to obtain a wide spectral broadening, high powers are needed. Instead, in fibers this effect is not fundamental since the spatial mode is defined by the waveguide. Indeed, in the supercontinuum generation in PCF, the effects that play a principal role are the SPM and the dispersion. For what about the latter, bulk materials require condition of strong normal dispersion which instead is not fundamental for the waveguides. Another characteristic of SCG in fiber is that a very high power is not necessary since the nonlinear effects can accumulate over long propagation distances. These low intensities reduce the plasma generation through multiphoton ionization which is a phenomenon causing an opposite effect with respect the one of self-focusing. It is not clear if this effect limits or help the SCG to start, what is well-established is that it happens rarely in fibers. Photonic crystal fibers for SCG are of practical interest due to the low energy operation and due to a stable beam profile with high spatial coherence [19].
Mathematically, SCG cannot be described by simply the nonlinear Schrödinger equation saw in Chapter 1. Indeed, Eq. (1.45), apart from be valid in case of pulses with duration $>$ 1ps, does not consider some effects that influence the propagation of

ultrashort pulses (< 1ps) and that have a key role in supercontinuum generation. Among them we find higher-order nonlinearities up to the 9th-10th order, four-wave mixing, and intrapulse Raman scattering. In the latter, the low-frequency components are amplified by transferring energy from the high-frequency ones causing a shift of the optical spectrum toward the low-frequency side as the pulse propagates [50]. For this reason, it is sometimes referred to as self-frequency shift [59].
Now, we can take into account all these effects in the propagation equation. The starting point is represented by the wave equation (1.29). If we want to consider higher-order effects, the third-order nonlinear polarization must be expressed by:

$$\boldsymbol{P}^{(nl)}(\boldsymbol{r},t) = \varepsilon_0 \chi^{(3)} \boldsymbol{E}(\boldsymbol{r},t) \int_{-\infty}^{t} R(t-t_1)|\boldsymbol{E}(\boldsymbol{r},t_1)|^2 dt_1 \tag{3.1}$$

where $R(t-t_1)$ is the nonlinear response function that is different from zero for times $t_1 < t$ and zero for times $t_1 > t$ in order to ensure causality. This function describes the Raman response and it is defined as the sum of two components, one instantaneous and one retarded [60][61]:

$$R(t) = (1-f_R)\delta(t) + f_R h_R(t) \tag{3.2}$$

with f_R=0.18 in silica fibers while h_R(t) is the experimentally determined Raman cross section [60]. After following the same procedure described in Subsection 1.4.1, what we get is [62]:

$$\begin{aligned} \frac{\partial A}{\partial z} + \frac{\alpha}{2}A - \sum_{k\geq 2} \frac{i^{k+1}}{k!}\beta_k \frac{\partial^k A}{\partial t^k} =& i\gamma\left(1 + \frac{i}{\omega_0}\frac{\partial}{\partial t}\right)\cdot \\ & \cdot \left(A(z,t)\int_{-\infty}^{+\infty} R(t')|A(z,t-t')|^2 dt'\right) \end{aligned} \tag{3.3}$$

called generalized nonlinear Schrodinger equation. In Eq. (3.3) the right hand side that was not present in (1.42) takes into account, apart from the losses introduced by the intrapulse Raman scattering, the self-steepening and shock formation at pulse edge [63][64]. These are other higher-orders effects contributing to the supercontinuum generation. This equation is also valid in case in which the slowly-vary envelope approximation is no more effective and it can be used to describe the propagation of few optical cycles pulses if higher-order dispersive terms are considered [64][65].
In case of pulses with a duration in the order of picoseconds, $R(t)$ is replaced by the delta function δ(t) since the time scale is much longer than the one of Raman response function h_R(t). Furthermore, for such pulses the shock term and the higher-order dispersion terms are negligible [50]. By applying these conditions, we return to the Equation (1.42) treated in Chapter 1.
In the left of Fig. 3.12, we provide the result of a simulation implementing the Equation (3.3) that shows how the spectrum evolves as the pulse propagates. The fiber parameters are the same used by J.C.Travers, M.H. Frosz, and J.M. Dudley in Ref. [66]. Instead, the pulses have characteristics similar to the ones at our disposal. Indeed, we considered in the simulation an average power of 4 W with a duration of 80 fs. For

what about the length of the fiber, we chose 15 cm which is the same of the waveguide used in the experiment even if the model is different. Figure 3.12 shown also the temporal evolution plot from which it is possible to see the effects of the soliton fission [67][68] that become remarkable after a distance of 2 centimetres. This phenomenon belongs to the "higher-order nonlinear effects" named above and it causes a splitting of the higher-order solitons into multiple fundamental solitons. It dominates, together with Raman scattering and soliton formation, the pulse propagation at wavelengths longer than the zero-dispersion point in fibers. Conversely, at shorter wavelength pulse propagation is dominated by four-wave mixing and SPM.

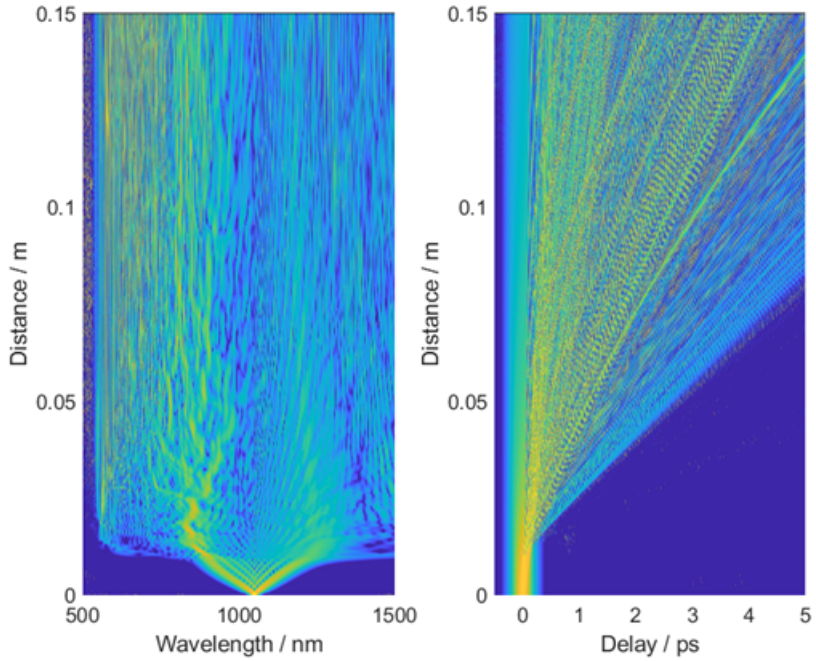

Figure 3.12: Example of spectrogram and temporal evolution plot in a photonic crystal fiber.

3.3.2 Experimental results

For the supercontinuum generation we adopted 15-cm long photonic crystal fiber (LMA-PM-10 by Thorlabs). The pulses at our disposal at the input of the fiber are characterized by a duration of 80 fs and an average power of 4 W. The last data seem not to be coherent with what we said in Section 3.2 where the power obtained was 5 W. If we return to the scheme in Section 2.1, there is an optical isolator between the fiber and the compression stage which introduces losses around 20% reducing the power to 4 W.
The light is coupled directly in the fiber by means of a lens. Choosing the right focal length is fundamental here since the coupling percentage depends from the dimension of the beam. To determine this parameter we used a simulation implementing the following formula:

$$w_1 = \frac{\lambda \cdot \mathrm{f}}{\pi \cdot w_0} \tag{3.4}$$

where w_1 and w_0 are respectively the output and the input beam radius while f is the focal length. In order to determine w_0 and other characteristic our beam we used a camera-based beam profile system. In Fig. 3.13 is shown the result of the measurement. The curve which represents the beam profile was fitted by means of a gaussian function obtaining w_0 ≈500 µm. Instead, for w_1 we considered half the mode field diameter provided in the datasheet of the photonic crystal fiber which is w_1=4.4 µm. By substituting these numbers in the Eq. (3.4), we get f=6.43 mm. The unique lens available with a focal length in the order of this number was an aspheric one with f=3.9 mm that allowed us to couple more than the 60% of the input power.

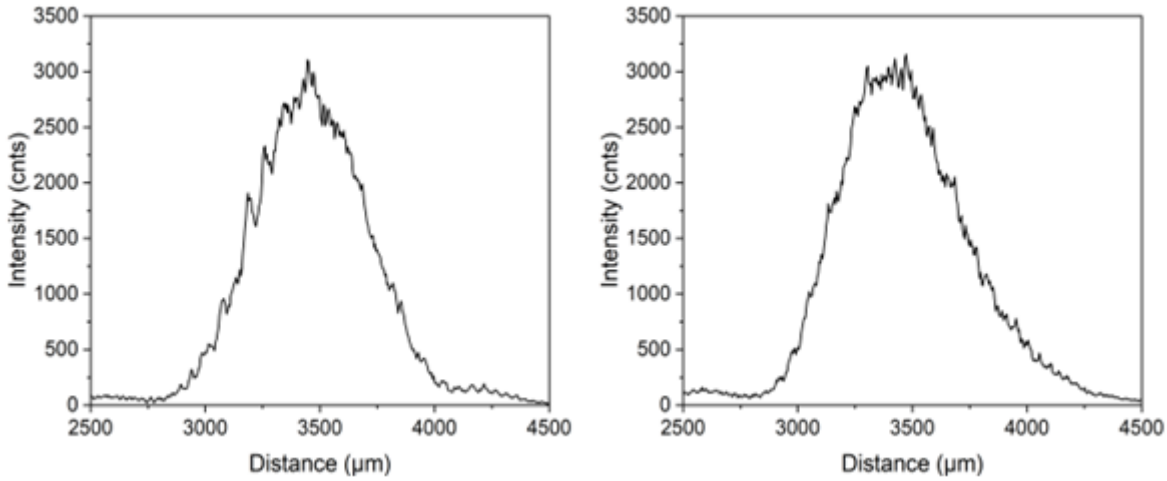

Figure 3.13: Beam profile measurements along X (on the left) and along Y (on the right).

In Figure 3.14, some measurements of optical spectrum performed after the PCF are shown. These are displayed in both linear (a) and logarithmic (b) scale. As expected, by increasing the power coupled in the fiber, the spectrum becomes wider and wider. In our case we have arrived to 1 W coupled which correspond to 2 W at the input of the fiber if we consider a coupling percentage of 60%. Already with these values we get a spectrum with a FWHM larger than 50 nm even if it is difficult to give a precise number due to the shape of the spectrum. As said in previous subchapter, we were able to reach a power of 4 W at the input of the fiber. If we consider that the measurements here were performed at half this value, we aspect to have at least 100 nm of FWHM with 4 W. The result could be further improved by increasing the coupling percentage using, for example, a lens with even lower focal length. In alternative, it is possible to save some centimetres of PCF which means reducing the costs of the system still obtaining good results. In Figure 3.14, it is possible to recognise the well-known modulation characteristics of the self-phase modulation. Indeed, especially in the curve corresponding to 1 W we see the two lateral peaks separated by a small modulation in the middle.

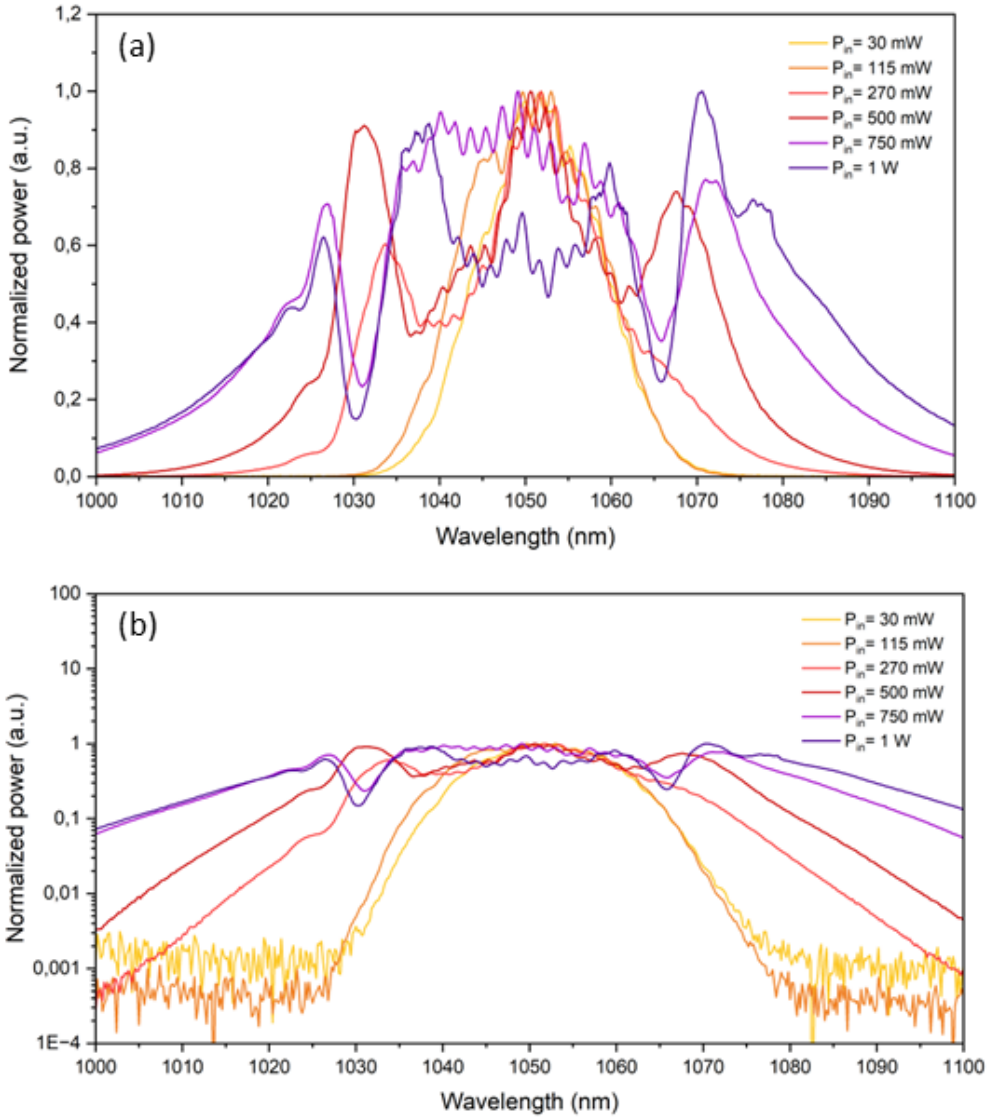

Figure 3.14: Spectral broadening for power going from 30 mW to 1 W in (a) linear scale and (b) logarithm scale.

The relative intensity noise was not measured because, as we will see in Section 3.4, the impossibility of implementing a suitable characterization technique does not allow a fine tuning of the optical compressors. As consequence, in absence of well-compressed pulses we preferred not to perform this measurement. However, we can make some predictions by means of a comparison with Fig. 3.8. What we expect is a degradation of the noise at low frequency caused by the modulation instabilities that govern the higher-order solitons propagation and fission. Also at high frequency there might be a degradation of white noise floor due to the nonlinear amplification of input pulse shot noise [69] even if it is expected to be not so dramatic due to the limited length of our fiber.

3.4 Pulse compression and characterization after supercontinuum generation

In this subchapter we will analyse some alternative characterization techniques to the one described in Chapter 2 and we will make some estimations about the temporal duration of our pulses after the compression. What we provide are estimations and not experimental data because the limited budget did not allow us to implement the scheme we are going to describe.
Our goal is to achieve a pulse duration of 15 fs that if compared with the 80 fs of the pulses before PCF, it produces a compressor factor F=80/15=5. We assume to be able to fully compensate the dispersion accumulated in PCF and so that the pulses we get are transform-limited. Under these conditions, the spectral broadening must be at least 5.3 larger than the initial spectrum which correspond to a FWHM of 80 nm. As shown in previous subchapter, already with half the maximum power we get a full width at half maximum of 50 nm and so we are confident to get a compression factor larger than 5.3 by fully exploiting the potential of the system. Indeed, assuming at maximum power a spectrum characterized by a FWHM of 100 nm, this would correspond to F=6.66 and so to pulses with duration of 12 fs.
By means of data provided in the datasheet of the PCF we can estimates both the distance between the fused silica prisms and the length of the HC fiber needed to compensate the dispersion. The calculations will stop for simplicity at the second order considering the GVD alone. The PCF has a group velocity dispersion at 1050 nm equal to 15 fs^2/mm that if multiplied by its length (15 cm), it produces a GDD of 2250 fs^2. Considering that HC-1060 fiber, already mentioned in Section 2.4, has a GVD at 1050 nm of about 14.6 fs^2/mm, the dispersion accumulated can be compensated with 15.4 cm of hollow core fiber. In alternative we can use a pair of SF14 prisms followed by a roof mirror (see scheme in Section 2.1). We estimate that with a tip-to-tip separation of about 12.6 cm we can fully compensate the dispersion.
In terms of average power at the output of the PCF, we estimate to have, at the best, more than 2.5 W. This value is enough high to allow a good efficiency in the production of a broadband mid-infrared pulse and for other applications treated in the next chapter.
Since we are dealing now with pulses with a duration lower than 20 fs, a characterization technique more sophisticated than the one shown in Subsection 2.2.3 is needed. This is represented by frequency-resolved optical gating, also known as FROG which belongs to the category of self-referencing spectrographic techniques. The latter use spectrograms to fully reconstruct pulses in terms of both amplitude and phase differently from noncollinear SH autocorrelator. Apart from that, this technique shows a high resolution allowing a characterization of pulses also in the sub femtosecond domain. There are many types of FROG which exploit different geometries and nonlinear interactions such as polarization gating, self-diffraction, and second- and third-harmonic generation [19]. Later we will provide a brief description of them.
Before we can analyse how to retrieve information about the pulse by means of FROG. We start defining three functions: $f(t)$ which is unknown, the gate function $g(t-\tau)$ which is known and, $f_{gated}(t,\tau) = f(t) \cdot g(t-\tau)$. The spectrogram $S(\omega,\tau)$ is defined

as the modulus squared of the Fourier transform of $f_{gated}(t,\tau)$:

$$S(\omega,\tau) = \left|\mathcal{F}\left\{f_{gated}(t,\tau)\right\}\right|^2 = \left|\int_{-\infty}^{+\infty} f(t)\cdot g(t-\tau)e^{-i\omega t}dt\right|^2 \tag{3.5}$$

The idea is to use an iterative procedure to retrieve the function $f(t)$ knowing $S(\omega,\tau)$ and $g(t-\tau)$. However, this is a general case. For ultrashort pulses the meaning of these functions is slightly different. Indeed, $f(t)$ represents the electric field $E(t)$ of the pulse while $g(t-\tau) = E(t-\tau)$ and for this reason is unknow. Instead, f_{gated} is here called E_{signal} and it is equal to:

$$E_{signal}(t,\tau) = E(t)\cdot E(t-\tau) \tag{3.6}$$

that can be defined as the electric field of a novel pulse generated inside a nonlinear media by the interaction of at least two replicas of E. As consequence the power spectral density measured by the spectrometer is equal to:

$$S(\omega,\tau) = \left|\mathcal{F}\left\{E_{signal}(t,\tau)\right\}\right|^2 \tag{3.7}$$

If now we feed all these quantities in the iterative procedure shown in Fig. 3.15 called vanilla procedure [70] after a certain number of iterations i, we can retrieve the unknown electric field. The equation in last box of Fig. 3.15 is obtained by inverting the integral of E_{signal} in $d\tau$:

$$\int_{-\infty}^{+\infty} E_{signal}(t,\tau)d\tau = \int_{-\infty}^{+\infty} E(t)\cdot E(t-\tau)d\tau = E(t)\int_{-\infty}^{+\infty} E(t-\tau)d\tau \tag{3.8}$$

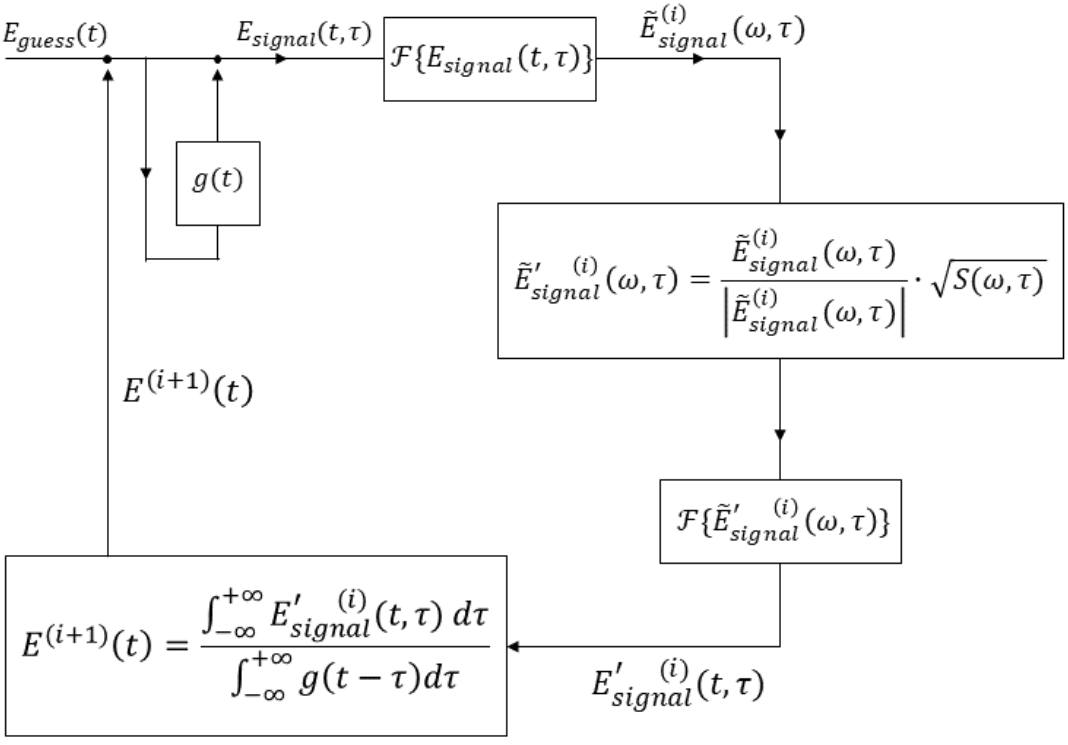

Figure 3.15: Vanilla procedure.

This is not the unique algorithm available since there exists more robust and complex procedure such as the so-called principal component generalized projection algorithm [70][71].
Among the most important types of FROG we find:

- *Second-harmonic generation* FROG (SHG-FROG) [72][73][70]. The scheme of this technique is identical to the one saw for the noncollinear SH autocorrelator shown in Figure 2.4 but with the photodetector substituted by a spectrometer. Here E_{signal} is defined as:

$$E_{signal}(t,\tau) = C \cdot E(t) \cdot E(t-\tau) \tag{3.9}$$

  where C is a constant. The advantages of this technique are the simplicity and the possibility to apply it also in continuous-wave laser. However, it is affected by time ambiguity in the sense that two pulses characterized by a chirp equal in modulus but different sign produce the same spectrograph being indistinguishable.

- *Polarization-gating* FROG (PG-FROG) [73][70]. This technique whose scheme is shown in Fig. 3.16 exploits the Kerr effect. The starting point is represented by the pulse to characterize and the delayed copy of it, called gating pulse. The former has a vertical polarization while the latter starts with a vertical polarization that is then converted into 45 degrees polarization.

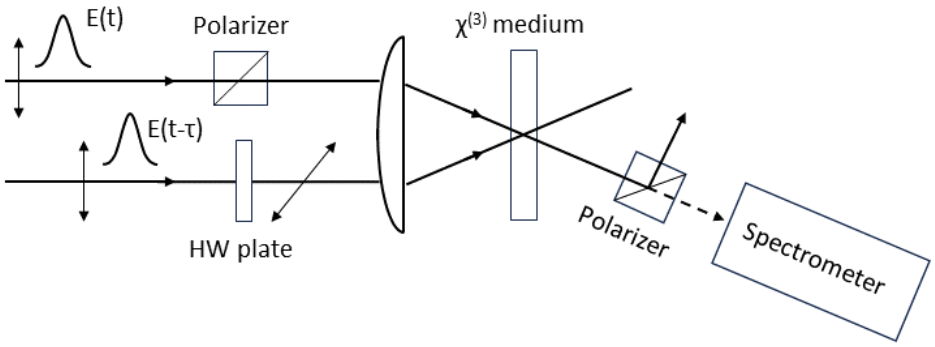

Figure 3.16: Polarization-gating FROG scheme.

The two pulses are then focus in a $\chi^{(3)}$ media where the phase modulation and the transient nonlinear birefringence caused by the Kerr effect produce a pulse with elliptical polarization that is partially transmitted by the second polarizer. The power spectrum of the transmitted pulse is then measured by a spectrometer. Here E_{signal} is equal to a quantity ΔE that represent the transmission function of the second polarizer and it is defined as:

$$\Delta E = C \cdot E(t) \cdot [n_{2//} - n_{2\perp}] \cdot |E(t-\tau)|^2 \tag{3.10}$$

where C is a constant while $n_{2//}$ and $n_{2\perp}$ are respectively the nonlinear index along the parallel and the orthogonal directions of the transient birefringence. This

technique solves the problem mentioned in SHG-FROG but the great amount of glass in the system introduces dispersion making it unsuitable for few optical cycles pulses.

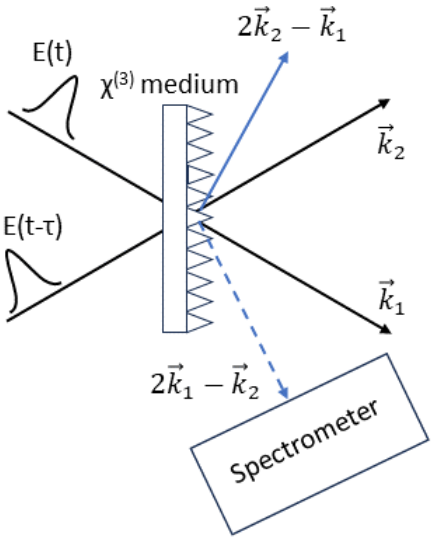

Figure 3.17: Self-diffraction FROG scheme.

- *Self-diffraction* FROG (SD-FROG) [74][73][70]. Like the previous technique, it exploits the interaction between the two pulses and the Kerr effect to produce a phase grating. These pulses, apart from creating it, are also diffracted by it. The possible diffraction directions are four as shown in Figure 3.17 and the power spectrum is measured by placing the spectrometer along one of the two external directions, $2\boldsymbol{k_2}$-$\boldsymbol{k_1}$ or $2\boldsymbol{k_1}$-$\boldsymbol{k_2}$. Consider the latter, E_{signal} is defined by:

$$E_{signal} = E(t) \cdot E(t) \cdot E^*(t - \tau) \tag{3.11}$$

  where the complex conjugate is due to the presence of a minus sign in front of $\boldsymbol{k_2}$.
  This technique is suitable for ultrashort pulses due to the small amount of glass. However, diffracted directions are, in general, not phase matched and so we need intense pulse to produce both a strong grating and a reasonable diffracted signal.

- *Third-harmonic generation* FROG (THG-FROG) [70][73]. This technique is similar to SHG-FROG but exploits the third-harmonic generation instead of the second-harmonic. As shown in Fig. 3.18, the possible directions are four, the external two are related to the third harmonic of the single pulses while the internal ones come from their interaction. The spectrometer is place along one of these last two directions. If we consider, for example, $2\boldsymbol{k_1}$+$\boldsymbol{k_2}$, what we get is:

$$E_{signal} = E(t) \cdot E(t) \cdot E(t - \tau) \tag{3.12}$$

  This technique is mainly exploited in the medium infrared since the third-harmonic of NIR is in the UV and it is difficult having a detector working in that spectral region.

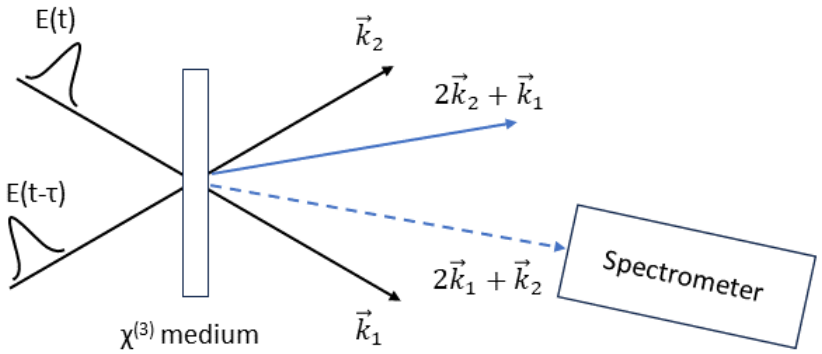

Figure 3.18: Third-harmonic generation FROG scheme.

In Fig. 3.19 are shown some examples of measurement provided by Trebino in Ref. [73]. Despite the problems characterizing it, for our purpose we would have decided to adopt the SHG-FROG due to its simplicity.

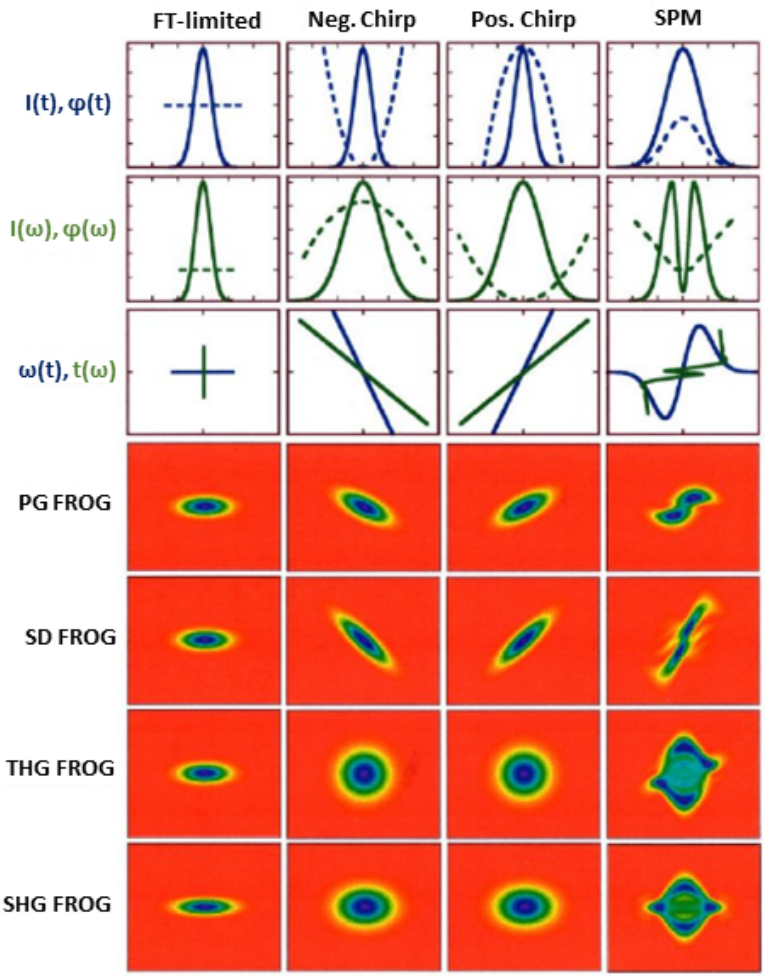

Figure 3.19: Comparison of traces for most common ultrashort pulses measured with different types of FROG provided by Trebino in Ref. [73].

4 | Few-optical-cycles pulse applications

4.1 Three-waves interaction processes

The frequency-conversion processes based on second-order nonlinear optic can be described as the interaction of three pulses/waves [19]. The latter must satisfy the energy conservation condition $\omega_1 + \omega_2 = \omega_3$ that in case of pulses represent the central angular frequency of the spectrum. To get a good efficiency also the phase matching or momentum conservation should be satisfied: $\boldsymbol{k_1} + \boldsymbol{k_2} = \boldsymbol{k_3}$.
The most common second order nonlinear effects are summarized in Fig. 4.1. Among them we find:

- *Sum frequency generation* (SFG) where the interaction of two waves of frequencies ω_1 and ω_2 generates a third wave of frequency $\omega_3 = \omega_2 + \omega_1$.
- *Difference frequency generation* (DFG) which involves again the interaction of the same two waves of SFG but generating a third wave of frequency $\omega_3 = \omega_2 - \omega_1$.
- *Second-harmonic generation* (SHG) which is a particular case of SFG where the two input waves have the same frequency.
- *Optical parametric amplification* (OPA) which is a particular case of DFG where in presence of strong input wave of frequency ω_2, the lower frequency wave ω_1 is amplified.
- *Optical rectification* (OR) which is a particular case of DFG where $\omega_3 \cong 0$.

The electric fields of the three pulses can be written as:

$$E_i(z,t) = \frac{1}{2}\Big[A_i(z,t)e^{i(\omega_i t - k_i z)} + cc\Big] \tag{4.1}$$

where i=1,2,3. Consider now the expression of the second-order nonlinear polarization in the form of Eq. (1.27):

$$\begin{aligned} P^{(2)}(z,t) = \frac{\varepsilon_0 \chi^{(2)}}{4}\Big[&A_1(z,t)e^{i(\omega_1 t - k_1 z)} + \\ &+ A_2(z,t)e^{i(\omega_2 t - k_2 z)} + A_3(z,t)e^{i(\omega_3 t - k_3 z)} + cc\Big]^2 \end{aligned} \tag{4.2}$$

Since this equation is made of many terms and the procedure is equal for all the three pulses, consider only the terms oscillating at $\omega_3 = \omega_2 - \omega_1$ corresponding to field E_1:

$$P^{(2)}_{\omega_1}(z,t) = \frac{\varepsilon_0 \chi^{(2)}}{2}\left[A_3 A_2^* e^{i[(\omega_3-\omega_2)t-(k_3-k_2)z]} + cc\right]^2 \tag{4.3}$$

By comparing this equation with the (1.35) and by substituting the result into (1.39), what we get is:

$$\frac{\partial A_1}{\partial z} + \frac{1}{v_g(\omega_1)}\frac{\partial A_1}{\partial t} = -id_1 A_3 A_2^* e^{-i\Delta k z} \tag{4.4}$$

with $\Delta k = k_3 - k_2 - k_1$ and $d_1 = \frac{\omega_1 \chi^{(2)}}{2n(\omega_1)c}$. Further, in Eq. (4.4) we neglect for simplicity the dispersion effects assuming $\beta_n = 0$.

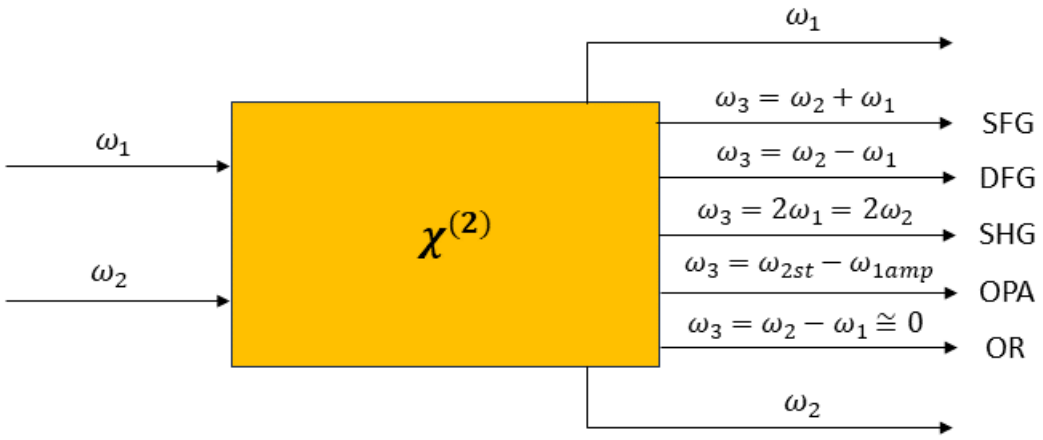

Figure 4.1: Summary scheme of the frequency-conversion nonlinear processes that can be described as interaction of three pulse/waves. SFG: sum frequency generation; DFG: difference frequency generation; SHG: second-harmonic generation; OPA: optical parametric amplification; OR: optical rectification;

Now, consider a new time frame comoving with the third pulse defined by $T = t - \frac{z}{v_g(\omega_3)}$. Since we are dealing with more than one pulse, by passing to this time frame we will have some shift of the other two due to the different propagation speeds. This aspect must be considered in the treatment of the various second-order nonlinear processes. After performing all the calculation also for the other two pulses, what we get is the following system of equations:

$$\begin{cases} \dfrac{\partial A_1}{\partial z} + \delta_{13}\dfrac{\partial A_1}{\partial T} = -id_1 A_3 A_2^* e^{-i\Delta k z} \\ \dfrac{\partial A_2}{\partial z} + \delta_{23}\dfrac{\partial A_2}{\partial T} = -id_2 A_3 A_1^* e^{-i\Delta k z} \\ \dfrac{\partial A_3}{\partial z} = -id_3 A_1 A_2 e^{+i\Delta k z} \end{cases} \tag{4.5}$$

where δ_{13} and δ_{23} are the group velocity mismatches expressed by:

$$\delta_{ij} = \left[\frac{1}{v_g(\omega_i)} - \frac{1}{v_g(\omega_j)}\right] \tag{4.6}$$

At the beginning of this section, we spoke about not only of interaction of pulses. Indeed, the system can be further simplified by considering waves satisfying the following relation:

$$\frac{\partial A_i}{\partial T} = 0 \tag{4.7}$$

where i=1,2,3. This condition tells us that the amplitudes of the three waves are constant over the time. As consequence, if we look at their temporal evolution at fixed point in $\chi^{(2)}$ media, the values will be always the same. Instead, if we look over the propagation along z, these will change due to the interaction among the three waves. The System (4.5) represents the starting point of the descriptions of second-order nonlinear processes treated in following subsection. A rigorous mathematical treatment is followed only for SHG, DFG and OPA. The reason why we do not consider SFG is because the procedure explained in Subsection 4.1.1 is practically identical to the one of second-harmonic generation with the difference that the two input waves have a different frequency. Apart from that, we decided to describe accurately only SHG since one of the applications faced in this chapter is based on it. Differently from SFG, optical rectification is presented since it is exploited in THz-radiation generation described in Section 4.3. However, we limit to provide few key concepts of the process without following a rigorous procedure due to its similarity to DFG.

4.1.1 Second harmonic generation

Second-harmonic generation is a second-order nonlinear process that produces a wave having twice the frequency of the input one. The mathematical treatment followed here is the same proposed by A. Weiner in Ref. [19]. It starts considering the case of a wave of intensity I_ω that, as shown by Fig. 4.2, can be split into two waves with the same frequencies $\omega = \omega_1 = \omega_2$ and with amplitudes defined by:

$$A_1 = A_2 = \frac{A_\omega}{\sqrt{2}} \tag{4.8}$$

Here, the factor $\sqrt{2}$ ensures the conservation of the intensity. The second-harmonic generated by the interaction is a wave of frequency 2ω and amplitude $A_{2\omega}$. By substituting all of these quantity in the System (4.5) and considering the approximation expressed by Eq. (4.7), what we get is:

$$\begin{cases} \dfrac{\partial A_\omega}{\partial z} = -id_\omega A_\omega^* A_{2\omega} e^{-i\Delta kz} \\ \dfrac{\partial A_{2\omega}}{\partial z} = -id_{2\omega}\dfrac{A_\omega^2}{2} e^{i\Delta kz} \end{cases} \tag{4.9}$$

with $\Delta k = k_{2\omega} - 2k_\omega$. This system is not difficult to solve analytically. Nonetheless, we prefer making a further approximation called non depletion approximation where

we consider an input wave so strong that the generation of the second harmonic does not reduce its intensity $[A_\omega(z) \sim A_{\omega_0}]$.

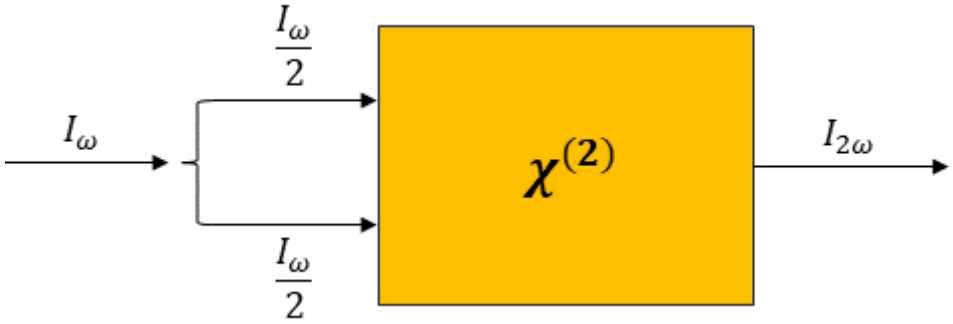

Figure 4.2: Simplified scheme describing the second-harmonic generation in a $\chi^{(2)}$ medium. Here the input wave is split into two waves having half its intensity.

Now, integrate the second equation of the system between 0 and z and impose $A_{2\omega}(0) = 0$, obtaining:

$$A_{2\omega}(z) = \frac{id_{2\omega}A_{2\omega}^2}{\Delta k} e^{i\frac{\Delta kz}{2}} sin\left(\frac{\Delta kz}{2}\right) \tag{4.10}$$

If we multiply and divide the Equation (4.10) by z/2 and we make the modulus squared of the result, we get the corresponding intensity expressed by:

$$I_{2\omega}(z) \propto d_{2\omega}^2 I_\omega^2 \frac{z^4}{4} sinc^2\left(\frac{\Delta kz}{2}\right) \tag{4.11}$$

we notice that the intensity of the second-harmonic wave is proportional to the square of I_ω and of the parameter d which contains $\chi^{(2)}$. Further, if we consider the case of a perfect phase matching $\Delta k = 0$, $I_{2\omega}$ is also proportional to the square of z showing a behaviour depicted in Fig. 4.3 as it propagates. However, this condition is not easy to achieve since:

$$\Delta k = k_{2\omega} - 2k_\omega = \frac{\omega}{c} n(2\omega) - 2\frac{\omega}{c} n(\omega) = 0 \tag{4.12}$$

requires $n(2\omega) = n(\omega)$. As shown in Fig. 4.4, this cannot be satisfied by simply employing an isotropic media. For this reason, it is necessary to adopt a birefringent medium. In the latter, it is possible to exploit the presence of an ordinary and extraordinary axis to fulfil the phase matching condition and so increase the efficiency of the process. In order to understand how it works, see Figure 4.5 where the co-called normal (or $\boldsymbol{k}$) surfaces are depicted. These curves refer to the case of positive uniaxial crystal where the refractive index along extraordinary axis n_e is larger than the one along ordinary axis n_0. The circle in black represents n_0 for a frequency $2\omega_0$ while the blue curve is expressed by [19]:

$$\frac{1}{n_b(\theta)} = \frac{cos^2\theta}{n_0} + \frac{sin^2\theta}{n_e} \tag{4.13}$$

In our case, the surface is calculated by using n_0 and n_e for a frequency ω_0. The parameter θ represents the incident angle of the input wave.

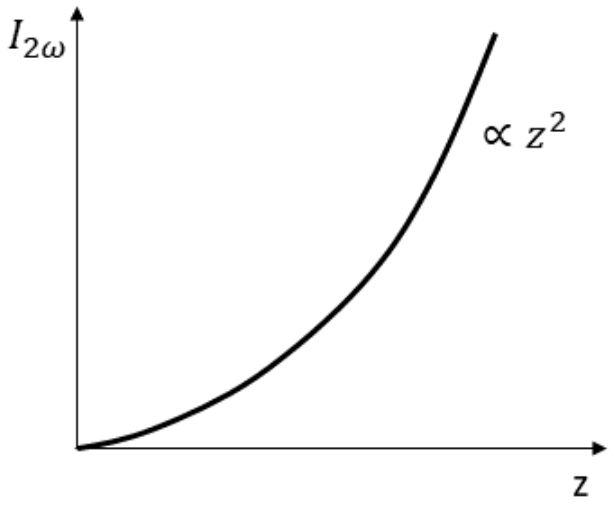

Figure 4.3: Behaviour of the second-harmonic intensity $I_{2\omega}$ as function of the length of the medium.

From the Figure 4.5, we see that the two curves have four cross points in which the values of the refractive indexes for ω_0 and $2\omega_0$ are the same. So, by properly choosing the angle θ_{pm} of the input wave, we can achieve the following condition:

$$n_b(\theta_{pm}, \omega_0) = n_a(2\omega_0) = n_0(2\omega_0) \tag{4.14}$$

obtaining a perfect phase matching. The price to pay is that the second-harmonic and the fundamental waves will be polarized along orthogonal directions but this is not the problem if we consider the advantages in terms of efficiency. This argument can be used to explain why the hypothesis of scalar $\chi^{(2)}$ was defined unphysical in Chapter 1. Indeed, if our two fields are $\boldsymbol{E_y} = \boldsymbol{E_\omega} = E_\omega \boldsymbol{u_y}$ and $\boldsymbol{E_x} = \boldsymbol{E_{2\omega}} = E_{2\omega}\boldsymbol{u_x}$, the second-order polarization vector is written as:

$$\boldsymbol{P_x} = \varepsilon_0 \chi^{(2)}_{xyy} \boldsymbol{E_y^2} \tag{4.15}$$

where the tensorial nature of $\chi^{(2)}$ is highlighted. The condition expressed in (4.14) belongs to type I phase matching which is the most exploited in SHG and where the second-harmonic is polarized along ordinary axis while the fundamental wave along the extraordinary axis. However, there exist other two types of phase matching conditions called type II and type 0 [19]. In the former the fundamental wave is split into two waves: one polarized along the ordinary axis the other along the extraordinary axis. The resulting second-harmonic wave will be polarized along ordinary direction. This type of phase matching can be realized in birefringent materials like the case of Type I.

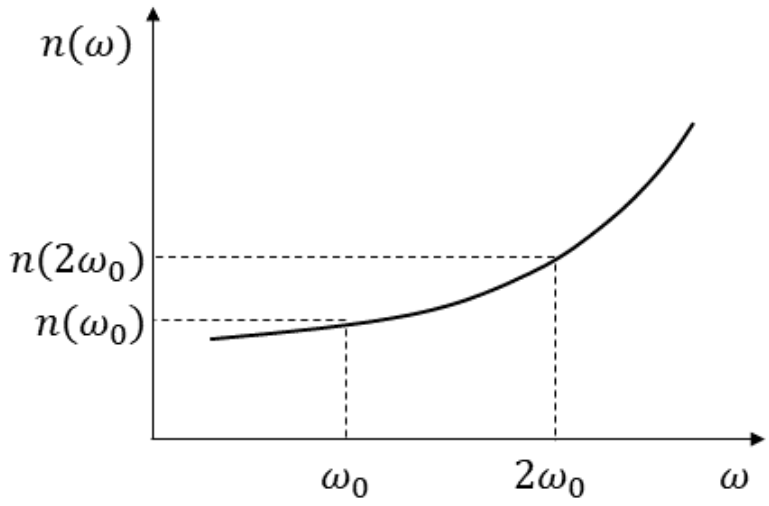

Figure 4.4: Behaviour of the refractive index n as function of ω in a general medium. As shown the values of n for ω_0 and $2\omega_0$ are different.

In type 0, all the three waves are polarized along the ordinary directions. However, differently from the other two types, it cannot be achieved in standard birefringent media. Indeed, in some nonlinear materials, it is possible to change the properties of polarization by applying strong fields with a certain periodic pattern. This process called periodic pooling generates alternating slices of material with $\chi^{(2)} > 0$ and $\chi^{(2)} < 0$ obtaining the effect depicted by the red curve in Figure 4.6. Each slice has a length equal to the coherence $L_{coh} = \Delta k/\pi$. The change of the sign of the second-order nonlinear susceptibility converts the destructive interference among the second-harmonic components into a constructive one. As consequence, the intensity instead of having an oscillatory behaviour characteristic of the non-phase matched processes described further in the text, it has the trend displayed by the red curve in Fig. 4.6. The condition achieved is called quasi-phase matching (QPM)[19][75] and it is exploited not only in SHG but also in the other nonlinear frequency-conversion processes [76]. An alternative way to the application of strong fields consists in fabricate materials with a well-defined patterns. An example is represented by the oriented-pattern media which belongs to the category of the so-called QPM material described in Section 4.2.
Returning to Eq. (4.11), there is also the opposite case where $\Delta k \neq 0$. The intensity instead of increasing with z shows some oscillations which are fast if Δk is large while are slow if Δk is small as shown in Figure 4.7. If we would like to exploit the maximum efficiency of this condition, the crystal must have a length equal to coherence length which indicates the points at which $I_{2\omega}$ shows a maximum.
Now we pass to the case of pulses which is a little bit more complicated. If we consider a single pulse at the input of $\chi^{(2)}$ media, each component within the bandwidth will generate a second-harmonic. However, not all these components will be effectively transformed. It is necessary introduce the concept of phase matching bandwidth $\Delta\omega_{pm}$ that defines the bandwidth within which we can achieve a good phase matching and the components are effectively transformed into second-harmonics.

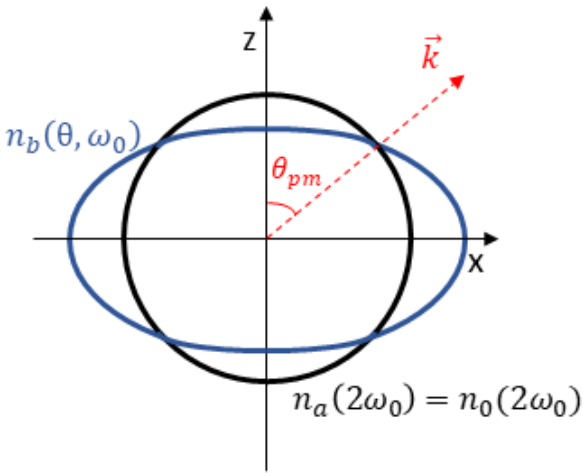

Figure 4.5: Normal or $\boldsymbol{k}$ surfaces for frequencies ω_0 (blue curve) and $2\omega_0$ (black curve). θ_{pm} is the angle for which phase matching condition is satisfied.

Consider a component $\omega = \omega_0 + \Delta\omega$ whose second-harmonic is $\omega_{SH} = 2\omega_0 + 2\Delta\omega$. If we impose $\Delta k_0 = k(2\omega_0) - 2k(\omega_0) = 0$, what we get is:

$$\Delta k = k(2\omega_0 + 2\Delta\omega) - k(\omega_0 + \Delta\omega) = 2\Delta\omega\delta_{2\omega_0,\omega_0} \tag{4.16}$$

with $\delta_{2\omega_0,\omega_0}$ group velocity mismatch defined by Eq. (4.6). As we can notice, it is not true that if the central components of the spectra are phase matched, the same holds for all the others. So, only those within $\Delta\omega_{pm}$ fulfil the condition. The phase matching bandwidth can be obtained by imposing:

$$\eta_{SH} \geq \frac{1}{2}\eta_{MAX,SGH} \tag{4.17}$$

where $\eta_{SH} = I_{2\omega}/I_{\omega}$ represents the efficiency of the second-harmonic generation. By making the calculations, what we obtain is:

$$\Delta\omega_{pm} = \frac{0,88 \cdot \pi}{L \cdot \delta_{2\omega_0,\omega_0}} \tag{4.18}$$

Here, L represents the length of the crystal. The fact that not all the bandwidth is transformed into a second-harmonic means that the pulse exiting from the medium will have a smaller BW and generally a longer duration.
In order to get the expression of the envelope of the second-harmonic pulse, we define a time frame comoving with pulse with central frequency ω_0 obtaining:

$$\frac{\partial A_{2\omega}(T,z)}{\partial z} + \delta_{2\omega_0,\omega_0}\frac{\partial A_{2\omega}(T,z)}{\partial T} = -id_{2\omega}\frac{A_{\omega}^2(T,z)}{2}e^{-i\Delta kz} \tag{4.19}$$

As we can notice, here $A_{2\omega}$ and A_{ω} depend on both T and z since condition 4.7 holds only for waves. If now we impose $T = \tau + \delta_{2\omega_0,\omega_0}z$ and we assume, for simplicity, that all components are phase matched, we get:

$$\frac{\partial A_{2\omega}(\tau,z)}{\partial z} = -id_{2\omega}\frac{A_{\omega}^2(\tau + \delta_{2\omega_0,\omega_0}z, z)}{2} \tag{4.20}$$

To further simplify the equation, assume that envelope of fundamental pulse depends only on time $A_\omega = A_{\omega_0} \cdot \delta(T)$ with A_{ω_0} constant. If now we impose $A_{2\omega}(\tau, z = 0) = 0$ and we integrate Eq. (4.20) between 0 and L, what we obtain is:

$$A_{2\omega}(\tau, L) = \frac{-id_{2\omega}A_{\omega_0}^2}{2} \frac{1}{\delta_{2\omega_0,\omega_0}} R(\tau) \tag{4.21}$$

Here, $R(\tau)$ is a function equal to 1 if $-L \cdot \delta_{2\omega_0,\omega_0} \leq \tau \leq 0$ and 0 everywhere else. If we go back to the local time frame, the only thing that change are these last conditions. Indeed, in that case R(T) is 1 if $0 \leq T \leq L \cdot \delta_{2\omega_0,\omega_0}$.

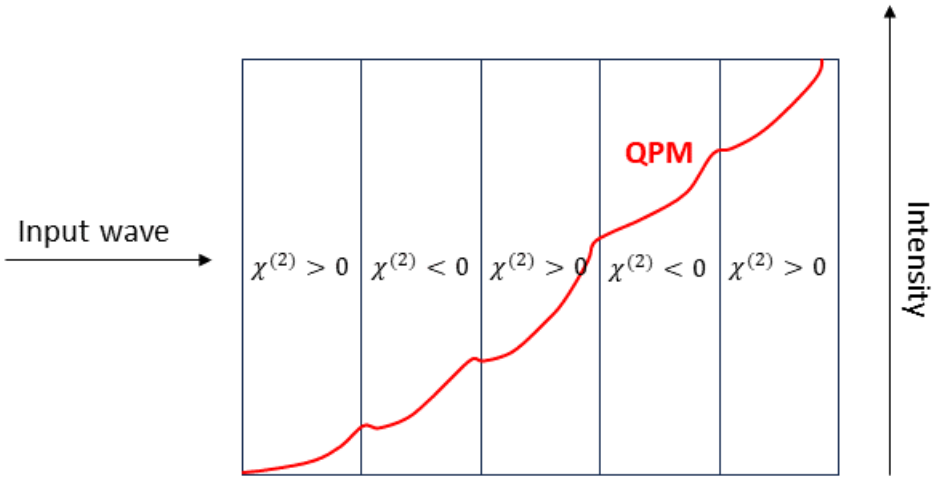

Figure 4.6: Periodic pooled medium. The red line describe the behaviour of the second-harmonic intensity in case of quasi-phase matching condition.

4.1.2 Difference frequency generation and optical parametric amplification

Difference frequency generation is a parametric process that starting from two input waves of frequencies ω_2 (also called signal) and ω_3 (called pump) produces a new wave of frequency $\omega_1 = \omega_3 - \omega_2$ (called idler). Further, in presence of a strong pump this process causes the amplification of the signal and for this reason it is also called optical parametric amplification.
The mathematical treatment is equivalent for both processes. As done for SHG, we follow the procedure proposed by A. Weiner in Ref. [19]. It starts from the case of perfect phase matching $\Delta k = 0$ and with the non-depletion approximation $[A_3(z) \sim A_{30}]$. As consequence, we recall only the first two equations of system which are related to the idler and the signal and under the previous assumptions they become:

$$\begin{cases} \dfrac{\partial A_1}{\partial z} = -id_1 A_2^* A_{30} \\ \dfrac{\partial A_2}{\partial z} = -id_2 A_1^* A_{30} \end{cases} \tag{4.22}$$

Now, differentiate the second equation and substitute $\frac{\partial A_1^*}{\partial z} = +id_1 A_2 A_{30}^*$ in it, obtaining:

$$\frac{\partial^2 A_2}{\partial z^2} = d_1 d_2 |A_{30}|^2 A_2 = \Gamma^2 A_2 \tag{4.23}$$

with $\Gamma = \left(d_1 d_2 |A_{30}|^2\right)^{\frac{1}{2}}$. The Equation 4.23 is well-known and its solution has the following form:

$$A_2(z) = c_1 e^{\Gamma z} + c_2^{-\Gamma z} \tag{4.24}$$

If we differentiate it and we impose $A_1(z=0) = 0$ and $A_2(z=0) = A_{20}$, it produces:

$$A_2(z) = A_{20} cosh(\Gamma z) \tag{4.25}$$

which describes the evolution of the signal while it propagates in the medium. In case of a large gain condition, we can assume $\Gamma z \gg 1$ and approximate $cosh(\Gamma z) \sim e^{\Gamma z}/2$. Under these assumptions, the intensity is expressed by:

$$I_2(z) = I_{20} \frac{e^{\Gamma z}}{4} \tag{4.26}$$

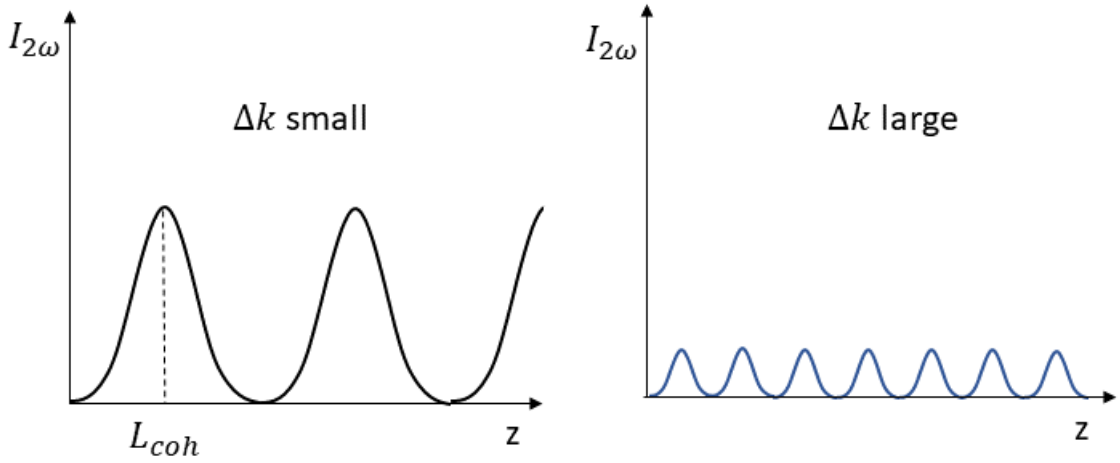

Figure 4.7: Behaviour of the second-harmonic intensity as a function of the length of the medium in case of small (on the left) and large (on the right) phase mismatch.

The Eq. (4.26) allows us to introduce the parametric gain of the system G which gives indication about the amplification of the signal. If we consider a media of length L, it is expressed by:

$$G = \frac{I_2(z)}{I_2(0)} = \frac{e^{\Gamma z}}{4} \tag{4.27}$$

Now, we can retrieve the intensity of the idler by integrating the first equation of the System (4.22) between 0 and z and by imposing the boundary conditions previously mentioned:

$$I_1(z) = \frac{1}{2} c\varepsilon_0 n(\omega_1)\frac{d_1}{d_2}|A_{20}|^2 sinh^2(\Gamma z) = I_{20}\frac{\omega_1}{\omega_2} sinh^2(\Gamma z) \tag{4.28}$$

As we can notice, Eq. (4.28) is linked to the intensity of the signal at z=0. If we write the Eq. (4.28) and (4.26) in terms of photon fluxes $n_i = I_i/\hbar\omega_i$ with i=1,2, we can retrieve an important characteristic of the process. Indeed, by calculating the difference between n_2 and n_1, we obtain n_{20} which is the the number of photons at the beginning of the crystal. This result tells us that the difference between signal and idler photons at the output of the crystal is always equal to the number of signal photons at the input. In case of $n_{20} = 1$, we get $n_2 = 2$ and $n_1 = 1$ which means that for each pump photon we destroy, we produce two new photons: one for the idler and one for the signal. This last statement described intuitively the amplification characterizing OPA. A pictorial view of what we just said is shown in Fig. 4.8.

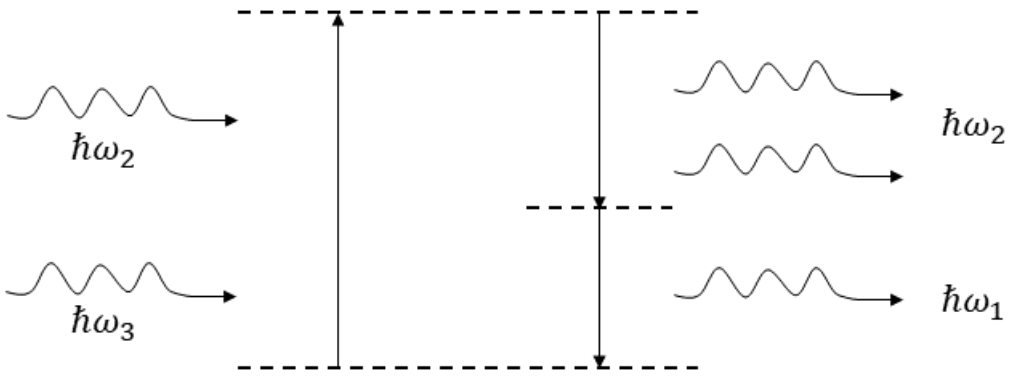

Figure 4.8: Pictorial view of optical parametric amplification. As shown for each pump photon of energy $\hbar\omega_3$, it generates two photons of energies $\hbar\omega_2$ and $\hbar\omega_1$.

If now we consider $\Delta k \neq 0$ and we make the same procedure adopted with perfect phase matching, the Eq. (4.23) becomes:

$$\frac{\partial^2 A_2}{\partial z^2} + i\Delta k\frac{\partial A_2}{\partial z} - \Gamma^2 A_2 = 0 \tag{4.29}$$

If we assume that the solution is $A_2(z) = A_{20}e^{gz}$ and we impose the same boundary conditions saw for $\Delta k = 0$, what we get is:

$$I_2(z) = I_{20}\left[cosh^2(\gamma z) + \frac{\Delta^2}{4\gamma^2} sinh^2(\gamma z)\right] \tag{4.30}$$

with $\gamma = \left[\Gamma^2 - \frac{\Delta k^2}{4}\right]^{\frac{1}{2}}$. Further, in 4.30 we assume $\Gamma^2 \gg \frac{\Delta k^2}{4}$. The resulting parametric gain is expressed by:

$$G = 1 + \frac{\Gamma^2}{\gamma^2} sinh^2(\gamma z) \tag{4.31}$$

From this equation we can determine the maximum phase mismatch Δk_m for which G is still good. There is not a unique criterion to retrieve this quantity, in our case we choose the following one:

$$G(\Delta k_m) = \frac{1}{2} G(\Delta k = 0) \tag{4.32}$$

Under the hypothesis of large gain, already seen in perfect phase matching, and by imposing $\gamma^2 \cong \Gamma^2$, we obtain:

$$\Delta k_m = 2\left[\frac{ln(2)\cdot\Gamma}{z}\right]^{\frac{1}{2}} \tag{4.33}$$

The Eq. (4.33) displays the relationship between Δk and the length of the medium and as we can notice, the latter is a limiting factor since higher is z, lower is the value of Δk for which we still have a good gain.
We can pass now to the case of ultrashort pulses where the generation process is based on the interaction among the components within the BW. Differently from what we did with second-harmonic generation, we do not repeat the rigorous mathematical treatment due to its complexity. We limit to analyse the BW within which we have an effective process. Assume to have three pulses perfectly phase matched with the following central wavelengths: ω_3, ω_{20} and, ω_{10}. If these last two frequencies are shifted of quantity $\Delta\omega$ such that $\omega_1 = \omega_{10} - \Delta\omega$ and $\omega_2 = \omega_{20} + \Delta\omega$, Δk becomes:

$$\Delta k = k_3 - \left[k_{20} + \frac{\partial k}{\partial \omega}\Delta\omega\right] - \left[k_{10} - \frac{\partial k}{\partial \omega}\Delta\omega\right] = \delta_{12}\Delta\omega \tag{4.34}$$

If now we substitute Δk in (4.34) with Δk_m expressed by (4.33) and we multiply by 2 in order to consider the full bandwidth, we get:

$$\Delta\omega_{FWHM} = 2\Delta\omega = \frac{4}{\delta_{12}}\left[\frac{ln(2)\cdot\Gamma}{z}\right] \tag{4.35}$$

Like in SHG, the limiting factors are both the group velocity mismatch and the length of the crystal.

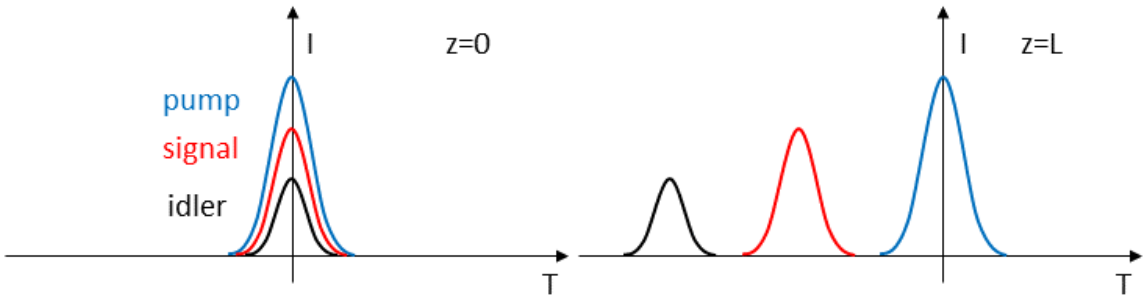

Figure 4.9: Pulses behaviour when the group velocities of signal and idler are faster than the pump. The absence of overlap does not allow an effective process.

The effect of a group velocity mismatch can be described qualitatively by considering the following three cases:

- Idler and signal are faster than pump which means that the group velocity mismatches δ_{13} and δ_{23} are both positive.
- Idler and signal are slower than the pump which means that δ_{13} and δ_{23} are both negative.
- Signal is faster than the pump while idler is slower than the pump. As consequence, δ_{13} is negative and δ_{23} is positive.

First two cases are equivalent. Figure 4.9 describes the behaviour of the three pulses when idler and signal are slower than the pump. This shows how the different group velocities do not allow an effective overlap among them. Under this condition, the difference frequency generation and the optical parametric amplification are not efficient. To be precise, the real behaviour of the pulses is more complicated and it is shown in Figure 4.10 where as we can notice there is a temporal broadening. This can be explained by considering that, even if the group velocity mismatch is large, there is a very weak overlap which causes an amplification process. The latter happens continuously even when the pulse moves away producing the effect described in figure.

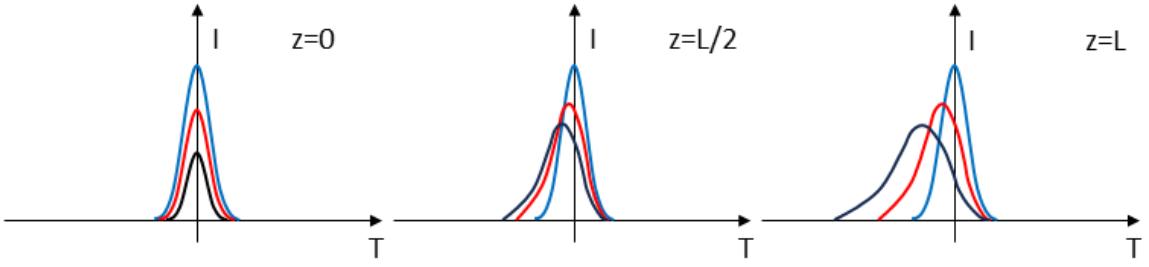

Figure 4.10: Real pulses behaviour in case of idler and signal faster than the pump. The amplification process happens continuosly causing a temporal broadening.

Instead, in third case, the three pulses are overlapped as shown in Fig. 4.11 and this produces an effective process. We assist to a reshape of the pump caused by the amplification of the signal. Further, if the mismatch is not large, signal and idler remain within the pump pulse limiting the temporal durations.
A way to improve the bandwidth expressed by Eq. (4.35) is to consider the degenerate case in which $\omega_2 = \omega_1$ and so $v_g(\omega_1) = v_g(\omega_2)$. However, with $\delta_{12} = 0$ the Equation (4.35) diverges. This is not true if the development in Eq. (4.34) is not stopped at the first order but arrive at least to the second one. In this way the equation becomes:

$$\Delta k = \frac{1}{2}\left[\beta_2(\omega_{10}) + \beta_2(\omega_{20})\right]\Delta\omega^2 \tag{4.36}$$

By proceeding like we did before, the phase matching BW is:

$$\Delta\omega_{FWHM} = 4\left[\frac{ln(2)\Gamma}{z}\right]^{\frac{1}{4}} \frac{1}{\left[|\beta_2(\omega_{10}) + \beta_2(\omega_{20}|\right]^{\frac{1}{2}}} \tag{4.37}$$

From the equation, we can notice that the improvements in phase matching bandwidth are possible only in case of small GVD.

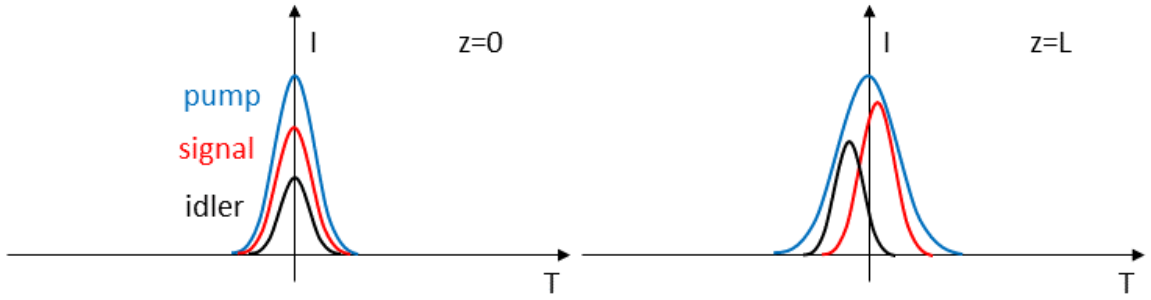

Figure 4.11: Pulses behaviour in case of idler slower than then pump and signal faster than the pump. The overlap causes a reshape of the pump and an effective amplification of the signal.

Up to this point we always consider a collinear case. Now we make a brief description of the non collinear geometry focusing on interesting phase matching condition. Assume to have three pulses with the same frequencies mentioned above but now with different propagation directions as shown in Figure 4.12. In this case the phase matching must be expressed along x and z. The equations describing it are:

$$\begin{cases} \Delta k_z = k_3 cos\alpha - k_2 - k_1 cos\Omega \\ \Delta k_x = k_3 sin\alpha - k_1 sin\Omega \end{cases} \tag{4.38}$$

Now we assume that both Δk_z and Δk_x are equal to zero and the three frequencies are shifted by $\Delta\omega$ like in collinear case. By following the same procedure described above, we arrive to the condition of phase matching expressed by:

$$v_g(\omega_2) - v_g(\omega_1)cos\Omega = 0 \tag{4.39}$$

The Equation (4.39) tells us that phase matching condition is reached if the projection of $v_g(\omega_1)$ on z is equal to $v_g(\omega_2)$.

4.1.3 Optical rectification

Optical rectification (OR) is second-order a nonlinear process that generates a DC or a low frequency polarization component [77] when a laser beam propagates in a medium. It is sometimes referred to as low difference frequency generation since OR

can be seen as a particular case of DFG where the frequency of the idler is around zero.
Here the mathematical treatment differs with the respect to the previous nonlinear processes. We start recalling the second order nonlinear polarization:

$$P^{(2)}(t) = \varepsilon_0 \chi^{(2)} E(t)^2 \tag{4.40}$$

To make calculations simpler, in Eq. (4.40) we explicit only the time dependence of the polarization. Consider a field propagating within the medium whose expression is made of the sum of two components with the same amplitude E_0 and different frequencies:

$$E(t) = E_0 cos(\omega_1 t) + E_0 cos(\omega_2 t) \tag{4.41}$$

In order to be coherent with Eq. (4.40), here we neglect the space dependence of the electric fields. By substituting (4.41) into (4.40), we get a second-order nonlinear polarization constituted by the following terms:

$$\begin{aligned} P^{(2)}(t) = \varepsilon_0 \chi^{(2)} \frac{E_0^2}{2} \big\{ & 2 + cos(2\omega_1 t) + cos(2\omega_2 t) + \\ & + cos[(\omega_1 - \omega_2)t] + cos[(\omega_1 + \omega_2)t] \big\} \end{aligned} \tag{4.42}$$

The first term is the DC polarization to which we referred at the beginning of this section and this results from the optical rectification of the electric field. The terms oscillating at $2\omega_1$ and $2\omega_2$ come from the second-harmonic generation of the single fields. The last two terms are linked, respectively, to the difference frequency generation (or to OR if the resulting frequency is around zero) and to sum frequency generation.
Optical rectification can originate also from a self-interaction of a femtosecond pulse. Indeed, in that case, the low frequency component is generated by the interactions of the frequencies constituting the spectrum.

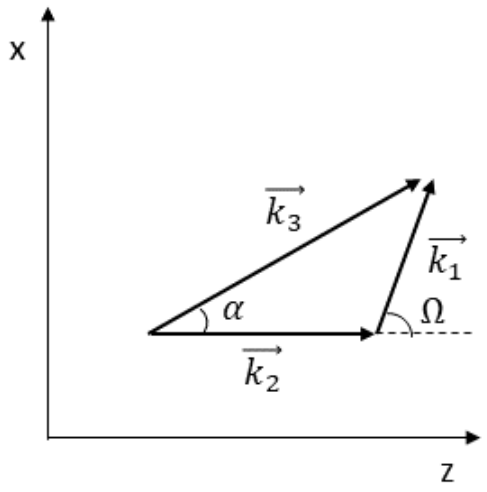

Figure 4.12: Directions of the pulses wavevectors in non-collinear geometry.

4.2 Mid-infrared generation

Broadband mid-infrared pulse generation can be obtained by exploiting collinear intrapulse difference frequency generation (IDFG) in suitable nonlinear crystal. IDFG is a nonlinear process characterized by simplicity, compactness and reduced jitter [78]. Differently from classical DFG described above, it exploits the interactions among the components constituting the spectrum of the pulse. The choice of the crystal in this process is fundamental since it must be both transparent in near-infrared and in mid-infrared regions. For an input pulse centred around 1 µm there few possibilities represented by lithium thiogallate ($LiGaS_2$) and orientation-patterned gallium phosphide (OP-GAP) [14]. Apart from the transparency, there are other characteristics to satisfy. Indeed, damage threshold of the crystal must be sufficiently high since pulses with durations lower than 15 fs which are requires by IDFG increase the possibility of two photon absorption. On the other hand, having such short pulses, increase a little bit the interaction length in the crystal. In case of pulses centred around 1 µm with duration of 15 fs, this length is estimated to be four times lower of the corresponding pulses centred around 1.5 µm [14]. So, by further reducing the duration, we can mitigate a little bit this downsized. This justify why it is important broaden the spectrum as much as possible and completely compensate the dispersion. Other parameters that play an important role in the choice of the crystal are the effective nonlinear coefficient d_{eff} and the phase matching properties [79]. As already said, achieving a perfect phase matching condition is beneficial for the efficiency of the process.
Now, we proceed by comparing OP-GaP and $LiGaS_2$ on the base of the parameters just listed and of the results obtained in previous experiments. Orientation-patterned gallium phosphide belongs to the category of quasi-phase matching materials [80]. The name comes from the fact that in this kind of nonlinear optical material a perfect phase matching condition is difficult to achieve since they are isotropic. An alternative is represented by the QPM condition that here is not achieved like in ferro-electric materials by applying strong fields and modulating second-order optical susceptibility $\chi^{(2)}$. Indeed, they exploit a novel technique that produce crystals characterized by a periodic pattern of domain orientation from which comes the name "oriented-patterned". The first kind of QPM material used in production of mid-infrared radiation was OP-GaAs [79] which shows an excellent performance in the neighbourhood of 2 µm in terms of losses and interaction lengths [80]. However, for our purpose we cannot use it due to the high absorption for wavelength lower than 1.73 µm [80]. An equivalent alternative but with a broader spectrum is represented by the OP-GaP whose cut-off frequency is fixed at 800 µm [79]. OP-GaP is characterized by higher band gap with respect to OP-GaAs mitigating the multi-photon absorption that as said could damage the medium. It shows a thermal conductivity of 110 W/mk [80] which is three times larger than OP-GaAs and a quite high nonlinearity (d_{eff}=70.6 pm/V [80]). The damage threshold is higher than 0.8 J/cm^2 [14].
$LiGaS_2$ (LGS) is characterized by wurtzite-type structure [81] (see Figure 4.13) showing a high thermal conductivity and high band gap [82]. It is non centrosymmetric and it belongs to the category of negative biaxial crystals [82]. The birefringence makes the perfect phase matching condition easily achievable differently from what said for oriented-patterned materials.

In our experiment we were not able to reach the mid-infrared generation for two reasons. The first one related to the fact that, as already said in Chapter 3, we had no a FROG setup to characterize pulses after supercontinuum generation. The second one is linked to these two crystals which are quite expensive and very difficult to find. In the following text, we limit to make some estimations about the performance of our system and to analysis which crystal is the best for our purpose. We refer to two experiments where these materials were employed: one performed by Nakamura in Ref. [14] while the other by Pupeza in Ref. [78]. In the latter, they used a LGS crystal solving the power scalability problems that affect this kind of experiments especially when radiation is centred around 1.5 µm [83]. Indeed, they were able to obtain radiation with an average power of 103 mW spanning a spectrum from 6.4 µm to 16.4 µm (610-1563 cm^{-1}). However, these data come from input pulses with an average power of 50 W and with a duration of 19 fs which are quite different from the ones at our disposal. Despite the good results, we are not able to make a fair estimation since the quantities that come into play in this process are a lot.

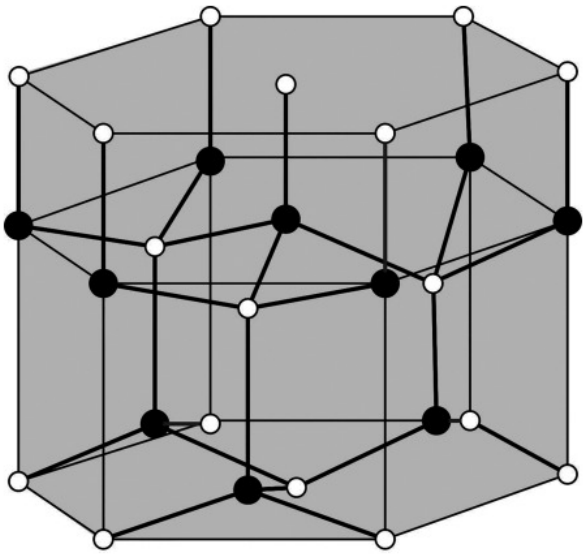

Figure 4.13: Wurtzite-type structure of lithium thiogallate ($LiGaS_2$) [81].

The experiment reported by Nakamura, used instead the OP-GaP. Here, the pulses at the input of the crystal have similar characteristics to ours. Indeed, their duration is 12.1 fs and the average power is 3.3 W. With such pulses, they were able to get a radiation spanning a spectrum between 8.1 µm and 13.1 µm (760-1240 cm^{-1}) and an average power of 1.2 mW. However, this is not the unique result reported since they tested two different grating periods. The result just mentioned was obtained with a period of 27 µm while with 31 µm the radiation generated spans a spectrum from 9.8 µm to 17 µm (590-1020 cm^{-1}). Despite a tighter spectrum and a lower average power, we would have decided to use this crystal since the similar characteristics of the pulses ensure us about the result. In our case, with 0.8-mm long OP-GaP crystal we estimate to have a smaller span since the spectral broadening is half the one obtained by Nakamura. Rough values could be 9.5-12 µm (830-1050 cm^{-1}) for a gratings period

of 27 µm and 11.6-15 µm (666-860 cm^{-1}) for 31 µm. These values must be carefully managed since the quantities into play, as already said, are a lot and everything, also the pulse duration, comes from rough estimations. For what about the average power, we estimate to have the same values reported by Nakamura. In terms of setup, after the crystal a dichroic mirror that is not depicted in Fig. 2.1 is needed to separate the mid-infrared radiation from the pump pulses. A further long-pass filter can be added in order to eliminate the near-infrared radiation leaking the dichroic mirror. One key aspect to analyse is the chromatic dispersion introduced by the crystal that at 1300 nm is quite high (>1300 fs^2/mm [14]). This can be compensated by increasing the distance of the prisms or the length of the hollow core fiber in the compression stage that precedes the crystal. In this way we provide a negative chirp that is the compensated by the positive dispersion of the OP-GaP.
Regardless of the choice of the crystal, the broadband mid-infrared radiation generated can be exploited for spectroscopic application in molecular fingerprint (500-1800 cm^{-1}) [14] allowing the identification of critical information about the structure and the properties of many molecules. Apart form that, it can be also used in very precises measurements exploiting the dual-comb spectroscopy.

4.3 Other applications

In this section we list other applications of few-optical-cycle pulses that go beyond the mid-infrared generation which is the main goal of this thesis work. We make a brief description of two processes based on the second-order nonlinear processes just treated: generation of THz-radiation pulses and 4^{th}-harmonic generation.

4.3.1 Generation of THz-radiation pulses

Terahertz spectrum is collocated among the electronics region characterized by radio, micro- and, millimetre waves and the photonic one constituted by IR, visible, UV and, X-ray. THz radiation finds a lot of spectroscopic and imaging applications [77]. Recent advancements in research employ it in the detection of single-base pair differences in femtomolar concentrations of DNA [84], in the observation of the temporal evolution of exciton formation in semiconductors [85] and, in understanding of carrier dynamics in high-temperature superconductors [86].
THz radiation can be generated by exploiting the optical rectification of ultrashort pulses. The materials used are different and classified into three categories: semiconductors, inorganic and organic electrooptic crystals [77]. Among semiconductors we find gallium arsenide (GaAs), gallium phosphide (GaP), cadmium telluride (CdTe) and, zinc telluride (ZnTe) [77]. In the category of inorganic crystal we have lithium niobate ($LiNbO_3$) and lithium tantalate ($LiTaO_3$) which are relative robust and readily available in large sizes [77]. Among all the categories, organic electrooptic crystals like DAST (4-dimethylamino-N-methylstilbazolium tosylate) are the ones that provide the strongest THz signal [77]. In all these media, if we want to achieve a high efficiency, factors like thickness, crystal orientation, absorption, and dispersion must be properly chosen. However, also in this case, the principal parameter that has the strongest

impact is the phase matching. In some materials like GaP and GaAs, a perfect phase matching condition can be achieved with a collinear scheme. Furthermore, they are characterized by a quite large phase matching bandwidth. In media like $LiNbO_3$ a Cherenkov phase matching scheme [87] is required while in other crystals a quasi-phase matching condition is achieved by a periodic pooling [88]. Generally, the strongest THz radiation is got with pulses characterized by a very low temporal duration. Indeed, the radiated electric field is proportional to the second-order derivative of nonlinear polarization and in case of short pulse, the latter is very strong. Further, by using such pulses we can obtain very wide bandwidth of terahertz pulses.

4.3.2 Fourth-harmonic generation

Fourth-harmonic generation is a nonlinear frequency conversion process that produces a radiation with a wavelength four times lower than the pump wavelength. It can be generated by means of two consequent second-harmonic generations in two different nonlinear crystals.
To generate visible second-harmonic, it is possible to use mainly five crystals: lithium tetraborate LiB_3O_5 (LBO), bismuth borate BiB_3O_5 (BiBO), periodically poled titanium phosphate (PPKTP) [89], potassium boro oxalate (KBO) [90], and beta barium borate (BBO) [91]. Generally, the last two materials are not so used due to the lower performance [89] compared to the other three crystals. Indeed, BBO is mainly adopted in the second stage when we pass from visible to UV. Among the remaining materials the most suitable and the most used is the LBO. Even if it is characterized by a low nonlinear coefficient compared to the other two crystals, LBO has the advantage of a lower walk-off effect and higher damage threshold.
For the second stage, the most used crystals are the already mentioned BBO and cesium lithium borate (CLBO). It is difficult to determine which is the best for this frequency conversion. Indeed, BBO seems to be the most indicated due to a high nonlinear coefficient. On the other hand, the low acceptance angle and the large walk-off [89] require a specific orientation of the crystal. Also CLBO shows good performances in the process but this is true only if it works at a temperature of -15°C and as consequence the complexity of the system increases.
One drawback characterizing all the processes that deal with strong UV light is the low lifetime of the crystals used due to the degradation caused by the radiation itself. Nonetheless, light in this spectral region can be used in laser material processing, for pumping dye lasers, and in spectroscopic applications for the detection of dangerous materials [89].

5 | Conclusions and future developments

In this thesis work we demonstrated a simple approach to generate amplified few-optical-cycles pulses for broadband mid-infrared generation by combining an Yb-doped fiber amplifier and the supercontinuum generation in a photonic crystal fiber. The initial pulses are emitted by a mode-locked Yb:CALGO femtosecond laser and they are characterized by a duration of 70 fs and an average power of 45 mW. After compensating the dispersion accumulated in fiber amplifier, we obtained pulses with a duration of 80 fs and an average power of 5 W. These are then focused into a photonic crystal fiber producing approximately a spectral broadening of 100 nm. If the output pulses are optically compressed and focused into an OP-GaP crystal, they can generate by means of intrapulse difference frequency generation a radiation spanning the mid-infrared range. Mid-infrared sources combine broad bandwidth with high spectral resolution and brightness [92] making them suitable to spectroscopic applications in molecular fingerprint region (500-1800 cm^{-1}). The absorption spectroscopy in this spectral range can be used to retrieve critical information on material structure for physical, chemical, and biological sciences [93]. The advantage of using a 1 µm mode-locked laser as master oscillator is the possibility to achieve alternative applications by simply change the type of crystal. The most relevant ones are terahertz radiation generation and the 4^{th}-harmonic generation.

Our results can be considered satisfactory since if compared with the ones reported, for example, by Nakamura in Ref. [14], they are quite similar. On the other hand, we know the potential of our system and we are confident that future versions could achieve a better result especially in terms of average power of the radiation generated. A high efficiency could be obtained by using in the amplifier a pump diode with a higher precision with respect to one we used. This would mean reaching the same level of power with a lower pump current. As consequence, the instabilities presented with high currents could be reduced a little bit making the setup more stable. Also the spectral broadening could be even larger if the light coupled in photonic crystal fiber would be increased. This could be done by adopting a lens with even lower focal length or by increasing the power at the input of the fiber.

Bibliography

[1] W. Cao and Y. Duan. Current status of methods and techniques for breath analysis. *Critical Reviews in Analytical Chemistry*, 37(1):3–13, 2007. doi: 10.1080/10408340600976499.

[2] C.E. McGrew H.H. Funke, B.L. Grissom and M.W. Raynor. Techniques for the measurement of trace moisture in highpurity electronic specialty gases. *Review of Scientific Instruments*, 74(9):3909–3933, 2003. doi: 10.1063/1.1597939.

[3] M.W. Todd et al. Application of mid-infrared cavity-ringdown spectroscopy to trace explosives vapor detection using a broadly tunable (6-8 µm) optical parametric oscillator. *Applied Physics B*, 75(2):367–376, 2002. doi: 10.1007/s00340-002-0991-8.

[4] D. Richter et al. Development of a tunable mid-ir difference frequency laser source for highly sensitive airborne trace gas detection. *Applied Physics B*, 75(2-3):281–288, 2002. doi: 10.1007/s00340-002-0948-y.

[5] I. Galli et al. Spectroscopic detection of radiocarbon dioxide at parts-per-quadrillion sensitivity. *Optica*, 3(4):385–388, 2016. doi: 10.1364/OPTICA.3.000385.

[6] S. Dupont et al. Ir microscopy utilizing intense supercontinuum light source. *Optics Express*, 20(5):4887–4892, 2012. doi: 10.1364/OE.20.004887.

[7] T. Paasch-Colberg A. Schiffrin and N. Karpowicz. Optical-field-induced current in dielectrics. *Nature*, 493:70–74, 2013. doi: 10.1038/nature11567.

[8] F. Krausz and M.I. Stockman. Attosecond metrology: from electron capture to future signal processing. *Nature Photon*, 8:205–213, 2014. doi: 10.1038/nphoton.2014.28.

[9] A.J. Hoffman Y. Yao and C.F. Gmachl. Mid-infrared quantum cascade lasers. *Nature Photonics*, 6:432–439, 2012. doi: 10.1038/nphoton.2012.143.

[10] Q. Ru et al. Two-octave-wide (3–12 µm) subharmonic produced in a minimally dispersive optical parametric oscillator cavity. *Optics Letters*, 46(4):709–712, 2021. doi: 10.1364/OL.403910.

[11] D.D. Hudson et al. Toward all-fiber supercontinuum spanning the mid-infrared. *Optica*, 4(10):1163–1166, 2017. doi: 10.1364/OPTICA.4.001163.

[12] D. Sanchez et al. 7 m, ultrafast, sub-millijoule-level mid-infrared optical paramet-

ric chirped pulse amplifier pumped at 2 m. *Optics Letters*, 3(2):147–150, 2016. doi: 10.1364/OPTICA.3.000147.

[13] T.A. Johnson T.W. Neely and S.A. Diddams. High-power broadband laser source tunable from 3.0 m to 4.4 m based on a femtosecond yb:fiber oscillator. *Optics Letters*, 36(20):4020–4022, 2011. doi: 10.1364/OL.36.004020.

[14] T. Nakamura et al. Simple approach to broadband mid-infrared pulse generation with a mode-locked yb-doped fiber laser. *Optics Letters*, 47(7):1790–1793, 2022. doi: 10.1364/OL.450921.

[15] N. Newbury I. Coddington and W. Swann. Dual-comb spectroscopy. *Optica*, 3(4): 414–426, 2016. doi: 10.1364/OPTICA.3.000414.

[16] A. Kawai et al. Mid-infrared time-stretch optical coherence tomography. *Communications Physics*, 3(1):152, 2020. doi: 10.1038/s42005-020-00420-3.

[17] I. Pupeza et al. Field-resolved infrared spectroscopy of biological systems. *Nature*, 577:52–59, 2020. doi: 10.1038/s41586-019-1850-7.

[18] F. Pirzio et al. Ultrafast, solid-state oscillators based on broadband, multisite yb-doped crystals. *Optics Express*, 24(11):11782–11792, 2016. doi: 10.1364/OE.24.011782.

[19] AM Weiner. *Ultrafast optics*. John Wiley Sons, 2008. doi: 10.1002/9780470473467.

[20] O. Svelto. *Principle of lasers*. Springer, 5th ed. edition, 2009. doi: 10.1007/978-1-4419-1302-9.

[21] R.K. Jain and J.P. Heritage. Generation of synchronized cw trains of picosecond pulses at two independently tunable wavelengths. *Applied Physics Letters*, 32(1): 41–44, 1978. doi: 10.1063/1.89833.

[22] D. Kuizenga and A. Siegman. Fm and am mode locking of the homogeneous laser - part ii: Experimental results in a nd:yag laser with internal fm modulation. *IEEE Journal of Quantum Electronics*, 6(11):709–715, 1970. doi: 10.1109/JQE.1970.1076344.

[23] T.F. Carruthers and I.N. Duling. 10-ghz, 1.3-ps erbium fiber laser employing soliton pulse shortening. *Optics Letters*, 21(23):1927–1929, 1996. doi: 10.1364/OL.21.001927.

[24] E.P. Ippen. Principles of passive mode locking. *Applied Physics B*, 58(3):159–170, 1994. doi: 10.1007/BF01081309.

[25] P.N. Kean D.E. Spence and W. Sibbett. 60-fsec pulse generation from a self-mode-locked ti:sapphire laser. *Optics Letters*, 16(1):42–44, 1991. doi: 10.1364/OL.16.000042.

[26] L. Spinelli. Cpdp7. *Digest Conf. Lasers. Electro-Opt.*, 1991.

[27] F. Doutre et al. Large temporal narrowing of subnanosecond pulses in a low-birefringence optical fiber. *Optics Letters*, 33(16):1789–1791, 2008. doi: 10.1364/OL.33.001789.

[28] Y. Meng Q. Liu H. Wang, J. Pan and Y. Shen. Advances of yb:calgo laser crystals. *Crystals*, 11(9), 2021. doi: 10.3390/cryst11091131.

[29] A.C. Tropper R. Paschotta, J. Nilsson and D.C. Hanna. Ytterbium-doped fiber amplifiers. *IEEE Journal of Quantum Electronics*, 33(7):1049–1056, 1997. doi: 10.1109/3.594865.

[30] R. Paschotta et al. Lifetime quenching in yb-doped fibres. *Optics Communications*, 136(5):375–378, 1997. doi: 10.1016/S0030-4018(96)00720-1.

[31] Y. Zaouter et al. 47-fs diode-pumped Yb^{3+} : $CaGdAlO_4$ laser. *Optics Letters*, 31 (1):119–121, 2006. doi: 10.1364/OL.31.000119.

[32] M. E. Fermann and I. Hartl. Ultrafast fiber laser technology. *IEEE Journal of Selected Topics in Quantum Electronics*, 15(1):191–206, 2009. doi: 10.1109/JSTQE.2008.2010246.

[33] A. Hardy and R. Oron. Signal amplification in strongly pumped fiber amplifiers. *IEEE Journal of Quantum Electronics*, 33(3):307–313, 1997. doi: 10.1109/3.555997.

[34] D.C. Hanna V. Cautaerts, R. Paschotta and D.J. Richardson. Stretched pulse Yb^{3+}:silica fiber laser. *Optics letters*, 22(5):316–318, 1997. doi: 10.1364/ol.22.000316.

[35] Y. Kobayashi X. Zhou, D. Yoshitomi and K. Torizuka. Generation of 28-fs pulses from a mode-locked ytterbium fiber oscillator. *Optics Express*, 16(10):7055–7059, 2008. doi: 10.1364/OE.16.007055.

[36] Gang-Ding Peng, editor. *Handbook of optical fibers*. Springer, 2019. doi: 10.1007/978-981-10-7087-7.

[37] W. J. Miniscalco. Erbium-doped glasses for fiber amplifiers at 1500 nm. *Journal of Lightwave Technology*, 9(2):234–250, 1991. doi: 10.1109/50.65882.

[38] R. Wyatt. Spectroscopy of rare earth doped fibres. *SPIE*, 1171:54–64, 1990. doi: 10.1117/12.963138.

[39] M. Federighi and F. Di Pasquale. The effect of pair-induced energy transfer on the performance of silica waveguide amplifiers with high Er^{3+}/Yb^{3+} concentrations. *IEEE Photonics Technology Letters*, 7(3):303–305, 1995. doi: 10.1109/68.372753.

[40] V. Dominic. 110 w fibre laser. pages CPD11/1–CPD11/2, 1999. doi: 10.1109/CLEO.1999.834612.

[41] S.C. Rashleigh R. Ulrich and W. Eickhoff. Bending-induced birefringence in single-mode fibers. *Optics Letters*, 5(6):273–275, 1980. doi: 10.1364/OL.5.000273.

[42] K. Okamoto J. Noda and Y. Sasaki. Polarization-maintaining fibers and their applications. *Journal of Lightwave Technology*, 4(8):1071–1089, 1986. doi: 10.1109/JLT.1986.1074847.

[43] R. Paschotta. *Field guide to optical fiber technology*. SPIE, 2010. doi: 10.1117/3.853722.

[44] M.-Y. Chen and Y.-K. Zhang. Improved design of polarization-maintaining photonic crystal fibers. *Optics Letters*, 33(21):2542–2544, 2008. doi: 10.1364/OL.33.002542.

[45] S. Ramachandran et al. Ultra-large effective-area, higher-order mode fibers: a new strategy for high-power lasers. *Laser Photonics Reviews*, 2(6):429–448. doi: https://doi.org/10.1002/lpor.200810016.

[46] S. Ramachandran et al. Light propagation with ultralarge modal areas in optical fibers. *Optics Letters*, 31(12):1797–1799, 2006. doi: 10.1364/OL.31.001797.

[47] F. Jansen et al. Thermally induced waveguide changes in active fibers. *Optics Express*, 20(4):3997–4008, 2012. doi: 10.1364/OE.20.003997.

[48] P. Russell. Photonic crystal fibers. *Science*, 299(5605):358–362, 2003. doi: 10.1126/science.1079280.

[49] J.C. Knight et al. Anomalous dispersion in photonic crystal fiber. *IEEE Photonics Technology Letters*, 12(7):807–809, 2000. doi: 10.1109/68.853507.

[50] G. P. Agrawal. *Nonlinear Fiber Optics*. Academic Press, 6$^{\text{th}}$ ed. edition, 2019. doi: 10.1016/C2018-0-01168-8.

[51] G.J. Foschini and C.D. Poole. Statistical theory of polarization dispersion in single mode fibers. *Journal of Lightwave Technology*, 9(11):1439–1456, 1991. doi: 10.1109/50.97630.

[52] L.M. Molteni et al. Low-noise yb:calgo optical frequency comb. *Optics Express*, 29(13):19495–19505, 2021. doi: 10.1364/OE.428603.

[53] R. Paschotta. *Field Guide to Laser Pulse Generation*. SPIE Press Book, 2008. doi: 10.1117/3.800629.

[54] J. Minowa H. Ishio and K. Nosu. Review and status of wavelength-division-multiplexing technology and its application. *Journal of Lightwave Technology*, 2(4):448–463, 1984. doi: 10.1109/JLT.1984.1073653.

[55] E. Delevaque et al. Modeling of pair-induced quenching in erbium-doped silicate fibers. *IEEE Photonics Technology Letters*, 5(1):73–75, 1993. doi: 10.1109/68.185065.

[56] E.B. Treacy. Optical pulse compression with diffraction gratings. *IEEE Journal of Quantum Electronics*, 5(9):454–458, 1969. doi: 10.1109/JQE.1969.1076303.

[57] C.V. Shank et al. Compression of femtosecond optical pulses. *Applied Physics Letters*, 40(9):761–763, 1982. doi: 10.1063/1.93276.

[58] O.E. Martinez R.L. Fork and J.P. Gordon. Negative dispersion using pairs of prisms. *Optics Letters*, 9(5):150–152, 1984. doi: 10.1364/OL.9.000150.

[59] F.M. Mitschke and L.F. Mollenauer. Discovery of the soliton self-frequency shift. *Optics Letters*, 11(10):659–661, 1986. doi: 10.1364/OL.11.000659.

[60] W.J. Tomlinson R.H. Stolen, J.P. Gordon and H.A. Haus. Raman response function of silica-core fibers. *Journal of the Optical Society of America B*, 6(6):1159–1166, 1989. doi: 10.1364/JOSAB.6.001159.

[61] W.J. Tomlinson R.H. Stolen. Effect of the raman part of the nonlinear refractive index on propagation of ultrashort optical pulses in fibers. *Journal of the Optical Society of America B*, 9(4):565–573, 1992. doi: 10.1364/JOSAB.9.000565.

[62] P.V. Mamyshev and S.V. Chernikov. Ultrashort-pulse propagation in optical fibers. *Optics Letters*, 15(19):1076–1078, 1990. doi: 10.1364/OL.15.001076.

[63] T.K. Gustafson F. DeMartini, C.H. Townes and P.L. Kelley. Self-steepening of light pulses. *Physical Review Letters*, 164(2):312–323, 1967. doi: 10.1103/PhysRev.164.312.

[64] T. Brabec and F. Krausz. Nonlinear optical pulse propagation in the single-cycle regime. *Physical Review Letters*, 78(17):3282–3285, 1997. doi: 10.1103/PhysRevLett.78.3282.

[65] S. Chi and S. Wang. Derivation of a wave equation for pulse propagation beyond a slowly varying envelope approximation. *Optical and quantum electronics*, 28:1351–1357, 1996. doi: 10.1007/BF00326208.

[66] J. Dudley and J. Taylor. *Supercontinuum Generation in Optical Fibers*. Cambridge University Press, 2010. doi: 10.1017/CBO9780511750465.

[67] F. Dias J.M. Dudley and M. Erkintalo. Instabilities, breathers and rogue waves in optics. *Nature Photonics*, 8(10):755–764, 2014. doi: 10.1038/nphoton.2014.220.

[68] M.N. Islam et al. Broad bandwidths from frequency-shifting solitons in fibers. *Optics Letters*, 14(7):370–372, 1989. doi: 10.1364/OL.14.000370.

[69] K.L. Corwin et al. Fundamental noise limitations to supercontinuum generation in microstructure fiber. *Physical Review Letters*, 90(11):113904, 2003. doi: 10.1103/PhysRevLett.90.113904.

[70] R. Trebino. *Frequency-Resolved Optical Gating: the Measurement of Ultrashort Laser Pulses*. Springer New York, 2002. doi: 10.1007/978-1-4615-1181-6.

[71] D.J. Kane. Principal components generalized projections: a review. *Journal of the Optical Society of America B*, 25(6):A120–A132, 2008. doi: 10.1364/JOSAB.25.00A120.

[72] J. Hunter K.W. DeLong, R. Trebino and W.E. White. Frequency-resolved optical gating using second-harmonic generation. *Journal of the Optical Society of America B*, 11(11):2206–2215, 1994. doi: 10.1364/JOSAB.11.002206.

[73] R. Trebino et al. Measuring ultrashort laser pulses in the time-frequency domain using frequency-resolved optical gating. *Review of Scientific Instruments*, 68(9): 3277–3295, 1997. doi: 10.1063/1.1148286.

[74] D.J. Kane and R. Trebino. Characterization of arbitrary femtosecond pulses using frequency-resolved optical gating. *IEEE Journal of Quantum Electronics*, 29(2): 571–579, 1993. doi: 10.1109/3.199311.

[75] D.S. Hum and M.M. Fejer. Quasi-phasematching. *Comptes Rendus Physique*, 8 (2):180–198, 2007. doi: https://doi.org/10.1016/j.crhy.2006.10.022.

[76] L.E. Myers et al. Quasi-phase-matched optical parametric oscillators in bulk periodically poled $LiNbO_3$. *Journal of the Optical Society of America B*, 12(11): 2102–2116, 1995. doi: 10.1364/JOSAB.12.002102.

[77] *Terahertz Spectroscopy:Principles and Applications*. CRC Press, 2008. doi: 10.1201/9781420007701.

[78] D. Sánchez I. Pupeza and J. Zhang. High-power sub-two-cycle mid-infrared pulses at 100 mhz repetition rate. *Nature Photonics*, 9(11):721–724, 2015. doi: 10.1038/nphoton.2015.179.

[79] J. Wei et al. Performance characterization of mid-infrared difference-frequency-generation in orientation-patterned gallium phosphide. *Optics Materials Express*, 8(3):555–567, 2018. doi: 10.1364/OME.8.000555.

[80] P.G. Schunemann et al. Advances in nonlinear optical crystals for mid-infrared coherent sources. *Journal of the Optical Society of America B*, 33(11):D36–D43, 2016. doi: 10.1364/JOSAB.33.000D36.

[81] J. S. Galsin. *Solid State Physics: An Introduction to Theory*. Academic Press, 2019. doi: 10.1016/C2018-0-01175-5.

[82] L. Isaenko et al. Growth and properties of $LiGaX_2$ (x = s, se, te) single crystals for nonlinear optical applications in the mid-ir. *Crystal Research and Technology*, 38(3-5):379–387, 2003. doi: 10.1002/crat.200310047.

[83] A. Gambetta et al. Milliwatt-level frequency combs in the 8–14 m range via difference frequency generation from an er:fiber oscillator. *Optics Letters*, 38(7): 1155–1157, 2013. doi: 10.1364/OL.38.001155.

[84] M. Brucherseifer et al. Label free probing of binding state of dna by time-domain terahertz sensing. 77(24):4049–4051, 2000. doi: 10.1063/1.1332415.

[85] R. A. Kaindl et al. Ultrafast terahertz probes of transient conducting and insulating phases in an electron-hole gas. *Nature*, 423(6941):734–738, 2003. doi: 10.1038/nature01676.

[86] J. Corson. Vanishing of phase coherence in underdoped $Bi_2Sr_2CaCu_2O_{8+d}$. *Nature*, 398(6724):221–223, 1999. doi: 10.1038/18402.

[87] J.A. Valdmanis D.H. Auston, K.P. Cheung and D.A. Kleinman. Cherenkov radiation from femtosecond optical pulses in electro-optic media. *Physical Review Letters*, 53(16):1555–1558, 1984. doi: 10.1103/PhysRevLett.53.1555.

[88] K.L. Vodopyanov. Optical thz-wave generation with periodically-inverted gaas. *Laser Photonics Reviews*, 2(1-2):11–25, 2008. doi: 10.1002/lpor.200710028.

[89] J.J. Zondy R. Le Targat and P. Lemonde. 75 *Optics Communications*, 247(4): 471–481, 2005. doi: 10.1016/j.optcom.2004.11.081.

[90] E. Peik G. Hollemann and H. Walther. Frequency-stabilized diode-pumped nd:yag laser at 946 nm with harmonics at 473 and 237 nm. *Optics Letters*, 19(3):192–194, 1994. doi: 10.1364/OL.19.000192.

[91] X. Ding et al. Generation of 3.5w high efficiency blue-violet laser by intracavity frequency-doubling of an all-solid-state tunable ti:sapphire laser. *Optics Express*, 16(7):4582–4587, 2008. doi: 10.1364/OE.16.004582.

[92] I.T. Sorokina K.L. Vodopyanov, E. Sorokin and P.G. Schunemann. Mid-ir frequency comb source spanning 4.4–5.4 m based on subharmonic gaas optical parametric oscillator. *Optics Letters*, 36(12):2275–2277, 2011. doi: 10.1364/OL.36.002275.

[93] H. Timmers et al. Molecular fingerprinting with bright, broadband infrared frequency combs. *Optica*, 5(6):727–732, 2018. doi: 10.1364/OPTICA.5.000727.